Forecasting stratocumulus under a strong thermal inversion and in regions of subsidence, with a large-eddy simulation model

Marijke Schuurbiers

student number: 1508830

Master's thesis

Supervisor:
Dr. S.R. de Roode

Reviewers:
Prof. Dr. H.J.J. Jonker
Dr. Ir. M.J. Tummers
Dr. Ir. R.A. Verzijlbergh
Dr. M.C. van Zanten

Atmospheric Physics
Department of Geoscience and Remote Sensing
Faculty of Civil Engineering
Delft University of Technology

September 22, 2014

Abstract

In this study simulation of stratocumulus under a strong thermal inversions and in regions of subsidence with a Large-Eddy Simulation (LES) model has been researched.

With use of observational data covering the year 2011 and 2012, stratocumulus cases are identified at Cabauw, in the Netherlands. With use of the selection, the climatology of stratocumulus at Cabauw is studied. It was found that the occurrence of stratocumulus under a strong thermal inversions and in regions of subsidence is about 5 %. Stratocumulus is most likely to occur in combination with a south-west or north-east wind direction, in wintertime and in the morning or evening hours.

A study of the representation of stratocumulus in a mesoscale model (RACMO) has shown that the model has difficulties with predicting stratocumulus. Subsequently simulations with a LES model have been performed on the basis of data assimilation. It is found that with use of observational data and LES the prediction of stratocumulus has potential. Especially predictions of the down welling solar radiation in the first 3 to 6 hours after initialization have shown to be improved.

Contents

Chapter 1

Introduction

Stratocumulus is a cloud type that forms at low altitudes. These clouds typically consist of large thin sheets with a high area coverage.

Conventional large scale weather forecast models have troubles representing stratocumulus. (Wood, 2012) Due to the relative shallowness of these clouds they are often under predicted. For example from January 30 till February 1 2011 an extended stratocumulus cloud deck covered the Netherlands, as can be seen on the satellite image in figure 1.1. Several forecasts however predicted the cloud deck would break up (Jacobs et al., 2012):
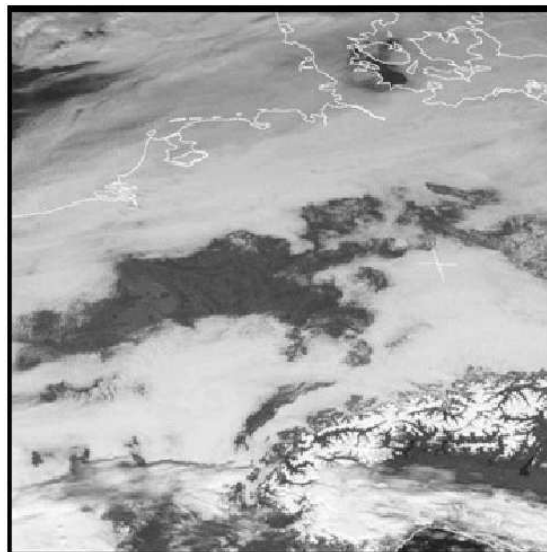
Figure 1.1: Satellite image of a stratocumulus cloud deck covering the Netherlands on 31 January 2011, 12.00 UTC (Jacobs et al., 2012).

" ... the amount of stratocumulus and persistence of the observed stratocumulus cloud deck is underpredicted in various European weather forecast models, such as the ECMWF, COSMO, and HiRLAM model. Also in HAR-

MONIE the stratocumulus cloud deck disappears for a couple of hours around noontime.

On the contrary numerical experiments with a large-eddy simulation (LES) model did result in a solid and persistent cloud deck for this case, as reported by Jacobs et al. (2012).

A LES model has a much higher resolution (typically 10 - 100 m) than operational weather forecast models (in the order of 10^4 km). Due to the higher vertical resolution it is better capable to capture the sharp inversion layer under which these clouds typically form. However the fine horizontal resolution is presently too computational expensive to cover large domains. Nevertheless improving weather forecast locally can be very beneficial to for example airports or solar power plants. Furthermore with the use of reliable simulations more insight can be gained in the processes controlling stratocumulus and this can improve parameterization in global models.

The aim of this research is to see whether the formation of stratocumulus under a strong thermal inversion and in regions of subsidence can be well predicted with use of LES when initialized with observations. Therefore stratocumulus cases are identified in the years 2011 and 2012 with use of available weather observation data from the Cabauw measurement site. Some of these selected cases will be simulated with the high resolution model and then evaluated. Furthermore forecasts made by the regional atmospheric climate model RACMO (generated by the KNMI) will be compared with the observations to obtain more insight in stratocumulus prediction.

1.1 Importance to solar power

Despite the fact that stratocumulus clouds are shallow they reflect more than half of the down welling solar radiation back to space. Therefore stratocumuli have a big influence on the solar insolation at the Earth's surface, which makes them important to for example the production of solar energy.

Clouds can cause rapid changes in solar insolation and therefore are largely responsible for the variability and uncertainty in the output of photo voltaic cells. (Hoff et al., 2009):

> "Changes in solar insolation at a point due to a passing cloud can exceed 60% of the peak insolation in a matter of seconds. ... For PV systems with a rated capacity of 100 MW, the time it takes to shade the entire system will be on the order of minutes rather than seconds."

To maintain stability of the electric grid, the electrical power generation must match the load. This matching can be achieved more easily by reducing the variability in the highly fluctuating power supplies such as solar power. To provide a more constant power to the grid, solar power plants make use of buffers. Forecasts on clouds are important to be able to address these buffers in time and thereby manage the variability.

Further the balancing of electric supply and load is nowadays achieved by cycling of fossil-fuelled generators. (Lew and Brinkman, 2013) This cycling however reduces the efficiency of these generators and influences their emissions. Improving the clouds forecast is thus beneficial to the electric grid stability and thereby also to the environment.

1.2   Importance to aviation

A reliable forecast of stratocumulus clouds is not only beneficial for solar power generation, but for example also for the aviation business.

The air and platform operations on airports such as Schiphol are very sensitive to low clouds (Jacobs et al., 2011). A precise local weather prediction is therefore very important for the (sustainable) operation of an airport. As quoted in the annual report of the KNMI by the control tower supervisor at Schiphol (KNMI, 2011):

> "Weather information is central to all operations at the airport. The alignment of the runways here and variability of the local weather can throw up some complex challenges. So personal input from a KNMI meteorologist is very useful in the context of processes such as calculating runway capacity. We need really detailed information."

The fact that stratocumulus forms at low heights makes that it can reduce the visibility close to the ground. Furthermore if the temperature of these clouds drops below $0°C$, freezing rain can occur. Stratocumulus can therefore lead to a loss in the available runway capacity. If this loss is not foreseen in time it can lead to flight delays and cancellations. These delays lead to a significant increase in operational costs including extra fuel burn and emissions (de Rover et al., 2008).

For example the airport of San Francisco is located in an area where a lot of stratocumulus occurs. In the period May till October stratus forms and dissipates on a daily cycle in this region. The low clouds impact the operations at the San Francisco airport on approximately 50 till 60 days in this period (Reynolds et al., 2012).

1.3   Outline

Chapter 2 of this report will start with introducing atmospheric variables that are relevant for this research. Furthermore the governing equations for describing the atmospheric boundary layer are discussed. In the following chapter the observational and computational data sources that are used will discussed. Furthermore it contains a description of the setup used for the LES simulations. Chapter 4 explains the method used to identify stratocumulus from the data sets. Thereafter this method is used to look into some of the climatology of stratocumulus at Cabauw. Additionally the simulation data sets are further compared with the observations, with use of scatter plots and so called quality matrices. Chapter 7 contains the results of the simulations as preformed with the LES model. This report is concluded with conclusions and recommendations in Chapter 8.

Chapter 2

Theory

In this chapter various concepts are explained that are used in this research. By describing the stratocumulus properties and atmospheric conditions, associated variables are introduced. Furthermore the governing equations for modelling the atmospheric boundary layer are discussed. The chapter is concluded with a description of the solar zenith angle.

2.1 Stratocumulus appearance

On January 31th 2011 a persistent stratocumulus formation is covering the Netherlands. The left of figure 2.1 shows a satellite image of this cloud deck at 12.00 UTC.
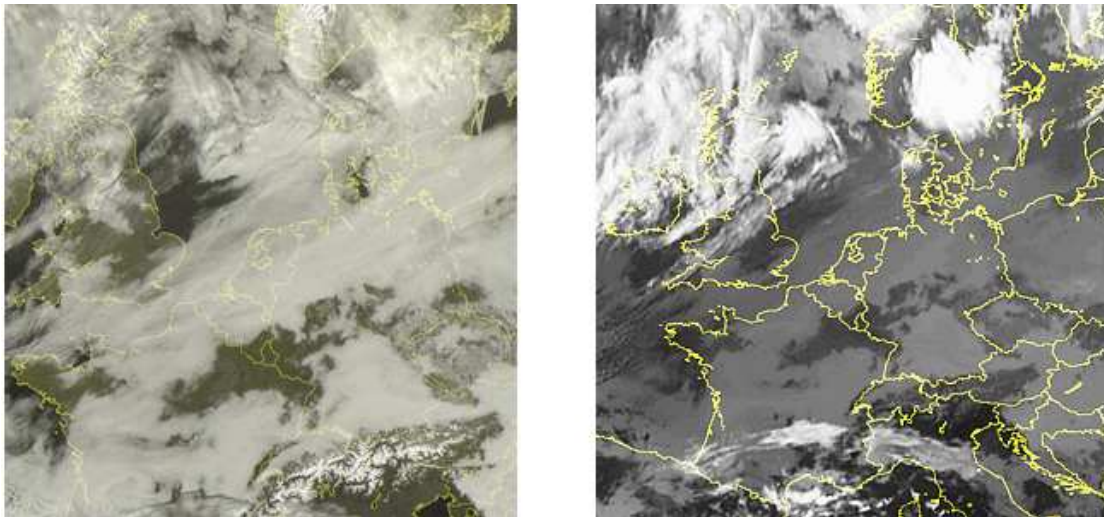
Figure 2.1: Satellite image (left) and infrared satellite image (right) of a stratocumulus formation above the Netherlands on 31/01/2011, 12.00 UTC. Images adapted from Sat24.com.

As typically for stratocumulus, the cloud forms as a large sheet. Note that the structure looks very uniform, for example by comparison with the clouds above Scotland.

This uniformity is not surprising, because the cloud fraction of stratocumulus is typically close to 100% (de Roode, 2004).

The stratocumulus cloud is well visible in satellite images from visible light, because it reflects a lot of the incoming solar radiation. The fraction of radiation reflected by a medium is called albedo. The albedo of stratocumulus clouds can range between about 0.5 and 0.8 Roode et al. (2012).

To be able to give a mathematical expression for the albedo of a cloud, a few important variables need to be introduced. An often used measure in meteorology is the specific humidity q. The specific humidity is the ratio of the mass of water to the total mass of dry air plus water. A distinction can be made for water in its different forms: vapour, liquid and ice. The use of the specific humidity regarding one of these phases is indicated by a subscript. The total specific humidity q_t is defined by:

$$q_t = q_v + q_l + q_i, \tag{2.1}$$

where the indices v, l and i denote the water vapour, liquid water and water in the ice phase respectively. A nonzero water vapour specific humidity is an indicator for the presence of a cloud. The water vapour saturation specific humidity, indicated with a subscript 's', is the water vapour specific humidity corresponding to a saturated water vapour concentration.

With use of the liquid water specific humidity, the liquid water path (LWP) can be determined. The LWP is defined as the vertical integral of the specific liquid water content:

$$\text{LWP} = \int_0^{z_{top}} \rho q_l dz, \tag{2.2}$$

in which ρ is the air density and z the height. For a thin cloud of 300 m with a cloud top height of 500 m and a linear liquid water density increase of 2 g/kg/km, the LWP path is about 0.250 kg/m^2:

$$\text{LWP} = \rho \int_{z_{base}}^{z_{top}} 2 \cdot 10^{-6} z dz = \rho \cdot \frac{1}{2} \cdot 2 \cdot 10^{-6} \cdot (z_{top}^2 - z_{base}^2), \tag{2.3}$$

where the air density is approximate as 1.2 kg/m^3. For stratocumulus the LWP typically has a value around 0.150 kgm^{-2} (de Roode, 2004).

The LWP is related to the optical thickness τ:

$$\tau = \frac{3}{2\rho_l r_e} \text{LWP}, \tag{2.4}$$

in which ρ_l is the density of liquid water and r_e is the cloud droplet effective radius (de Roode, 2004). This radius is about 10 μm in stratocumulus clouds. The optical thickness is a dimensionless quantity that indicates the amount of radiation that is transmitted by a medium. The larger this thickness the more radiation is reflected or absorbed instead of transmitted. The optical thickness of stratocumulus clouds range

from less than 1 to more than 20 (Wood, 2012). The mean value for stratocumulus over land is 11 (Hahn et al., 2001).

Once the optical thickness of a cloud is known, its albedo can be approximated as:

$$\alpha = \frac{\tau}{\tau + 7}, \tag{2.5}$$

where α is the albedo (Wood, 2012). An optical thickness of 11 thus corresponds to a albedo of about 0.6.

The right of figure 2.1 shows the infrared image of the stratocumulus cloud deck at 12.00 UTC. According to Wien's law the wavelength at which a body radiates is inversely proportional to its temperature. Therefore sun radiates at short wavelengths, while the Earth's surface, atmosphere and clouds radiate at long wavelengths. An infrared image shows the longwave radiation that is emitted. The higher the temperature of the surfaces, the darker they appear in the picture. In comparison with the normal satellite photo on the left, the stratocumulus cloud deck is hardly noticeable in the infrared picture. The temperature of the cloud is thus similar to the underlying surface. This is not surprisingly since stratocumulus typically occurs at low altitudes. It belongs to the class of low level clouds, which is characterized by a cloud base height of less than 2 km.

The intensity at which a body radiates is also related to its temperature. This relation is defined by the StefanBoltzmann law:

$$I = \epsilon \sigma T^4, \tag{2.6}$$

in which I is the intensity, ϵ the emissivity, σ the StefanBoltzmann constant and T the temperature. The Earth radiates almost as a black body, meaning that its emissivity is close to 1. The emissivity of a cloudless atmosphere is about 0.8. Therefore the difference between the upwelling longwave radiation emitted by the Earth and the downwelling longwave radiation emitted by a clear atmosphere is in the order of 60 Wm^{-2} (de Roode, 2004). Clouds, however, can have a different emissivity. If a stratocumulus cloud is optically thick enough it can radiate as a black body, just like the Earth (Bennetts et al., 1986). In this case the net longwave radiation will approach zero, as the temperature of the Earth's surface is similar to the cloud temperature.

2.2 Stratocumulus profiles

The left of figure 2.2 shows the vertical profile of the temperature as measured at "de Bilt" in the Netherlands, at the same time as the satellite images of 2.1 were taken. Notice the striking jump in temperature at a height of 600 m. This jump is called a temperature inversion, as the temperature in this layer sharply increases with height instead of decreasing. Typically the top of the cloud layer is marked with such an inversion (Klein and Hartmann, 1993). For stratocumuli the increase in temperature can be as strong as 10-20 K over only tens of meters (Wood, 2012).

The right of figure 2.2 shows the vertical profile of the potential temperature. The potential temperature can be interpreted as the temperature a parcel would have if
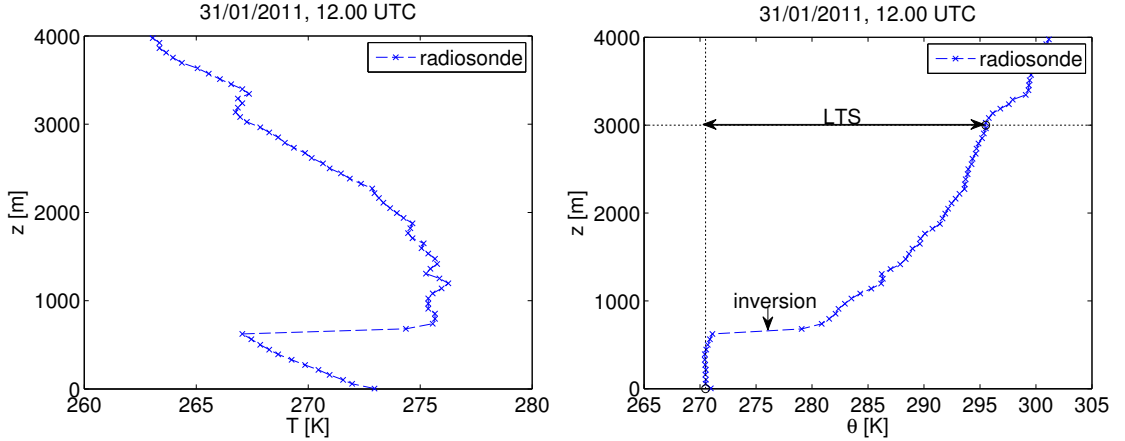
Figure 2.2: The observed temperature (left) and potential temperature (right) on 31/01/2011 at noon as a function of height. Data obtained from a radiosonde released at "de Bilt" in the Netherlands.

it were displaced isentropically to a reference height where the pressure is 1000 hPa. (de Roode, 2004) The definition is as follows:

$$\theta = T(\frac{p_0}{p})^{\frac{R_d}{c_p}}, \tag{2.7}$$

where θ is the potential temperature, p_0 the reference pressure, p the pressure, c_p the isobaric specific heat of 1004.703 JK^{-1}kg^{-1} and R_d the specific gas constant of dry air with value 287.06 JK^{-1}kg^{-1}. The decrease in temperature with height due pressure changes is compensated when using the potential temperature. Thus when a temperature profiles follows the dry adiabatic lapse rate the potential temperature is constant with height. This is visible in the left and right of figure 2.2 up until the inversion height.

With use of the potential temperature, the lower-tropospheric stability (LTS) can be calculated. The LTS is defined as the difference in potential temperature between 700 and 1000 hPa:

$$\text{LTS} = \theta_{700} - \theta_0 \tag{2.8}$$

(Wood and Bretherton, 2006), as illustrated in the left of 2.2. The LTS can be regarded as an indicator for the presence of an inversion layer. A high LTS is likely to be associated with a strong(low-lying) inversion. The height of the inversion is dependent on the entrainment, the process of mixing the dry, warm air from above the cloud into the cloud layer. The entrainment rate w_e is directly related to the inversion height development over time:

$$\frac{\partial z_i}{\partial t} = w_e + \overline{w} - \overline{u_h}\frac{\partial z_i}{\partial x_h}. \tag{2.9}$$

In this equation z_i is the inversion height, $\overline{w}$ the large scale subsidence (vertical velocity), u the velocity and h denotes a summation over the x and y direction. If the air in the

cloud is more turbulent, the entrainment rate will be larger, causing the inversion height to increase.

The potential temperature is conserved for dry air parcels that are isentropically vertically displaced. However, the presence of water in an air parcel alters its properties. Water vapour decreases the average density of air, while liquid water increases the air's density. These density changes also effect the buoyancy of the air parcels. The virtual temperature is a quantity that takes these effects of water into account. It is defined as the temperature that air of a given pressure and density would have if the air were completely dry (de Roode, 2004). With use of the virtual temperature, the gas law thus reads:

$$p = \rho R_d T_v. \tag{2.10}$$

The pressure on the left hand side is a summation of the partial pressures for the dry air, water vapour and liquid water (assuming no ice is present). If one neglects the liquid water partial pressure, this summation is:

$$p = \rho_d R_d T + \rho_v R_v T, \tag{2.11}$$

where R_v is the specific gas constant for water vapour. The virtual potential temperature can now be expressed as:

$$T_v = (\frac{\rho_d}{\rho} + \frac{\rho_v}{\rho}\frac{R_v}{R_d})T. \tag{2.12}$$

Since the total volume is approximately equal to the volume of dry air

$$\frac{\rho_d}{\rho} = \frac{m_d}{m_d + m_v + m_l} = 1 - q_v - q_l \tag{2.13}$$

and

$$\frac{\rho_v}{\rho} = \frac{m_v}{m_d + m_v + m_l} = q_v, \tag{2.14}$$

where m is the mass of the dry air, water vapour and liquid water for the subscripts d, v and l respectively. The virtual temperature T_v can thus be calculated as follows:

$$T_v = (1 - (1 - \frac{1}{\epsilon})q_v - q_l)T, \tag{2.15}$$

with $\epsilon = R_d/R_v$. The virtual potential temperature θ_v is analogously to equation 2.7 defined as:

$$\theta_v = T_v(\frac{p_0}{p})^{\frac{R_d}{c_p}}. \tag{2.16}$$

Additional to density changes due the presence of water in air parcels, heat release or absorption can occur due its phase changes. As the temperature of the environment

decreases with height, the saturation vapour pressure will decrease. When the saturation vapour pressure drops below the water vapour pressure of the parcel, condensation of liquid water will occur. This condensation results in a release of latent heat. The liquid water potential temperature is a quantity that does include the heat effects of phase changes. Its approximate form reads:

$$\theta_l \simeq \theta - \frac{L_v}{c_p}\frac{q_l}{\Pi},$$ (2.17)

where L_v the latent heat of condensation and Π the exner function defined by:

$$\Pi = (\frac{p}{p_0})^{-\frac{R_d}{c_p}}$$ (2.18)

(de Roode, 2004). The liquid water potential temperature is conserved for isentropic processes, unless liquid water is removed from the air by precipitation.

2.3 Governing equations

To understand and model stratocumulus formations in the atmospheric boundary layer, one can make use of conserved variables. In this section the conservation equations for mass, momentum, heat and moisture are introduced. The equations are presented in tensor notation such that repeated indices to imply a summation over $\{1, 2, 3\}$ and $(x_1, x_2, x_3) = (x, y, z)$.

Conservation of mass

The conservation of mass is described by the continuity equation:

$$\frac{\partial \rho}{\partial t} + \frac{\partial \rho u_j}{\partial x_j} = 0,$$ (2.19)

where $\vec{u}$ is the velocity. Under the assumption of incompressible air this reduces to:

$$\frac{\partial u_j}{\partial x_j} = 0.$$ (2.20)

Conservation of momentum

Navier-Stokes expresses the conservation of momentum:

$$\rho(\frac{\partial u_i}{\partial t} + \frac{\partial u_j u_i}{\partial x_j}) = -\frac{\partial p}{\partial x_i} + \frac{\partial}{\partial x_j}(\mu\frac{\partial u_i}{\partial x_i}) + F_{ijk},$$ (2.21)

where μ represents the dynamic viscosity coefficient and F denotes the external body forces acting on a parcel. There are two important body forces in the atmosphere:

the gravitational force and the Coriolis force, resulting from the Earth's rotation. The gravitational force F^g is:

$$F^g = -\delta_{i3}\rho g, \tag{2.22}$$

in which g is the gravitational constant and δ_{ij} is the Kronecker delta function. The Coriolis force F^C is:

$$F^C = -2\rho\epsilon_{ijk}\omega\eta_j u_k, \tag{2.23}$$

where ϵ is the Levi-Civita symbol, expressing the cross-product in tensor notation, ω denotes the angular velocity of the Earth and $\vec{\eta}$ is the unit vector parallel to the Earth's axis of rotation: $\vec{\eta} = (0, \cos\phi, \sin\phi)$, where the ϕ is the latitude. Furthermore with neglection of the viscosity term, because it is orders of magnitude smaller than the other terms, the equation for conservation of momentum becomes:

$$\rho(\frac{\partial u_i}{\partial t} + \frac{\partial u_j u_i}{\partial x_j}) = -\frac{\partial p}{\partial x_i} - \delta_{i3}\rho g - 2\rho\epsilon_{ijk}\omega\eta_j u_k. \tag{2.24}$$

Conservation of heat and moisture

The conservation of heat and moisture is described by:

$$\frac{\partial\Psi}{\partial t} + \frac{\partial\Psi u_j}{\partial x_j} = S_\Psi, \tag{2.25}$$

in which Ψ denotes the temperature or humidity variable and S is a sink/source term that for example can include precipitation.

Reynolds averaged heat and moisture equations

To understand the dynamics involved with stratocumulus, one can apply Reynolds averaging to obtain approximated equations for mean quantities. Reynolds averaging decomposes the variables into a mean $\overline{\Psi}$ and fluctuations around this mean Ψ':

$$\Psi = \overline{\Psi} + \Psi' \tag{2.26}$$

and subsequently averages over the entire equation. Applying this method to equation 2.25 leads to:

$$\frac{\partial\overline{\Psi}}{\partial t} + \frac{\partial\overline{\Psi' u_j'}}{\partial x_j} + \frac{\partial\overline{\Psi u_j}}{\partial x_j} = \overline{S_\Psi}. \tag{2.27}$$

If one assumes that the horizontal fluctuations around the mean will even out over time:

$$\frac{\partial\overline{\Psi}}{\partial t} + \frac{\partial\overline{\Psi' w'}}{\partial z} + \frac{\partial\overline{\Psi u_j}}{\partial x_j} = \overline{S_\Psi}. \tag{2.28}$$

With use of the product rule of differentiation and equation 2.20, this expression becomes:

$$\frac{\partial \overline{\Psi}}{\partial t} + \frac{\partial \overline{\Psi' w'}}{\partial z} + \overline{u_j}\frac{\partial \overline{\Psi}}{\partial x_j} = \overline{S_\Psi}. \tag{2.29}$$

Now one can make a distinction between the horizontal and vertical gradients:

$$\frac{\partial \overline{\Psi}}{\partial t} + \frac{\partial \overline{\Psi' w'}}{\partial z} + \overline{u_h}\frac{\partial \overline{\Psi}}{\partial x_h} + \overline{w}\frac{\partial \overline{\Psi}}{\partial z} = \overline{S_\Psi}, \tag{2.30}$$

where h denotes the summation over (x, y).

The conservation of heat in terms of the liquid potential temperature now expresses the rate of change of the mean liquid potential temperature:

$$\frac{\partial \overline{\theta_l}}{\partial t} = -\frac{\partial \overline{\theta_l' w'}}{\partial z} - \overline{u_h}\frac{\partial \overline{\theta_l}}{\partial x_h} - \overline{w}\frac{\partial \overline{\theta_l}}{\partial z} - \frac{1}{\overline{\rho}c_p}\frac{\partial \overline{F}}{\partial z}, \tag{2.31}$$

where it is assumed that there are phase changes and where F is the net radiation flux, defined by:

$$F = (lw \uparrow -lw \downarrow +sw \uparrow -sw \downarrow), \tag{2.32}$$

with lw and sw denoting the longwave and shortwave radiation respectively.

The conservation of moisture in terms of the total specific humidity is:

$$\frac{\partial \overline{q_t}}{\partial t} = -\frac{\partial \overline{q_t' w'}}{\partial z} - \overline{u_h}\frac{\partial \overline{q_t}}{\partial x_h} - \overline{w}\frac{\partial \overline{q_t}}{\partial z}, \tag{2.33}$$

where it is assumed that there is no precipitation.

With use of the conservation equations a relation can be derived between the turbulent flux at the top of the boundary layer and the difference in the conserved variable across the inversion. This derivation can be found in Lilly (1968) and holds for an infinitesimally thin inversion layer:

$$\overline{w'\Psi_T'} = -w_e\Delta\overline{\Psi}, \tag{2.34}$$

where $\Psi \in q_t, \theta_l$ and $\Delta\overline{\Psi}$ denoting the jump across the inversion layer (Lilly, 1968).

2.4 Solar zenith angle

Clouds like stratocumulus have a big influence on the radiation from the sun reaching that reaches the Earth's surface. Of course this radiation already varies in both time and space due the orbit of the Earth around the sun and the rotation of the Earth around its axis. The angle between the normal to the Earth's surface and this incoming solar

radiation, at a certain location and time, is the solar zenith angle. This angle θ_s can be calculated from the following expression:

$$cos(\theta_s) = sin(\delta)sin(\phi) + cos(\delta)cos(\phi)cos(h), \tag{2.35}$$

in which δ is the declination angle, ϕ is the latitude angle and h is the hour angle.

The inclination angle of the Earth ϵ, that is the angle between its equatorial plane and orbital plane, is $23.45°$. The declination angle, the angle between the Earth's equator and the incoming solar radiation, is dependent on this inclination angle and the position of Earth in its orbit around the sun. The position of Earth in its orbit is expressed as the day of the year N. The declination angle can then be calculated with:

$$sin(\delta) = sin(\epsilon)sin(360 \cdot \frac{284 + N}{365.24}). \tag{2.36}$$

The solar zenith angle further depends on the latitudinal position on Earth. The latitude is the angle between a line from the center of the Earth to the position on its surface and the equatorial plane. The latitudinal position of CESAR, the origin of the data used in this research, is $51.97°$.

Lastly the zenith angle varies due the rotation of the Earth around its axis. With the time t of the day in UTC and the longitudinal position on the Earth's surface x_{lon}, the hour angle h can be calculated:

$$h = x_{lon} - \pi + \frac{2\pi t}{24}. \tag{2.37}$$

Chapter 3

Data sources

This chapter treats the data sources that are used in this research. First the observational resources are discussed, namely radiosonde measurements and observations from a measurement site at Cabauw. Furthermore forecasts of two atmospheric model types have been used, namely RACMO and GALES. Lastly simulations with the DALES model were performed. The setup of those simulations will also be discussed here.

3.1 Observations

To evaluate the capability of weather models to predict stratocumulus, information is needed on the actual presence of these clouds. For this research the presence of stratocumulus is identified with observational data from the Cabauw measurement site. For further comparison also measurements are used that originate at "de Bilt".

3.1.1 CESAR

At the Cabauw Experimental Site for Atmospheric Research, abbreviated as CESAR, weather conditions are monitored. This site is situated near the center of the Netherlands, at a small town called Lopik ($51.971°$N, $4.927°$E). It contains a large set of instruments to study the atmosphere and its interaction with the land surface. A 213 meter high mast is used to measure for example the air temperature, specific humidity, wind speed and the wind direction at several heights. Furthermore measurements are made on parameters such as the cloud base height, cloud cover, the liquid water path and radiation.

The cloud base height is detected by use of the LD-40 ceilometer. (Haij et al., 2007) The ceilometer transmits laser pulses into the sky and measures the intensity of the back scatter signal as a function of time. The time between the emission and reception signal determines the height at which the back scatter occurred. The back scatter profile as a function of height is obtained by using multiple laser emissions. This profile provides information on the amount of particles in the atmosphere per height. From this

information the cloud base height is obtained. The LD-40 has a measurement range of 7.5 m to 13.6 km and operates at a resolution of 7.5 m.

Another instrument installed at CESAR is the NubiScope, which determines the cloud cover. The NubiScope uses a pyrometer to determine the temperature distribution in the sky. The pyrometer measures the irradiance and with use of StefanBoltzmann law (equation 2.6) the temperature is obtained. In an atmospheric layer the temperature increases from zenith to horizon. This change is larger for a cloudless sky then for a cloudy sky. With use this information the cloud cover is estimated.

The LWP is also measured at the Cabauw site. The apparatus used is called the HATPRO and is a microwave radiometer. The instrument measures radiant electromagnetic energy emitted by liquid water at a selected frequency to estimate the LWP.

For this research data from measurements at this site from the beginning of the year 2011 up until the end of 2012 has been used. The time interval between most of the measurements is 10 minutes. The radiation and liquid water path measurements are also available per minute. On the basis of the observation data, stratocumulus will be identified and compared with the presence of stratocumulus in the simulations.

3.1.2 Radiosonde

For comparison of the model results with observations at higher altitudes, measurements of a radiosonde are used. A radiosonde was released twice a day, at midnight and noon, at the Royal Netherlands Meteorological Institute (KNMI) measurement site "de Bilt" in the years 2011 and 2012. Nowadays the radiosonde is unfortunately only released once a day. It measures the air pressure, temperature, dew point temperature, potential temperature, water vapour specific humidity, relative humidity, wind direction and wind speed as a function of its altitude. De Bilt is situated less than 30 km from the Cabauw site, therefore it is expected that the weather conditions at the two sites are similar.

3.2 Simulation data

Atmospheric models exist in a wide variety of scales. In figure 3.1 for different types of models is shown on which scales they operate and which weather phenomena are associated with those scales. In this report three of these different model types are used.

3.2.1 RACMO

RACMO is an abbreviation for "regional atmospheric climate model". RACMO is a numerical weather production model that is used by the KNMI. The KNMI runs RACMO twice a day to obtain a three day weather forecast for Western Europe. The simulations are initialized with analysis from the European Centre for Medium-Range Weather Forecasts (ECMWF) and forced by ECMWF boundaries. (Neggers and Siebesma, 2010), (Meijgaard et al., 2008) Two RACMO data sets covering the years 2011 and 2012 are used for this research.
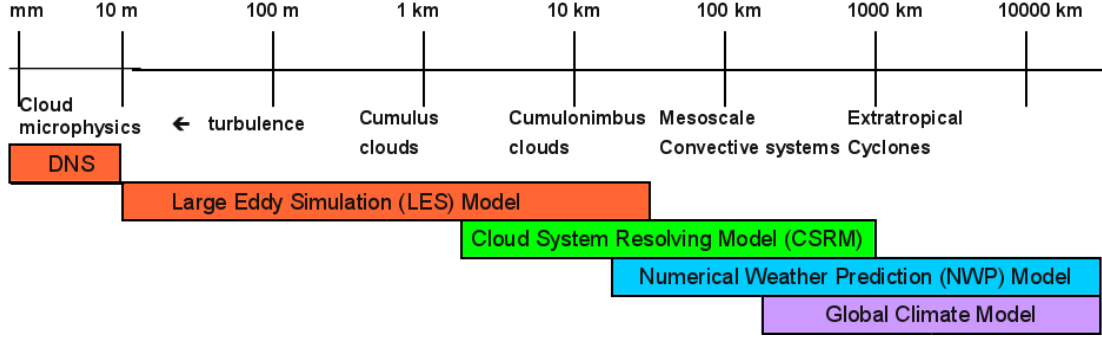
Figure 3.1: The different atmospheric model types shown together with the phenomena they are able to simulate and the scales relevant to these phenomena. (Benschop, 2013)

The data set "SCMin" (single column model input) is used to prescribe large scale forcings to the LES model as explained later on in this report. The model gives a daily forecast of three days, of which the first day is used in this research. The forecasts are initialized at 12 UTC. The set provides hourly simulation data, which in this research have been interpolated to match the 10 minute frequency of the observation data. The simulation has 91 model levels in the vertical direction, ranging from 10 m to 70 km.

The other set is obtained from a simulation especially run for this project that uses the most recent physics package (including the TKE scheme, see Soares et al. (2004)). This set is used for comparison with stratocumulus observations. The simulation gives a daily forecast of 36 hours, initialized at 12 UTC. The first 24 hours of each three day forecast is used for the analysis of the two year period. The data is available in time steps of 6 minutes, which have been converted to 10 minute intervals for comparison with the observational data with a 10 minute frequency. The radiation values are generated hourly and have also been interpolated to every 10 minutes. The simulation has 40 levels in height, covering 6 m to 30 km.

3.2.2 LES

LES stands for large-eddy simulations. The principle of LES is to resolve the larger, most energetic scales of turbulent motion and to parameterize the smaller scales. This is implemented by applying a filtering operator on the governing equations to separate the different length scales. The filter width typically can range between 1 to 50 m. (Heus et al., 2010) The filtering operation is defined by:

$$\widetilde{\phi}(\vec{x}, t) = \int G(\vec{r}, \vec{x})\phi(\vec{x} - \vec{r}, t)d\vec{r}, \tag{3.1}$$

where $\widetilde{\phi}$ is the filtered variable, ϕ the original variable, G is a normalized filter function and $\vec{r}$ is the position vector which is integrated over (Pope, 2000). The difference between the filtered variable and the original variable is defined as the residual ϕ':

$$\phi' = \phi - \widetilde{\phi}. \tag{3.2}$$

17

Filtered governing equations

The filtering operation can be applied to the governing equations as described in section 2.3. Here a homogeneous filter is used, meaning that the filter is independent of $\vec{x}$. (van der Dussen, 2009) In this case the filtered continuity equation (2.20) reads:

$$\frac{\partial \widetilde{u_j}}{\partial x_j} = 0. \tag{3.3}$$

The filtered version of the equation of motion (2.24) can be written as:

$$\widetilde{\rho}\left(\frac{\partial \widetilde{u_i}}{\partial t} + \frac{\partial \widetilde{u_j u_i}}{\partial x_j}\right) = -\frac{\partial \widetilde{p}}{\partial x_i} - \delta_{i3}\widetilde{\rho}g - 2\widetilde{\rho}\epsilon_{ijk}\omega\eta_j\widetilde{u_k}, \tag{3.4}$$

in which the unit vector $\vec{\eta}$ is assumed to be constant for the domain of the simulation. The second term in this equation can be rewritten with use of the residual-stress tensor τ_{ij}, defined as:

$$\tau_{ij} = \widetilde{u_j u_i} - \widetilde{u_j}\widetilde{u_i}. \tag{3.5}$$

Furthermore with use of the hydrostatic balance equation:

$$\frac{\partial p}{\partial z} + \rho g = 0, \tag{3.6}$$

the pressure term can be rewritten into:

$$\frac{\partial \widetilde{p}}{\partial x_i} = \frac{\partial p_0}{\partial x_i} + \frac{\partial p'}{\partial x_i} = -\delta_{i3}\rho_0 g + \frac{\partial p'}{\partial x_i}. \tag{3.7}$$

Substituting equations 3.5 and 3.7 into equation 3.4 leads to:

$$\widetilde{\rho}\left(\frac{\partial \widetilde{u_i}}{\partial t} + \frac{\partial \widetilde{u_j}\widetilde{u_i}}{\partial x_j}\right) = -\widetilde{\rho}\frac{\partial \tau_{ij}}{\partial x_j} + \delta_{i3}\rho_0 g - \frac{\partial p'}{\partial x_i} - \delta_{i3}\widetilde{\rho}g - 2\widetilde{\rho}\epsilon_{ijk}\omega\eta_j\widetilde{u_k}. \tag{3.8}$$

If it is assumed that the temperature fluctuates around a reference temperature T_0, with only small deviations, the density will vary little around reference density ρ_0. For these small variations a first order Taylor expansion can be used to approximate the density:

$$\widetilde{\rho}(\widetilde{T_v}) = \rho_0 + \frac{\partial \widetilde{\rho}}{\partial \widetilde{T_v}}\bigg|_{\widetilde{T_v}=T_0} (\widetilde{T_v} - T_0). \tag{3.9}$$

With use of the ideal gas law ($p = \rho R_d T_v$) this can be changed to:

$$\widetilde{\rho}(\widetilde{T_v}) = \rho_0 - \frac{p}{R_d T_0^2}(\widetilde{T_v} - T_0) = \rho_0 - \rho_0 \frac{\widetilde{T_v} - T_0}{T_0}. \tag{3.10}$$

With use of the Boussinesq approximation the actual LES equation can now be derived (Heus et al., 2009). The Boussinesq approximation neglects changes in the density, except in the gravity term. The equation of motion now reads:

$$\rho_0\left(\frac{\partial \widetilde{u_i}}{\partial t} + \frac{\partial \widetilde{u_j}\widetilde{u_i}}{\partial x_j}\right) = -\rho_0\frac{\partial \tau_{ij}}{\partial x_j} + \delta_{i3}\rho_0 g - \frac{\partial p'}{\partial x_i} - \delta_{i3}\widetilde{\rho}g - 2\rho_0\epsilon_{ijk}\omega\eta_j\widetilde{u_k}. \tag{3.11}$$

Finally using equation 3.10 and 2.16 and dividing with ρ_0 the following result is achieved for the conservation of momentum:

$$\frac{\partial \widetilde{u}_i}{\partial t} + \frac{\partial \widetilde{u}_j \widetilde{u}_i}{\partial x_j} = -\frac{\partial \tau_{ij}}{\partial x_j} - \frac{1}{\rho_0}\frac{\partial p'}{\partial x_i} + \frac{\widetilde{\theta}_v - \theta_0}{\theta_0}\delta_{i3}g - 2\epsilon_{ijk}\omega\eta_j\widetilde{u}_k. \tag{3.12}$$

The second term on the right hand side of equation 3.12 can be prescribed with use of the geostrophic wind as obtained from RACMO.

Lastly the filter is applied to the equations for conservation of heat and moisture (2.25):

$$\frac{\partial \widetilde{\theta}_l}{\partial t} = \frac{\partial \widetilde{u_j\theta_l}}{\partial x_j} + S_{\theta_l} = -\frac{\partial \widetilde{u}_j\widetilde{\theta}_l}{\partial x_j} + S_{\theta_l} - \frac{\partial \tau_{u_j,\theta_l}}{\partial x_j} \tag{3.13}$$

and

$$\frac{\partial \widetilde{q}_t}{\partial t} = \frac{\partial \widetilde{u_jq_t}}{\partial x_j} + S_{q_t} = -\frac{\partial \widetilde{u}_j\widetilde{q}_t}{\partial x_j} + S_{q_t} - \frac{\partial \tau_{u_j,q_t}}{\partial x_j}, \tag{3.14}$$

where τ_{u_j,θ_l} and τ_{u_j,q_t} are short notations for $\widetilde{u_j\theta_l} - \widetilde{u}_j\widetilde{\theta}_l$ and $\widetilde{u_jq_t} - \widetilde{u}_j\widetilde{q}_t$ respectively. These are the residual scalar fluxes and represent the contribution to the resolved motion from all scales below the LES filter width. The first two terms of the very right hand sight of equations 3.13 and 3.14 are large scale forcings that can be prescribed with use of RACMO data.

Closure

In order to close the equations 3.13, 3.14 and 3.12 a sub scale parametrization is needed. For heat and moisture conversation the following is used:

$$\tau_{u_j,\theta_l} = -K_{\theta_l}\frac{\partial \widetilde{\theta}_l}{\partial x_j} \tag{3.15}$$

and

$$\tau_{u_j,q_t} = -K_{q_t}\frac{\partial \widetilde{q}_t}{\partial x_j}, \tag{3.16}$$

where K_{θ_l} and K_{q_t} are eddy diffusivity constants. To close the equation for conservation of momentum one uses:

$$\tau_{ij} = -K_m(\frac{\partial \widetilde{u}_j}{\partial x_j} + \frac{\partial \widetilde{u}_i}{\partial x_i}) - \frac{2}{3}e, \tag{3.17}$$

where $\widetilde{e}$ is the subgrid turbulent kinetic energy, which is compensated for in the pressure term:

$$\pi = \frac{p'}{p_0} + \frac{2}{3}e, \tag{3.18}$$

resulting in:

$$\frac{\partial \widetilde{u}_i}{\partial t} + \frac{\partial \widetilde{u}_j \widetilde{u}_i}{\partial x_j} = -\frac{\partial \tau_{ij}}{\partial x_j} - \frac{\partial \pi}{\partial x_i} + \frac{\widetilde{\theta}_v - \theta_0}{\theta_0} \delta_{i3} g - 2\epsilon_{ijk} \omega \eta_j \widetilde{u_k}. \tag{3.19}$$

Now the only unknowns left in the governing equations are the eddy diffusivity constants K_{θ_l}, K_{q_t} and K_m. In the LES model used for this research $K_{\theta_l} = K_{q_t} = K_h$. The eddy diffusivity constants are modelled as a function of the subfilter-scale turbulence kinetic energy (SFS-TKE) e:

$$K_m = c_m \lambda e^{\frac{1}{2}}, \tag{3.20}$$

$$K_h = c_h \lambda e^{\frac{1}{2}}. \tag{3.21}$$

In these equations c_m and c_h are model constants and λ is the typical length scale of the turbulent eddies.

Lastly to close, in Heus et al. (2010) the following expression is given for this SFS-TKE:

$$\frac{\partial e^{\frac{1}{2}}}{\partial t} = -\widetilde{u}_j \frac{\partial e^{\frac{1}{2}}}{\partial x_j} + \frac{1}{2e^{\frac{1}{2}}} [K_m (\frac{\partial \widetilde{u}_j}{\partial x_i} + \frac{\partial \widetilde{u}_i}{\partial x_j}) \frac{\partial \widetilde{u}_i}{\partial x_j} - K_h \frac{g}{\theta_0} \frac{\partial (A\widetilde{\theta}_l + B\widetilde{q}_t)}{\partial z}] + \frac{\partial}{\partial x_j} (2K_m \frac{\partial e^{\frac{1}{2}}}{\partial x_j}) - \frac{c_\epsilon e}{2\lambda}, \tag{3.22}$$

in which A and B are coefficients depending on the local thermodynamic state.

3.3 DALES with use of observational data

In this report DALES 4 is used to perform simulations of selected stratocumulus cases. DALES stands for Dutch Atmospheric Large Eddy Simulation and is designed for studies of the turbulence in the atmospheric boundary layer. In DALES the radiation is calculated and doesn't need to be prescribed. The large scale forcings, such as the horizontal heat and moisture advection, do need to be provided. For these forcings RACMO SCMin simulations will be used. The initialization however, will be done with use of observations. The aim is to find out if DALES is capable of simulating stratocumulus on the basis of this data assimilation.

Setup

The horizontal domain of the simulations is 3600 by 3600 m, with a grid spacing of 50 m. The vertical spacing of the input is 10 m and the domain height is either 1275 m or 2000 m, depending on the simulation. The center of the domain matches the Cabauw measurement site, with a latitude of 52 ° and a longitude of -5 °.

Initial conditions

To initialize DALES one needs to prescribe the vertical profiles for the liquid water potential temperature and the total specific humidity at the start of the simulation. These profiles are determined with use of the CESAR and radiosonde data, under the assumption of vertically well mixed boundary layer.

Firstly the tower observations are used. Beneath the cloud layer, the liquid water specific humidity will be zero. In this case the liquid water potential temperature will be equal to the potential temperature (see equation 2.17). The total specific humidity will be equal to the water vapour specific humidity, under the assumption that there is no ice in the atmosphere (equation 2.1). Furthermore is assumed that the liquid potential temperature and the total specific humidity are constant with height up until the inversion. Therefore one can use the temperature and water vapour specific humidity as measured by the tower, beneath the cloud, to determine the value of the liquid potential temperature (with use of equation 2.7) and the total specific humidity, beneath the inversion.

Secondly, the inversion height is determined with use of the radiosonde, by locating the jump in temperature. Here it is assumed that the atmospheric conditions are horizontally homogeneous between de Bilt and Cabauw.

The third step is to prescribe the temperature and humidity profiles above the inversion height. In principle one could use the profiles as measured by the radiosonde, where the liquid water potential temperature equals the potential temperature and the total specific humidity equals the water vapour specific humidity due to the absence of liquid water above the cloud layer. However uncertainty about the reliability of the radiosonde water vapour specific humidity measurements exists because non-physical peaks in the measurements were observed across the inversion layer. Therefore the RACMO SCMin data is used to prescribe the profiles above the inversion height.

Besides the temperature and humidity profiles, the initial vertical profiles of the horizontal wind velocity in the x and y direction need to be provided to the model. For these profiles the SCMin data set is used as well. The SCMin wind profiles are averaged over the first hour of the simulation.

Large scale forcings

The sensible and latent heat flux, the geostrophic wind velocity in the x and y direction and the large scale horizontal temperature and moisture advection are provided by the SCMin data set. These forcings are prescribed to DALES on an hourly basis for the entire simulation period. Furthermore the subsidence from the SCMin data is prescribed to DALES on an hourly basis for the entire period.

DALES calculates the radiative transfer through the atmospheric column. To this end it needs information about the area above the simulation domain. The profiles needed are for ozone, temperature, water vapour specific humidity and liquid water specific humidity. The temperature and humidity profiles again originate from RACMO SCMin. The averages per RACMO pressure level are taken over the whole simulation

period. For the amount of ozone per pressure level a fixed profile is used that is shown in figure 3.2. This profile is obtained from an example case for DALES and represents the ozone in the tropics. It is assumed that this profile can be used for the simulations in the Netherlands.
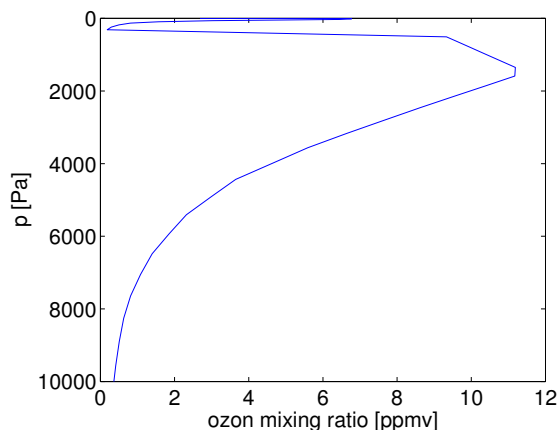
Figure 3.2: Vertical profile of the ozone mixing ratio.

3.4 GALES

In this report the representation of stratocumulus in a data set that was generated by GALES is researched. The GALES data set covers the year 2012 and was generated with a LES model which runs on a GPU (Schalkwijk et al., 2012). The domain of the simulation is about 25 by 25 km horizontally and about 13 km vertically, enclosing the Cabauw tower. The horizontal resolution is 100 by 100 m. Large scale forcings were prescribed to GALES. These forcings originate from RACMO SCMin. Also the radiation values and the initialization is based on RACMO SCMin. The incorporation of these RACMO results can of course influence the representation of stratocumulus in GALES. Therefore as part of this research simulations are performed with the LES model DALES, which is partly initialized with observational data.

Chapter 4

Stratocumulus identification

To validate the forecasting of stratocumulus under a strong thermal inversion in subsidence regions, the presence of these clouds needs to be verified in both the observation and simulation data. This verification is done with use of a set of criteria for the atmospheric conditions. The choice of the criteria will be explained in section 4.1. To compare the simulations and observations in more detail, also four other situations with a strong thermal inversion and in regions of subsidence are identified. These categories and their criteria are discussed in section 4.3.

4.1 Criteria

To identify the stratocumulus moments a set of four criteria is used. The criteria are listed in table 4.1.

Table 4.1: stratocumulus criteria

criterion			selection	source
LTS	$>$	15 K	inversion present	RACMO
$\overline{w}$	$<$	0 ms^{-2}	subsidence region	RACMO
cloud base height	$<$	1 km	low cloud	observation, RACMO, GALES
cloud cover	$\geq$	0.9	homogeneous cloud	observation, RACMO, GALES

This research focuses on stratocumulus under a strong thermal inversion. Therefore firstly a selection is made on the presence of such an inversion. The meteorological tower, however, has a height of about 200 m, while the stratocumulus clouds typically occupy the upper few hundred meters of the Planetary Boundary Layer (PBL). Observation data above 200 m are available from the radiosonde measurements, but this data is only available twice a day in 2011 and 2012. Therefore the presence of a strong thermal inversion is checked with the use of LTS data from RACMO. The RACMO simulations were initialized once a day with the radiosonde data. Therefore it is expected that the temperature profile in RACMO is quite accurate. In chapter 5 of this report this assumption will be checked. However, the depth of the inversion layer can be very shallow

(20-50 m), which is much smaller than the vertical grid of RACMO. The inversion layer is therefore spread out in this model and the strong inversion cannot be detected directly. For the calculation of the LTS the vertical resolution of RACMO is not a problem. To calculate the LTS, the temperature is needed at only 2 levels: at the surface and at a height of about 3 km. Therefore it is expected that the LTS calculated from the RACMO data with use of equation 2.7 and 2.8, can be used as an approximate for the presence of a strong thermal inversion. The LTS criteria is set to be at least 15 K. For example: for a (maximum) inversion height of 1.2 km and a roughly estimated potential temperature lapse rate of 6 K/km above the inversion, this would be a jump of at least 4 K. The research of Klein and Hartmann (1993) showed a strong correlation between the LTS and the formation of stratocumulus. In the identified regions with a high stratocumulus occurrence, the maximum LTS ranges from 15 to 28 K and occurs in the season with the maximum amount stratocumulus.

Secondly the selection is further refined upon the presence of subsidence. If the average vertical velocity between the surface and 3 km is negative (downwards), the region is regarded as a subsidence region. As with the calculation of the LTS, the calculation of this mean average velocity is done with use of the RACMO data. The presence of subsidence in combination with the high LTS leads to the selection of stable weather conditions and excludes the deep convection.

The third criterion used for selecting stratocumulus is the cloud base height. As mentioned earlier stratocumulus belongs to the class of low clouds with a cloud base height below 2 km. Therefore the cloud base height criteria is set to be less than 1 km.

The fourth criterion is a cloud cover of 0.9 or higher. The cloud cover is the horizontal projection of the cloud fraction. Since the cloud fraction of stratocumulus is close to unity, the cloud cover of stratocumulus will also be close to one.

Note that cloud base height measurements are point measurements, while cloud cover measurements evaluate an area of the sky. Therefore it is possible that no cloud base height is detected while the cloud cover is larger than 0.

The identification stratocumulus is thus based on a RACMO LTS above 15 K, a negative average vertical velocity between the surface and 3 km from RACMO, a cloud base height of less than 1 km and a minimum cloud cover of 0.9.

4.2 Selection of time periods with persistent stratocumulus

With use of the criteria presented in table 4.1 the moments in 2011-2012 for which a stratocumulus cloud deck is present can be selected. To identify periods of persistence stratocumulus another two criteria are applied. The first criterion for the selection of stratocumulus periods is that the stratocumulus must be observed for at least 3 hours (18 subsequent data points). A table with the resulting selected cases is added to appendix A, in which the starting date and time in UTC as well as the total length of the periods in hours are indicated. The second criterion is applied to the grouping of subsequent stratocumulus moments. If no more than one subsequent moment within a

period of observed stratocumulus does not fulfil the stratocumulus conditions, the two stratocumulus periods will be combined to one period.

With use of the same method also the stratocumulus periods in RACMO and GALES are selected. For consistency the selection on the LTS and the subsidence is always done with RACMO. Furthermore if one of the cloud cover or cloud base height is not available in the observational data, the period is disregarded. The resulting cases for which at least 50% of the period is also identified as stratocumulus in the observations, are listed in table A.1 and A.2. The remaining cases are listed separately in tables A.3 and A.4 for RACMO and GALES respectively.

4.3 Boundary layer types with a high LTS and in regions of subsidence

Besides the presence of stratocumulus during conditions with a high LTS and subsidence, also four other boundary layer types are identified. These categories are: shallow cumulus, other low broken clouds, a clear boundary layer and a category for those conditions who fit none of the others. An overview of the criteria used for each situation is given in table 4.2. For all the categories the LTS criterion is set to be larger than 15 and the presence of subsidence is checked by a negative average vertical velocity between the surface and 3 km.

Table 4.2: Boundary layer types during a high LTS and subsidence

boundary layer type	z_{base}	cloud cover
stratocumulus	< 1 km	≥ 0.9
shallow cumulus	< 1 km	≤ 0.4 & > 0.1
other low broken clouds	< 1 km	< 0.9 & > 0.4
clear		≤ 0.1
other		

With use of these criteria one can find out what weather conditions are modelled when no stratocumulus is predicted while it is observed and what is observed if stratocumulus is modelled but not measured. Here will follow a short description of the boundary layer types and their criteria.

Shallow cumulus is characterized by its broken structure and small cloud cover. It also belongs to the class of low clouds. Therefore the criteria of a cloud base height below 1 km is used. The cloud cover is set to be between 0.4 and 0.1. This is in agreement with the classification used by Xu et al. (2008). However the cloud cover is a difficult quantity to both measure and simulate. Therefore it might be considered to take merge this category into other low broken clouds.

The category of other low clouds consists of again a cloud base height below 1 km. Furthermore the cloud cover lies between that for stratocumulus and shallow cumulus, thus between 0.4 and 0.9.

The clear boundary layer is identified by use of a cloud cover upper limit of 0.1.

Lastly the parts of the subset of high LTS situation that don't fit into any of the identified boundary layer types are grouped to the category "other".

The sensitivity of the stratocumulus criteria has been assessed. In appendix B is shown what the effect on the selection is for changes in each of the criteria.

Chapter 5

Stratocumulus climatology at Cabauw

In this chapter some of the climatology of stratocumulus at the Cabauw measurement site will be discussed. The criteria discussed in section 4.1 are used to identify the stratocumulus presence in the 2 years of observation data and as well in the simulated data. The occurrence of the different LTS values in combination with the specific humidity, the cloud base height probabilities and wind directions have been assessed. Furthermore the influence of stratocumulus clouds on the solar irradiance is researched. The horizontal homogeneity between Cabauw and de Bilt is researched by comparing the vertical profiles of the potential temperature and the water vapour specific humidity.

5.1 LTS and total specific humidity

The joint probability density function of the LTS and the total specific humidity difference between 3 km and 10 m calculated with RACMO, is visualized in the top graph of figure 5.1. The occurrence is normalized by the total amount of data points. It is found that the most frequently occurring combination is an LTS of about 11 K with a difference in specific humidity of -4 g/kg.

Next a selection is made on the presence of subsidence, a cloud base height below 1 km and a cloud cover greater than or equal to 0.9. The frequency of occurrence as a function of the humidity difference and the LTS is shown in the middle of figure 5.1. The occurrence is again normalized by the total amount of data points. The highest probability on a low uniform cloud deck in a subsidence region is for an LTS around 15 K in combination with a humidity difference of about -4 g/kg. Note for an LTS below 15 K low clouds also occur, but between 15 and 20 K the probability is highest.

The bottom graph of figure 5.1 indicates frequency of occurrence as a function of the humidity difference and the LTS of an observed clear boundary layer in a subsidence region. The observed clear boundary layer is identified by a cloud cover less or equal to 0.1. As before the occurrence is normalized by the total amount of data points. The color bar distribution is kept the same as the middle graph. The highest chance on a
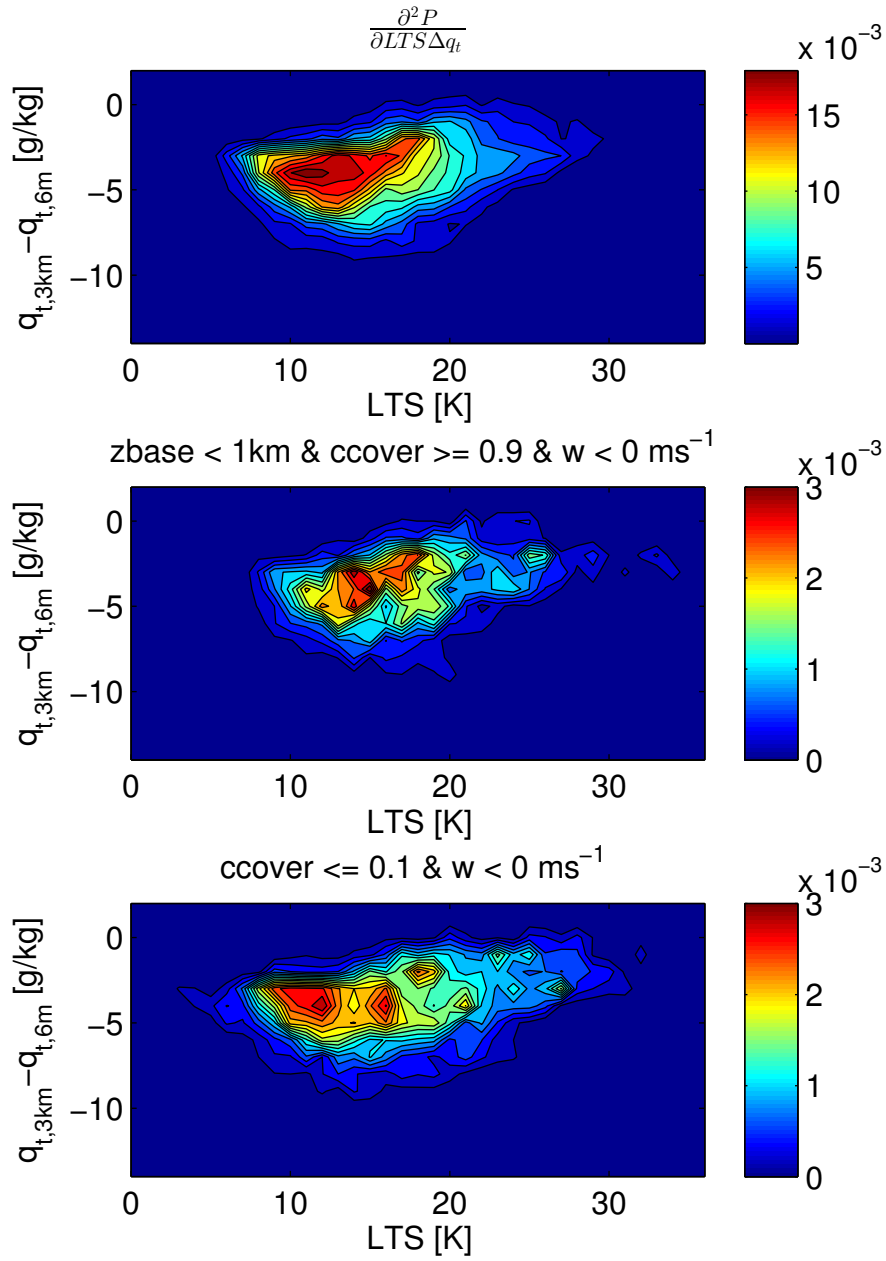
Figure 5.1: Joint probability density functions of the LTS (x-axes) and the difference in total specific humidity between 3 km and 10 m (y-axes) from RACMO. Top graph visualizes the occurrence of the LTS and humidity difference combinations. The middle graph shows the probability of a observed cloud base height below 1 km and an observed cloud cover of at least 0.9 in combination with a negative average vertical velocity between 10 m and 3 km as obtained from by RACMO. The bottom graph illustrates the occurrence of a observed clear boundary layer, identified by an observed cloud cover of maximum 0.1, in a subsidence region as identified with RACMO.

clear sky occurs for a humidity difference of about -4 g/kg in combination with a LTS of 12 K. Note that the humidity difference of about -4 g/kg is the most frequently occurring humidity difference, as shown in the top graph.

The joint probability density functions as made for the observational data in 5.1 are also generated for the RACMO data, as shown in figure 5.2. (The top figure of 5.1 will of course be the same, since the LTS and humidity difference are in both cases determined with RACMO.) The top graph of figure 5.2 indicates the presence of low uniform clouds in a subsidence region in RACMO. In comparison with figure 5.1 it shows that there are less low uniform clouds present in RACMO than observed. The distribution of the probability is similar. The bottom graph of figure 5.2 shows the probability of a clear boundary layer in a subsidence region in RACMO. In comparison with figure 5.1 it shows that there is a higher probability of a clear boundary layer in RACMO than is observed, but the distribution of the probability is again similar.
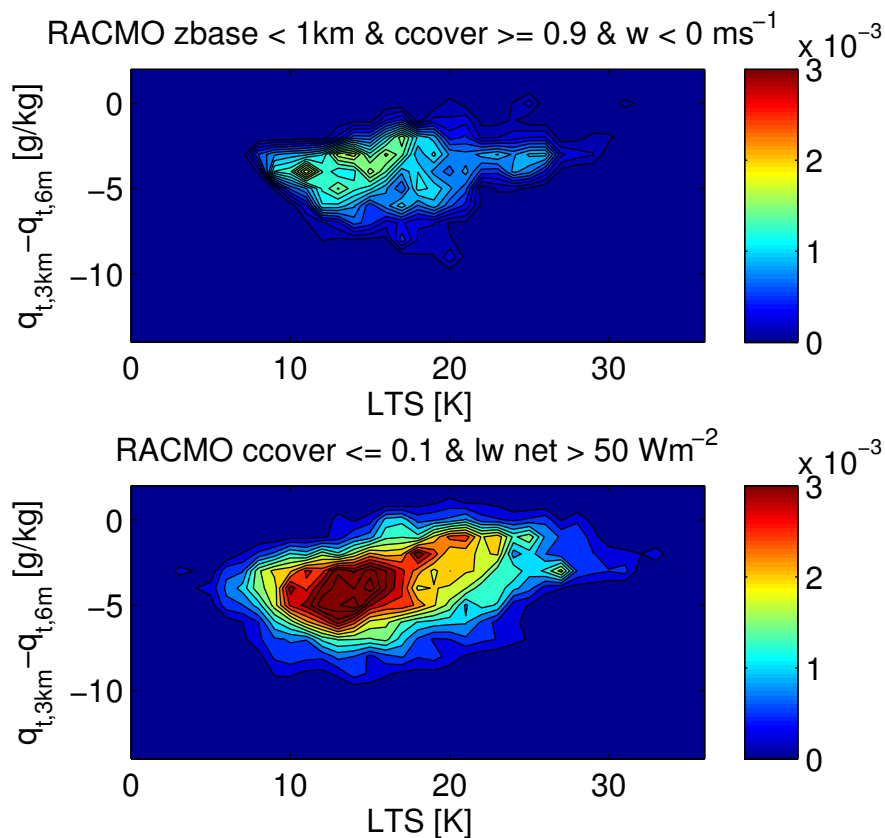
Figure 5.2: Joint probability density functions of the difference in total specific humidity between 3 km and at 10 m and the LTS. The top figure shows the probability of a cloud base height below 1 km and a cloud cover of at least 0.9 in RACMO, for a negative average velocity between 10 m and 3 km. The bottom figure illustrates the probability of a cloud cover below 0.1 in RACMO, for a negative average velocity between 10 m and 3 km.

5.2 Cloud base height

Figure 5.3 compares the measured cloud base height with the simulated cloud base height in RACMO and GALES. The upper graph shows the probability of different cloud base heights for the whole data sets and the lower graph shows the probability for the identified stratocumulus cases in the observations. The vertical resolution of RACMO is taken as a basis for the cloud height bins, since RACMO has the lowest resolution. Looking at the upper graph it shows that cloud base height below 2000 m are most common. The highest probability occurs around a height of 250 m, for both observations and the GALES. The lower graph shows that stratocumulus cloud base heights below 500 meters are less likely in RACMO than is observed. The probabilities of the stratocumulus cloud base heights in GALES are in general lower than in the observations.
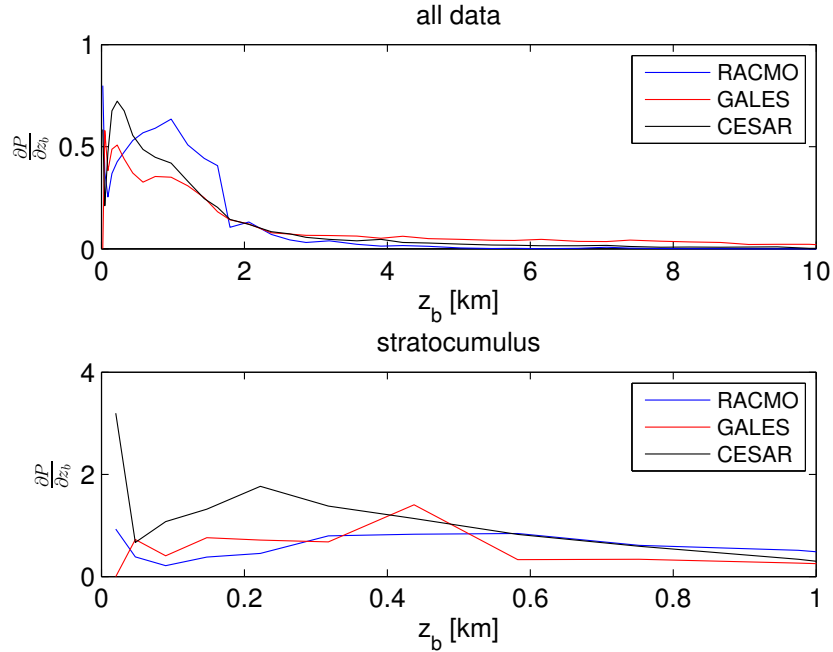
Figure 5.3: The top graph shows the probability density function of the cloud base heights in the observations (black), RACMO (blue) and GALES (red). The lower graph shows the probability density function of the cloud base heights at identified stratocumulus moments in the observations.

5.3 Wind

In figure 5.4 the distribution of the wind direction is illustrated, for both the complete data set and the selected stratocumulus cases. It can be seen that the most common wind direction at CESAR is the south-west. For the identified stratocumulus cases the distribution is slightly different. Stratocumulus hardly occurs with a north-west or

south-east wind and is most common with a south-west or north-east wind.
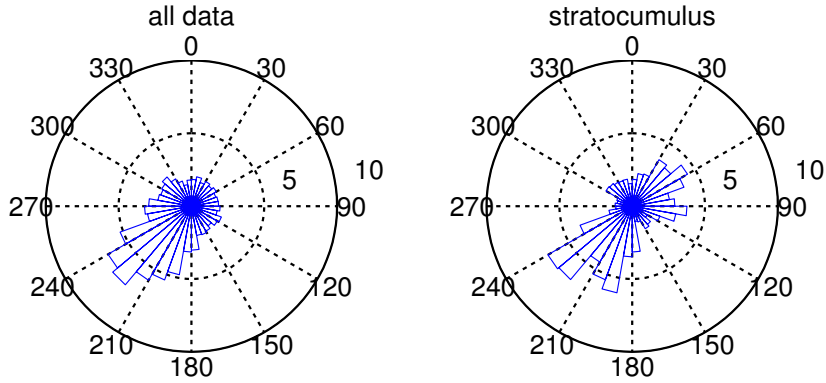
Figure 5.4: Wind rose plots showing the distribution of wind directions in degrees for the complete data set (left) and for the stratocumulus cases (right). The length of the bars indicate the percentage of the total data points.

Figure 5.5 shows the probability density function of the wind speed measured at a height of 80 m. The distribution of all wind speeds at this height is similar to the distribution of wind speeds under stratocumulus conditions, but stratocumulus peaks at a slightly less strong wind.
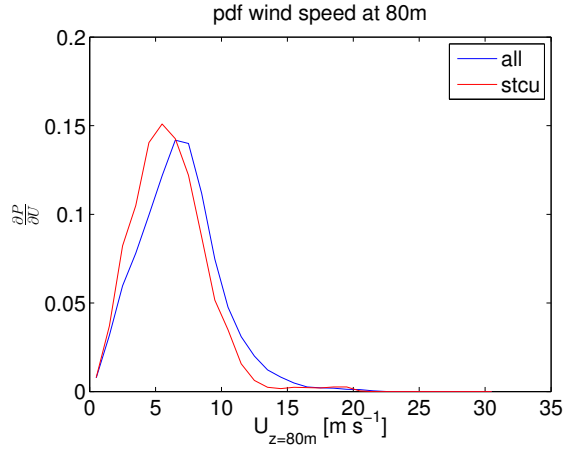
Figure 5.5: The probability density function of the wind speed at a height of 80 m. Blue indicates the probability as calculated with the complete data set of 2011-2012, while red is showing the probability for stratocumulus moments only.

5.4 Solar irradiance

Stratocumulus clouds have a big influence on the down welling shortwave radiation from the sun that reaches the ground. In the left of figure 5.6 this is illustrated by plotting

the down welling shortwave radiation measured at CESAR as a function of the solar zenith angle. The highest radiation values are likely corresponding to a clear sky, since then there are no clouds to reflect and absorb the sunlight. The light blue line is a fit through the highest point density in the top 20% radiation values per zenith angle interval. The points far above the blue line are possibly caused by side reflections of broken clouds. In the graph the identified stratocumulus cases under a strong thermal inversion are indicated by a red circle. The pink line is the average of the down welling shortwave radiation per zenith angle, under this stratocumulus. There is clearly a big difference between the radiation that reaches the ground under a clear sky (light blue line) and under a stratocumulus topped boundary layer (pink line).
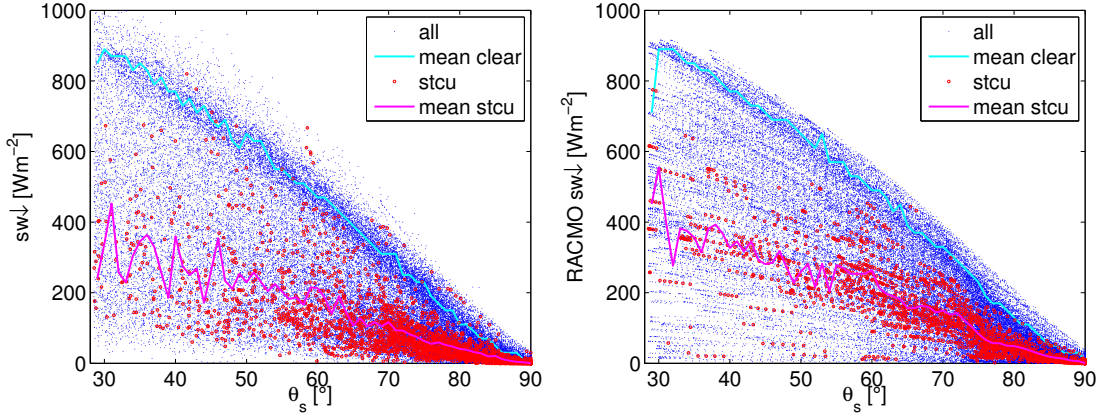
Figure 5.6: **Scatter plot of the downwelling short wave radiation at CESAR (left) and in RACMO (right) as a function of the solar zenith angle is plotted in blue. The points in these plot that represent observed (left) or simulated (right) stratocumulus are indicated with a red circle. The light blue line is a fit through the highest density of points in the highest 20% downwelling shortwave radiation per zenith angle interval. The pink line shows the average of shortwave radiation under stratocumulus.**

The same figure is made for the RACMO simulated downwelling shortwave radiation, shown in the right of 5.6. The red circles indicate the points that are identified as stratocumulus in RACMO. The top band of the RACMO figure is better defined than the top band of the observations. This is because the concentration of aerosols is constant in RACMO. In the observations differences occur in this concentration, for example depending on the wind direction. Aerosols increase reflection and absorption of solar radiation by the atmosphere and therefore reduce the shortwave radiation reaching the Earth's surface. The clear sky radiation fit is very similar as found in the observations. Comparing the radiation under stratocumulus conditions in the model with the observations however, shows that for RACMO this radiation is on average a bit higher.

The downwelling shortwave radiation, swd, from the sun that reaches the surface of the Earth is reduced by the presence of clouds. Clouds will partly absorbed and reflect the solar radiation:

$$swd_{transmitted} = swd_{total} - swd_{reflected} - swd_{absorbed}. \tag{5.1}$$

Here, the total radiation is defined as the radiation at the surface under a clear sky. If the absorbed radiation is neglected, the difference between the downwelling shortwave radiation at the surface under a clear and a stratocumulus topped boundary layer can thus be used as a rough estimation for the reflected solar radiation by stratocumulus clouds:

$$swd_{reflected} = swd_{clear} - swd_{transmitted}. \tag{5.2}$$

The reflected solar radiation can furthermore be normalized on the clear sky radiation:

$$swd_{reflected} = \frac{swd_{clear} - swd_{transmitted}}{swd_{clear}}. \tag{5.3}$$

The left of figure 5.7 shows the difference between the pink and light blue line from figure 5.6, as a percentage of the fitted clear sky values. It is shown that the reflection by stratocumulus is around 0.65 for the observations, which is in agreement with the albedo values found in literature. The reflection in RACMO is slightly lower than is observed for an angles below $80°$.
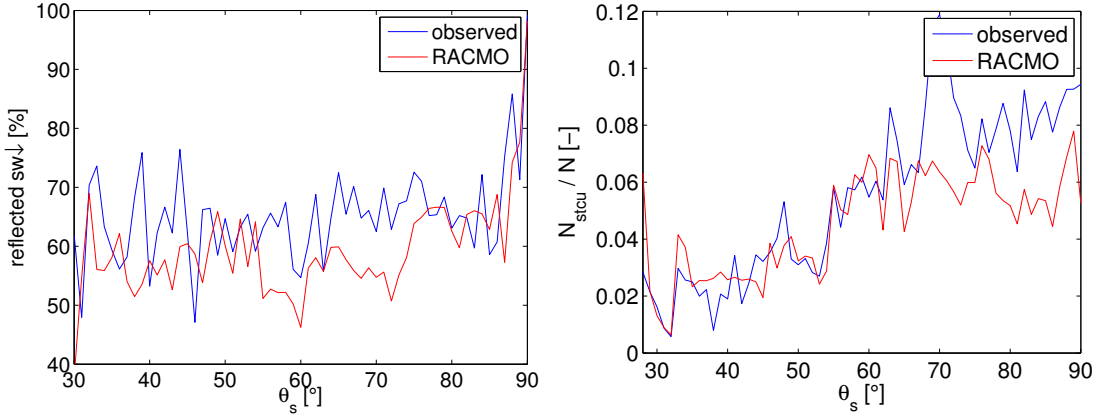
Figure 5.7: Left: estimated fraction of solar radiation reflection by stratocumulus, as a function of the solar zenith angle, for both the observations (blue) and RACMO (red). Right: The number of selected stratocumulus points as a fraction of the total points per solar zenith angle, for both observations (blue) and RACMO (red).

In the right of figure 5.7 the occurrence of stratocumulus normalized with the occurrence of the solar zenith angle is shown as a function of the angle for both observations and RACMO. Both plots show an increase in occurrence per rising zenith angle. The increase suggest that stratocumulus is more likely to develop and maintain when the sun is low. This means that stratocumulus occurs most in winter and in the morning/evening. Furthermore it is shown that for zenith angles above 65 $°$ stratocumulus occurs less in RACMO than is observed. Lastly note that the frequency of occurrence per zenith angle does not rise above 10%.

5.5 Horizontal homogeneity between Cabauw and de Bilt

To initialize the simulation with DALES the inversion height, determined from the radiosonde measurements, is used, as discussed in section 3.3. It is assumed that the atmospheric conditions between de Bilt and Cabauw are horizontal homogeneous and that the inversion height will therefore be similar. In this section the horizontal homogeneity is researched by comparing the vertical profiles of the potential temperature and the water vapour specific humidity as measured at Cabauw with the profiles obtained from the radiosonde at de Bilt. Since the weather balloon at de Bilt is released at 12 and 00 UTC in 2011 and 2012, the comparison is only done for these moments.

In figure 5.8 the root mean square errors (RMSE's) of the radiosonde measurements with respect to the tower measurements are shown per tower height. For the calculation, the radiosonde data is linear interpolated to the tower level heights.
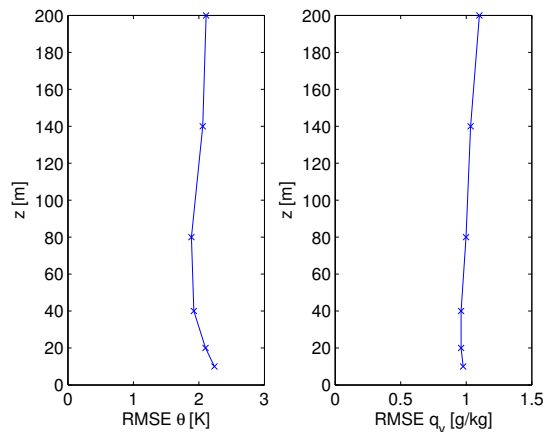
Figure 5.8: The RMSE per tower level height for the potential temperature (left) and the water vapour specific humidity (right) of the tower measurements at Cabauw with respect to the radiosonde measurements at de Bilt at 00 and 12 UTC.

The RMSE of the potential temperature between the tower and the radiosonde is around 2 K. The RMSE of the water vapour specific humidity is about 1 g/kg. Significant differences in the potential temperature and water vapour specific humidity can thus occur between de Bilt and Cabauw and the atmospheric conditions are not always horizontally homogeneous.

In figure 5.9 the average potential temperature and water vapour specific humidity at 00 and 12 UTC is shown per tower level height.
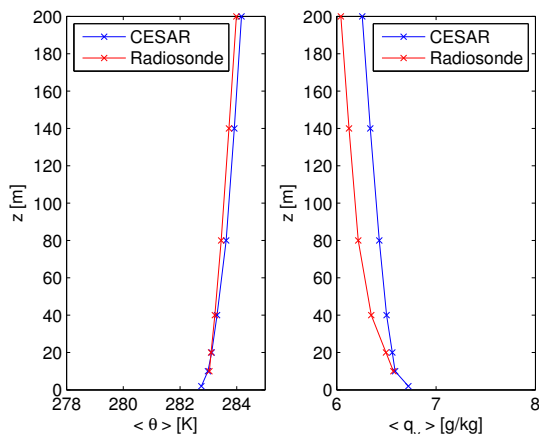
Figure 5.9: The average potential temperature (left) and water vapour specific humidity (right) at 00 and 12 UTC per tower level height as observed at Cabauw (blue) and at de Bilt (red).

The averages show that the radiosonde observations are in general slightly colder and dryer. Furthermore it is shown that the differences increase with the tower height.

5.6 RACMO temperature and humidity profiles compared with the radiosonde

The LTS and subsidence from RACMO are used for defining a data subset in which stratocumulus cases are identified in the observations, RACMO and GALES. In this section the potential temperature (with which the LTS is calculated) and the water vapour specific humidity of RACMO are compared with the weather balloon measurements. This way an indication of the uncertainties in the RACMO profiles can be obtained.

In figure 5.10 RMSE of RACMO with respect to the radiosonde measurements at 12 and 00 UTC is shown per RACMO level height for the potential temperature and the water vapour specific humidity. For the calculation, the radiosonde data is linearly interpolated to the RACMO levels.

It is shown that at 12 UTC the RMSE's for both the potential temperature as well as for the water vapour specific humidity are smaller than at 00 UTC. This is not surprising since RACMO is initialized at 12 UTC. At 00 UTC the RMSE of the potential temperature is about 2 K higher than at 12 UTC. To calculate the LTS, the potential temperature at the surface and at a height of 3 km is used. At the surface the RMSE is between 1 and 3 K and at a height of 3 km between 2 and 4 K, which is quite large. The RMSE of the water vapour specific humidity is about 0.5 g/kg higher at 00 UTC than at 12 UTC.
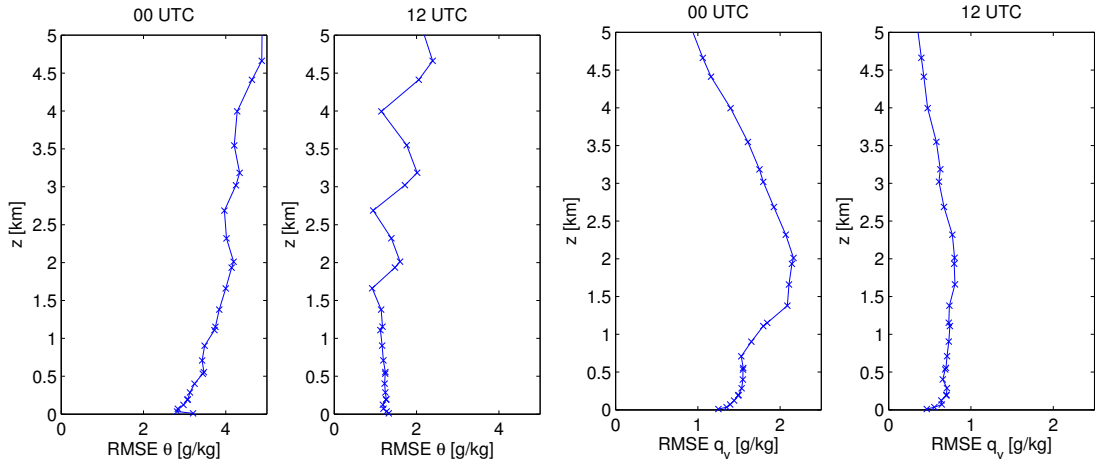
Figure 5.10: RMSE per RACMO height with respect to the radiosonde measurements for the potential temperature (left 2 graphs) and the water vapour specific humidity (right 2 graphs) at 00 and 12 UTC.

In figure 5.11 the average potential temperature and water vapour specific humidity per RACMO level height are shown for RACMO and the radiosonde at 00 and 12 UTC.
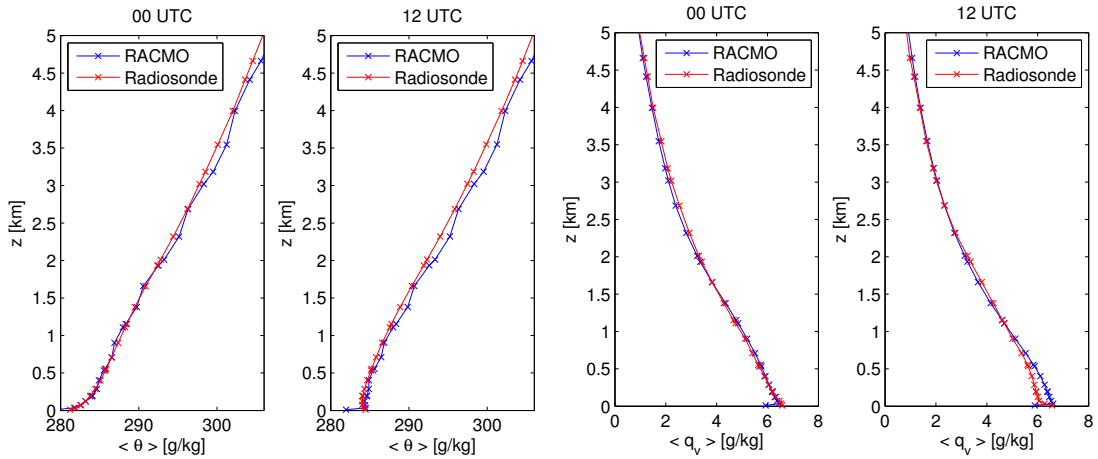
Figure 5.11: Average potential temperature (left 2 graphs) and water vapour specific humidity (right 2 graphs) at 00 and 12 UTC per RACMO height for RACMO (blue) and the radiosonde measurements (red)

It is shown that the potential temperature averages of RACMO often slightly lower than as calculated with the radiosonde observations, especially at 12 UTC. The averages of the water vapour specific humidity in RACMO are sometimes lower and sometimes higher than as obtained from the radiosonde. No systematic bias is found.

The RACMO SCMin dataset is used to prescribe large scale forcing to DALES. Therefore the comparison with the radiosonde profiles is also done with the SCMin data set (also see section 3.2.1). The RMSE per RACMO height is shown in figure 5.12. In this case the radiosonde data is linear interpolated to the SCMin level heights.
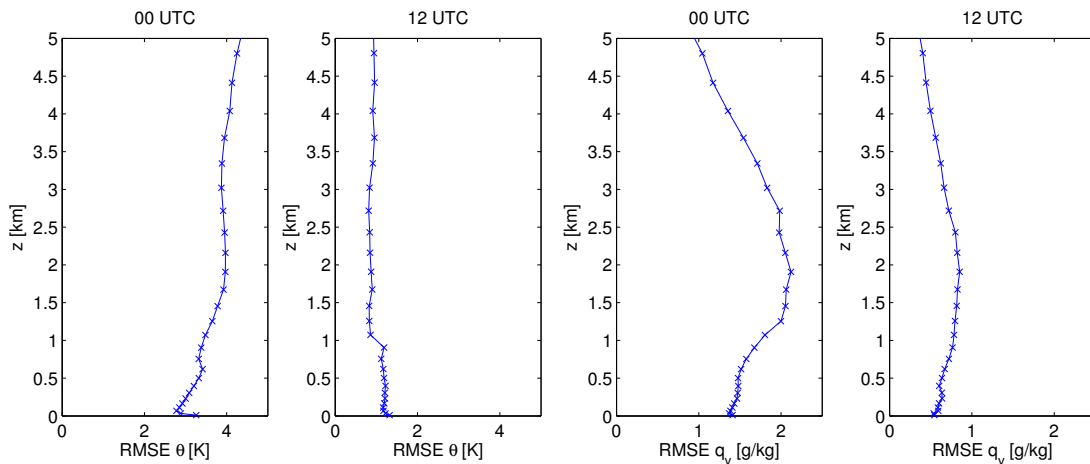
Figure 5.12: RMSE per SCMin height with respect to the radiosonde measurements for the potential temperature (left 2 graphs) and the water vapour specific humidity (right 2 graphs) at 00 and 12 UTC.

The RMSE of the potential temperature and the water vapour specific humidity of the RACMO SCMin dataset with respect to the radiosonde measurements also show that at 12 UTC the RMSE's are smaller than at 00 UTC. For the potential temperature RMSE the difference is about 2 K and for the water vapour specific humidity RMSE it is around 0.5 g/kg. These values were also found with the RACMO TKE data.

In figure 5.13 the average potential temperature and water vapour specific humidity per SCMin RACMO level height at 00 and 12 UTC are shown for RACMO SCMin and the radiosonde.

The averages as found with the SCMin dataset are close to the averages as found with the radiosonde measurements. At 00 UTC the potential temperature averages are slightly lower than as obtained with the weather balloon. Below a height of 2 km the average water vapour specific humidity is slightly higher in SCMin than as observed with the radiosonde.
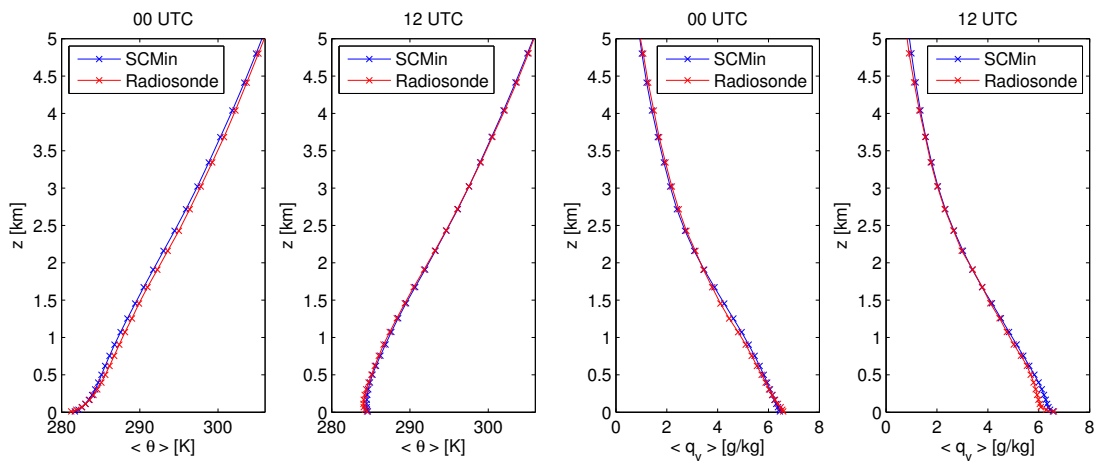
Figure 5.13: Average potential temperature (left 2 graphs) and water vapour specific humidity (right 2 graphs) at 00 and 12 UTC per SCMin height for RACMO SCMin (blue) and the radiosonde measurements (red)

Chapter 6

Stratocumulus representation in RACMO and GALES

The method to identify stratocumulus from the observation data, as described in chapter 4.1 can also be used to select the stratocumulus in the simulations. In this chapter simulation data from RACMO and GALES will be compared with observations. The periods with stratocumulus in RACMO and GALES, as selected according to section 4.2, are listed in appendix A.

6.1 Downwelling shortwave radiation

Stratocumulus has a large impact on the shortwave radiation from the sun that reaches the Earth's surface. The modelled downwelling shortwave radiation at the surface is therefore compared with the observations. In figure 6.1 the radiation in RACMO is scattered against the observed radiation. There is a slight positive bias visible. This positive bias is confirmed by the difference in mean downwelling shortwave radiation of the whole period. The observed mean is 119 Wm^{-2}, while that of RACMO is a bit higher: about 125 Wm^{-2}. The identified observed stratocumulus moments, with use of the criteria listed in table 4.1, are encircled with red. It can be seen that on average these points follow a steeper slope than the blue dots. This could be a indication for the under prediction of stratoculumus in RACMO. If the cloud deck is missing, there will be more solar radiation reaching the ground. RMSE between RACMO and the observation data is 90 Wm^{-2}. For the observed stratocumulus points the RMSE is 65 Wm^{-2}.

6.2 Quality matrices

With the method described in section 4.3, subsets of the observation, RACMO and GALES data with a LTS higher than 15 K and in a subsidence region are further divided over 5 categories. These categories are stratoculumus (stcu), shallow cumulus (shcu), other low broken clouds (low br), clear boundary layer (clear) and other. For consistency,
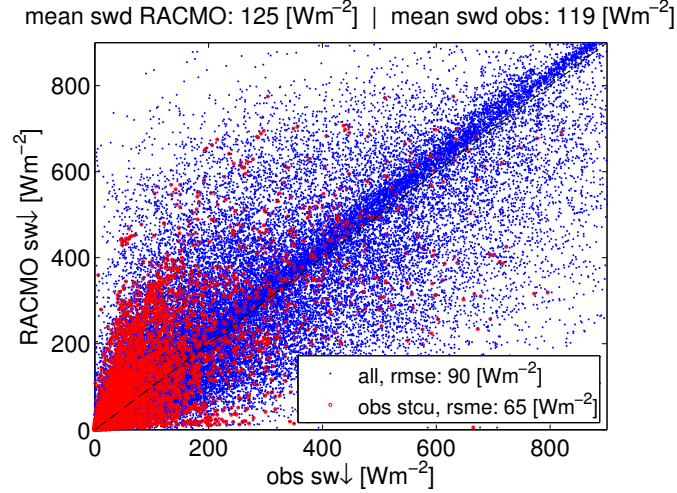
Figure 6.1: Scatter plot of the downwelling shortwave radiation in RACMO as a function of the observations. The total mean of the model and of the observations is given above the figure. The identified observed stratocumulus points are indicated with red circles. The RMSE of the model with respect to the observations is given in the legend.

the LTS and subsidence criteria used for the identification are taken from RACMO. The resulting selections are compared with use of the so-called "quality matrices". In these matrices the fractions of the observed selections that correspond to each of the five model selections are shown. Each row represents one of the observed categories. The columns indicate the number of modelled cases that correspond to the observed category as a fraction of the observed cases. Thus ideally, when all modelled cases match the observed type, the quality matrix is a unity matrix. It is important to note that the subset of the data for which the LTS is higher than 15 K and the average vertical velocity between the surface and a height of 3 km is negative, is only 15 % of the total data points in 2011 and 2012.

In table 6.1 the quality matrix of RACMO versus the observations is shown. It shows that only 41 % of the identified stratocumulus cases in the observations are also identified as stratocumulus in RACMO. 23 % of the time the stratocumulus is identified as shallow cumulus or other low broken clouds. 22 % is even identified a clear, which will for example give a large difference in predicted and actual solar radiation. Looking at the RACMO column for stratocumulus it is shown that stratocumulus is also identified in the model while it is not observed. 42 % of the times that shallow cumulus is identified in the observations, stratocumulus is modelled. Further it is noticed that RACMO is most in agreement with the observational data for the clear atmosphere category. 54 % of observed clear moments are also identified as clear in RACMO.

In table 6.2 the quality matrix of GALES versus the observations is shown, with use of data from 2012 only. The subset of the data in 2012 for which the LTS and subsidence criteria hold is only 6 % of the total data points for that year. Therefore one must keep in mind that the number of data points identified as one of the boundary layer types

Table 6.1: Quality matrix of RACMO (R) for 2011–2012. For each observed boundary layer type (rows) it is shown which fraction of the observed cases are modelled as the various boundary layer types (columns).

	R stcu	R shcu	R low br	R clear	R other
obs stcu	**0.41**	0.05	0.18	0.22	0.14
obs shcu	0.42	**0.05**	0.15	0.26	0.11
obs low br	0.33	0.05	**0.24**	0.22	0.16
obs clear	0.15	0.04	0.07	**0.54**	0.20
obs other	0.11	0.04	0.08	0.45	**0.32**

might be too little to obtain statistical reliable results.

Table 6.2: Quality matrix of GALES (G) for 2012. For each observed boundary layer type (rows) it is shown which fraction of the observed cases are modelled as the various boundary layer types (columns).

	G stcu	G shcu	G low br	G clear	G other
obs stcu	**0.42**	0.01	0.03	0.20	0.34
obs shcu	0.63	**0.00**	0.02	0.09	0.26
obs low br	0.49	0.00	**0.01**	0.17	0.33
obs clear	0.20	0.01	0.03	**0.34**	0.41
obs other	0.09	0.01	0.01	0.31	**0.58**

First it is noticed that GALES scores a only a little bit higher than RACMO for modelling stratocumulus when it is observed, namely 42 %. 34 % of the observed stratocumulus is classified as the category others in GALES. Also clear weather seems to be under predicted for the LTS subset, 34 % of the identified clear conditions in the observations are also found in GALES. Looking at the GALES column for stratocumulus it is seen that also in GALES stratocumulus is identified when another category is observed. 63 % of the identified shallow cumulus in the observations are identified as stratocumulus in GALES. However it was found that the frequency of occurrence of the observed shallow cumulus boundary layer type in a subsidence region and with a LTS higher than 15 K is only 0.4 % in 2012. For other types of low broken clouds the frequency of occurrence in 2012 as found with the observational data is 0.6 %. The number of data points that are identified as these two boundary layer types is thus too little to obtain a fair comparison between observations and predictions.

Chapter 7

LES results

In this chapter the results of the simulations with DALES are discussed. Four periods of 24 hours were simulated, during which stratocumulus was identified in the observations. The results are compared with the observations, RACMO and when available GALES.

7.1 Methodology

The setup of the simulations is described in section 3.3. Observational and RACMO SCMin simulation data is used to initialize and prescribe large scale forcings to DALES. The use of the RACMO data as well as the observational data comes with uncertainties. Therefore besides the setup as described in section 3.3, more simulations are performed, for which the forcings and input parameters are slightly adjusted. With use of an ensemble of simulations a "plume" prediction is created, which shows the sensitivity of the prediction to small changes in the input parameters. The sensible and latent heat flux from the RACMO SCMin dataset is prescribed to the DALES simulations. These fluxes are also measured at CESAR. Therefore an additional DALES simulation is done with use of the observational latent and sensible heat fluxes. The initial potential temperature and water vapour specific humidity profile above the inversion height is prescribed with use of the RACMO SCMin data. Another DALES run is done with use of the radiosonde profiles above the inversion height instead. Furthermore the setup assumes horizontal homogeneity between de Bilt and Cabauw for determining the initial inversion structure. In reality the inversion height at Cabauw can differ from the inversion height at de Bilt. Therefore an additional simulation is done with an adjusted initial inversion height (either increased or decreased). Lastly an additional simulation is done with an increased or decreased subsidence over the entire height and period. In this chapter the additional DALES simulation results will be shown with dotted lines in the following colours:

1. prescribing the observational sensible and latent heat flux (PURPLE)
2. prescribing the initial potential temperature and humidity profile above the inversion height as measured by the radiosonde (YELLOW)
3. adjusting the initial inversion height (GREEN)
4. adjusting the subsidence over the entire height and period (RED)

7.2 Simulation 18 February 2011

A stratocumulus period is identified from the observational data on the 18th of February 2011, starting at 17:20 UTC and lasting 11.3 hours (see table A.1). In figure 7.1 an infrared satellite image is shown of the stratocumulus cloud deck at 18:00 UTC.

Figure 7.1: Infrared satellite image of stratocumulus cloud deck above the Netherlands on February 18, 2011 at 18:00 UTC. Image adapted from Sat24.com

In RACMO this stratocumulus cloud is also found, although it only lasts less than 5 hours. It was found that in RACMO the inversion layer is not well captured, which causes a too high liquid water potential temperature in the cloud layer.

A 24 h simulation is run with DALES, starting at 12:00 UTC. The initial input profiles of the liquid water potential temperature, the total specific humidity and zonal and meridional wind speed, are shown in figure 7.2.

The latent and sensible heat flux are prescribed to DALES on an hourly basis. In principle the latent and sensible heat flux are taken from the RACMO SCMin dataset, but an additional simulation is done with use of the observed fluxes. The observed and SCMin latent and sensible heat flux are shown in figure 7.3.

The large scale heat and humidity advection, the subsidence and the geostrophic zonal and meridional wind speed are prescribed with use of the RACMO SCMin data set. These large scale forcings are shown in figure 7.4.

The four additional simulations with DALES are done to gain insight in the effects changes in the input parameters. For this case the change in the initial inversion height is a decrease of 50 m, due to the uncertainty in the inversion height as observed by the radiosonde and the change in the subsidence is a decrease of 1 mm/s over the entire period and height, which a change in the order of 10 %.

In left graph of figure 7.5 the downwelling shortwave radiation at the surface is plotted as a function of time. It shows a very large difference between RACMO and the observations at the start. The DALES simulations are in a much better agreement with the observations but still up to 50 Wm^{-2} too high.
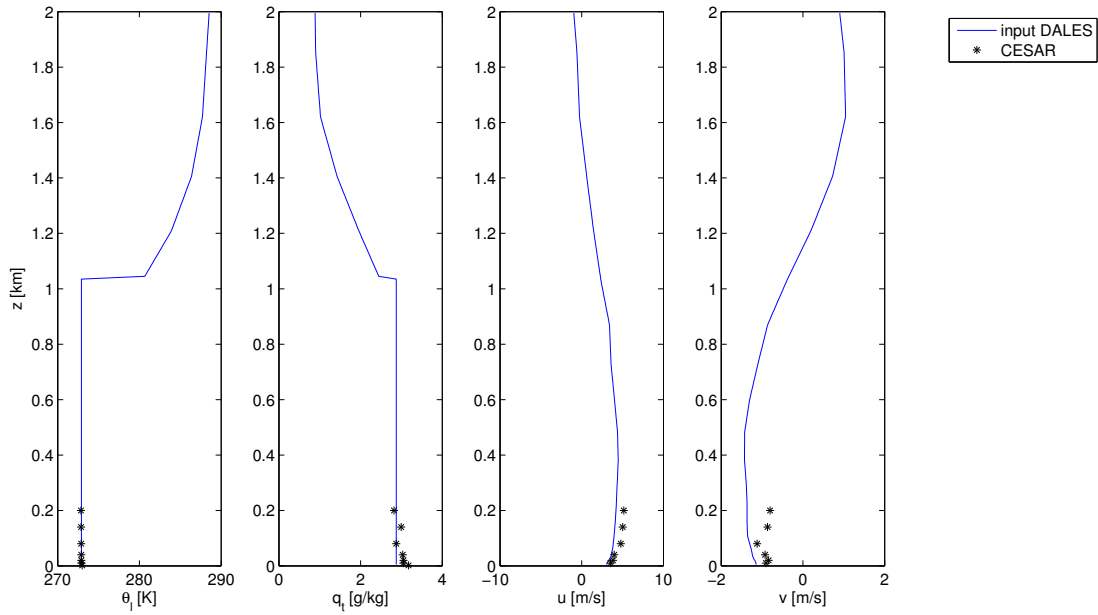
Figure 7.2: Initial DALES input profiles for Julian day 48 2011 at 12:00 UTC of the liquid water potential temperature (first graph), the total specific humidity (second graph), the zonal wind speed (third graph) and the meridional wind speed (fourth graph).

The right graph of figure 7.6 shows the net longwave radiation at the surface. It is noticed that in RACMO this net longwave radiation is mainly too high. All DALES simulations are in good agreement with the observations for the first 18 hours of the simulated period. In the last 6 hours the observed net longwave radiation is increasing fast, showing that the cloud is breaking up.
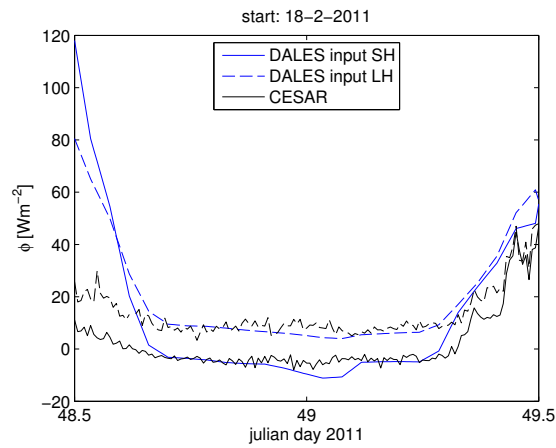
Figure 7.3: The sensible (solid line) and latent heat flux (solid line) as observed (black) and from RACMO SCMin (blue) for the entire simulation period (February 18 12.00 UTC - February 19 12.00 UTC, 2011).
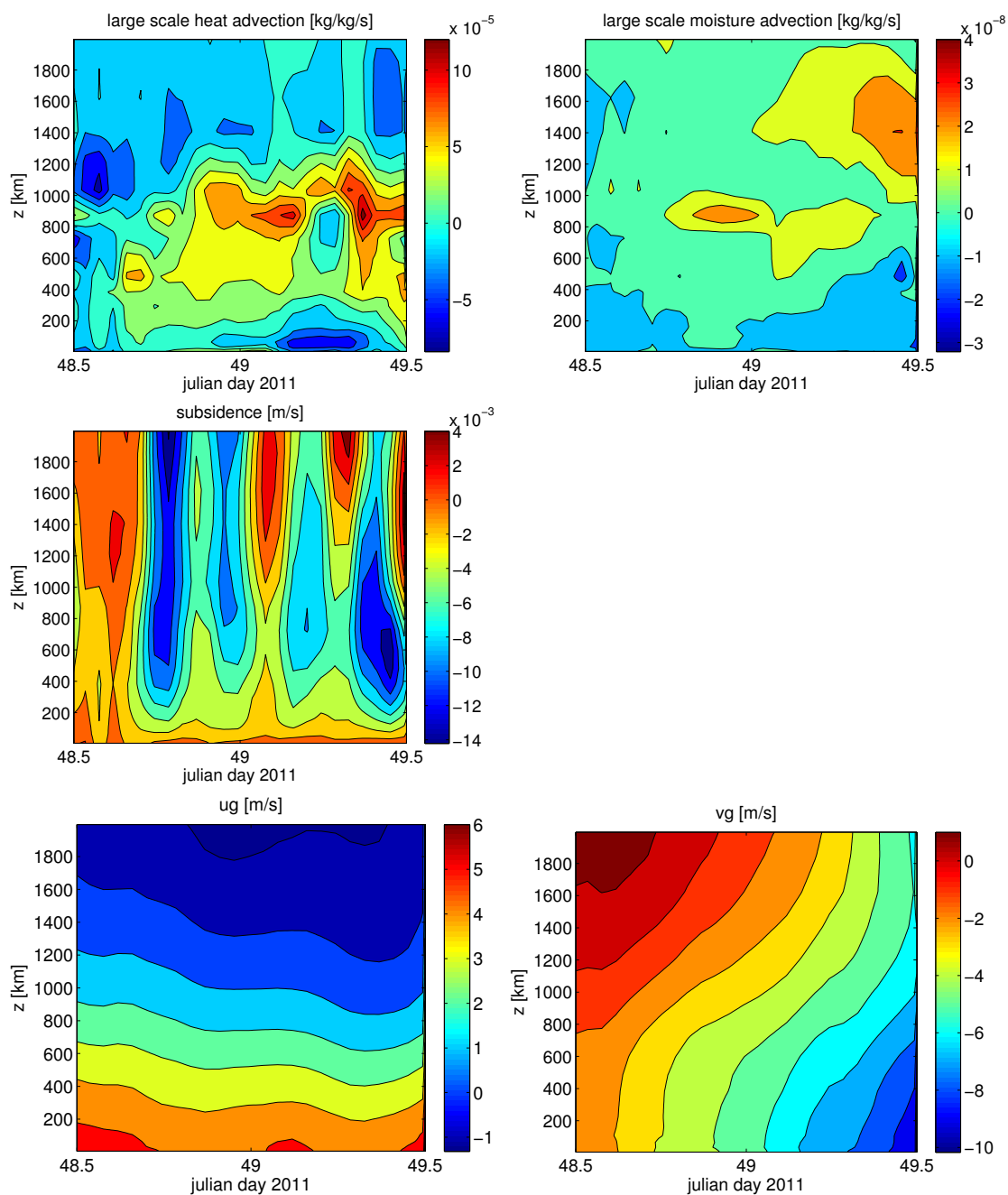
Figure 7.4: The large scale heat advection (top left), the large scale humidity advection (top right), the subsidence (middle), the geostrophic zonal wind speed (bottom left) and the geostrophic meridional wind speed (bottom right) as a function of time and height.

In the top left of figure 7.6 the inversion height and stratocumulus cloud base height are shown. With exception of the run that was forced with the observational heat
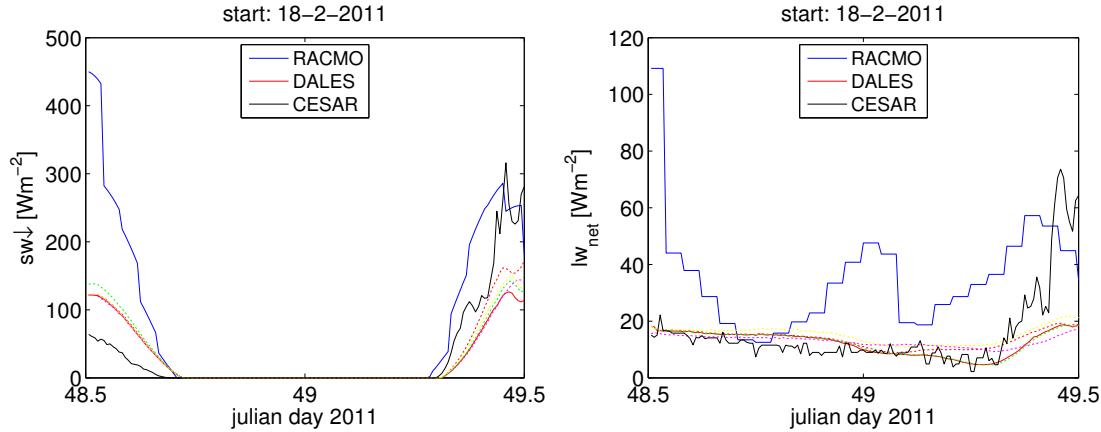
Figure 7.5: The downwelling shortwave radiation at the surface (left) and the net longwave radiation at the surface (right) as a function of time for the observations (black), RACMO (blue) and DALES. The red solid line indicates the basic DALES simulation, the dotted lines show the extra simulations with DALES for which (1) the observational heat fluxes are used (purple), (2) the radiosonde measurements are used as initial potential temperature and humidity profiles above the inversion (yellow), (3) the initial inversion height is adjusted (green) and (4) the subsidence is adjusted (red).

fluxes, a fog layer developed beneath the stratocumulus cloud between 15 and 21 hours of simulation time. The observed cloud base height shows large variations in the second half of the simulation period. These variations suggest a high degree of horizontal heterogeneity.

The top right graph of figure 7.6 shows the cloud cover as a function of time. All the simulations performed with DALES results in a constant cloud cover of one. This is in agreement with the observational data, except for the very end of the simulations where the observation shows a slight decrease in cloud cover. The cloud cover in RACMO however is decreasing much too soon and too much.

In the bottom of figure 7.6 the LWP is shown. Unfortunately the observational LWP is missing for most of the simulation period. However for the first six hours of the simulation period it can be concluded that the DALES runs are in good agreement with the observational LWP. The tendencies of the LWP in DALES are very similar for all runs. The lowest DALES LWP at the end of the simulation is caused by simulating with a further decreased subsidence. This is not surprising since according to equation 2.9 a more negative subsidence will reduce the cloud thickness. With a thinner cloud the LWP will decrease (see equation 2.2).

In figure 7.7 the potential temperature profiles at the start, middle (00.00 UTC, February 19) and end (12:00 UTC, February 19) of the simulation period is plotted. The radiosonde measurements show a decoupled mixed layer at Julian day 49 and 49.5. This decoupling is not picked up by the simulations with DALES.

The bottom of figure 7.7 shows the water vapour specific humidity. After 12 hours of simulation time the DALES q_v profiles are in good agreement with the observations. After 24 hours the simulated q_v profiles are about 0.5 g/kg dryer than the tower obser-

47
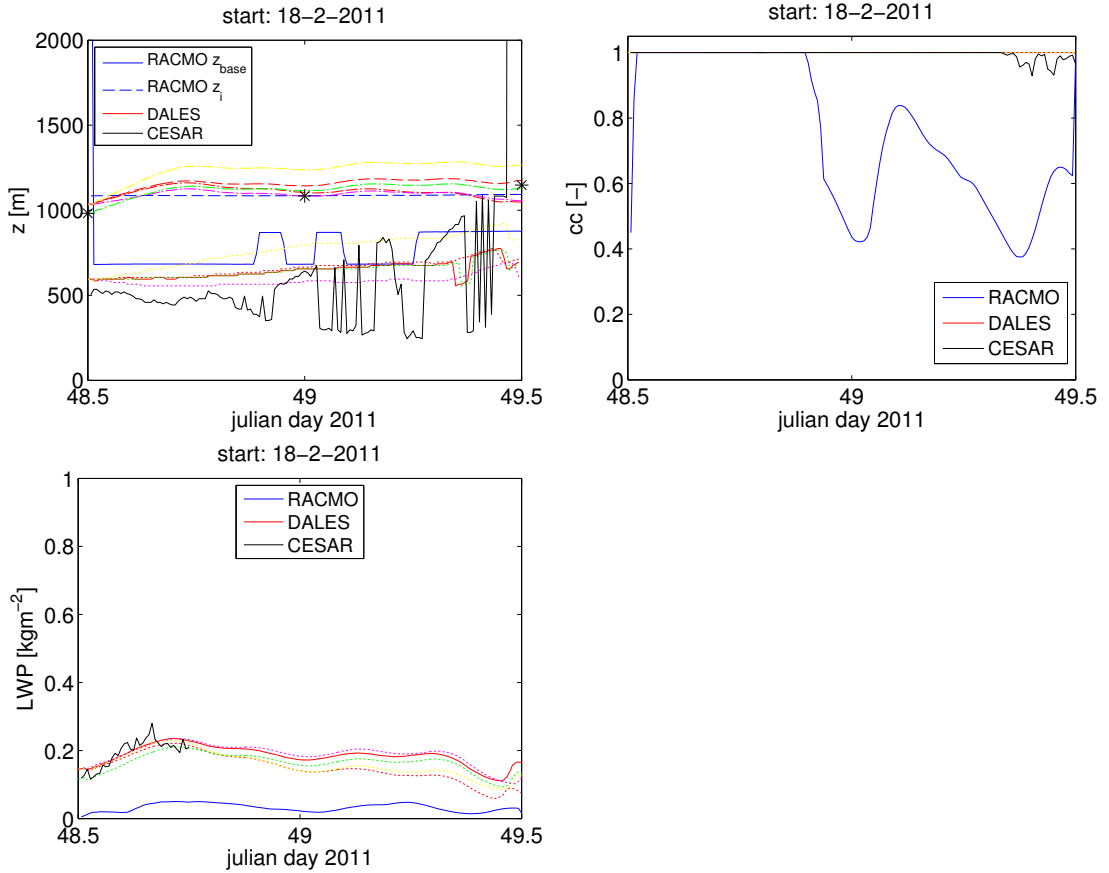
Figure 7.6: Top left: the inversion height (dashed lines/stars) and the cloud base height (solid/dotted lines) as a function of time for the observations (black), RACMO (blue) and DALES (red and dotted lines).The cloud cover (top right) and LWP (bottom) as a function of time as observed (black), as simulated by RACMO (blue) and as simulated with DALES. The red solid lines indicate the basic DALES simulations, the dotted lines show the extra simulations with DALES for which (1) the observational heat fluxes are used (purple), (2) the radiosonde measurements are used as initial potential temperature and humidity profiles above the inversion (yellow), (3) the initial inversion height is adjusted (green) and (4) the subsidence is adjusted (red).

vations, but in agreement with the radiosonde. The decoupling in the mixed layer as shown by the radiosonde does not appear in any of the DALES runs.

The liquid water potential temperature for RACMO, SCMin and DALES is shown in the top graphs of figure 7.8. The bottom graphs of figure 7.8 shows the liquid water specific humidity for RACMO, SCMin and DALES. In these graphs the relative humidity as measured by the radiosonde is also given, where a value of 1 corresponds to a relative humidity of 100 %.

If one integrates equation 2.31 over height up until just beneath the inversion layer,
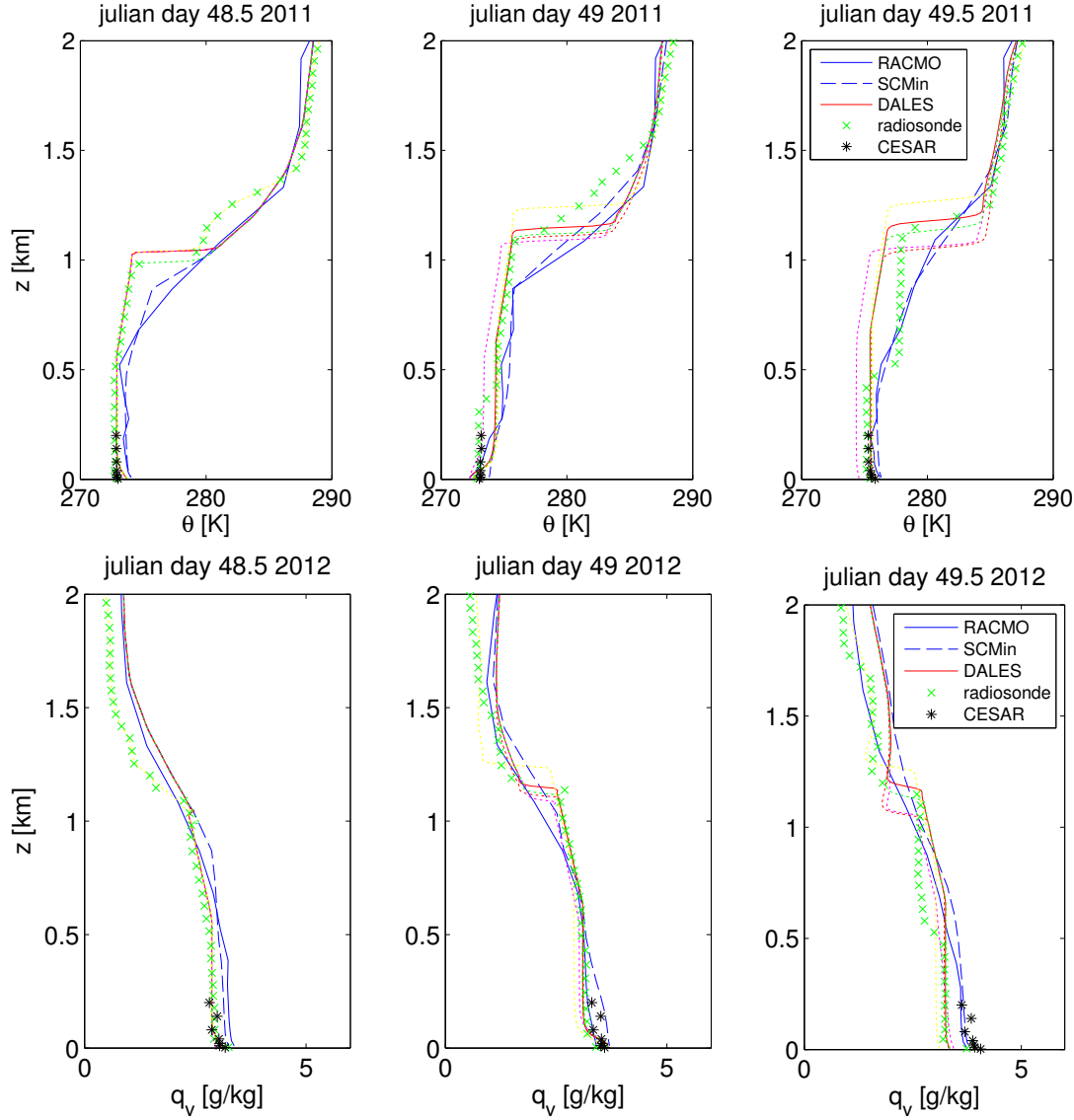
Figure 7.7: The vertical profiles of the potential temperature (top graphs) and the water vapour specific humidity (bottom graphs) as obtained from the radiosonde (green crosses), the CESAR tower (black stars), RACMO (blue line), RACMO SCMin (blue dashed line) and the DALES simulations (red and dotted lines) on February 18, 2011. The red solid lines indicate the basic DALES simulations, the dotted lines show the extra simulations with DALES for which (1) the observational heat fluxes are used (purple), (2) the radiosonde measurements are used as initial potential temperature and humidity profiles above the inversion (yellow), (3) the initial inversion height is adjusted (green) and (4) the subsidence is adjusted (red).

one obtains the following expression for the evolution of θ_l in the mixed layer:

$$\int_0^{z_i^-} \frac{\partial \overline{\theta_l}}{\partial t}\, \mathrm{d}z = -w_e \Delta \overline{\theta_l} + \overline{\theta_l' w'}^0 - \int_0^{z_i^-} \overline{u_h} \frac{\partial \overline{\theta_l}}{\partial x_h}\, \mathrm{d}z - \int_0^{z_i^-} \overline{w} \frac{\partial \overline{\theta_l}}{\partial z}\, \mathrm{d}z - \frac{1}{\overline{\rho} c_p}(\overline{F}^0 - \overline{F}^{z_i^-}), \ (7.1)$$
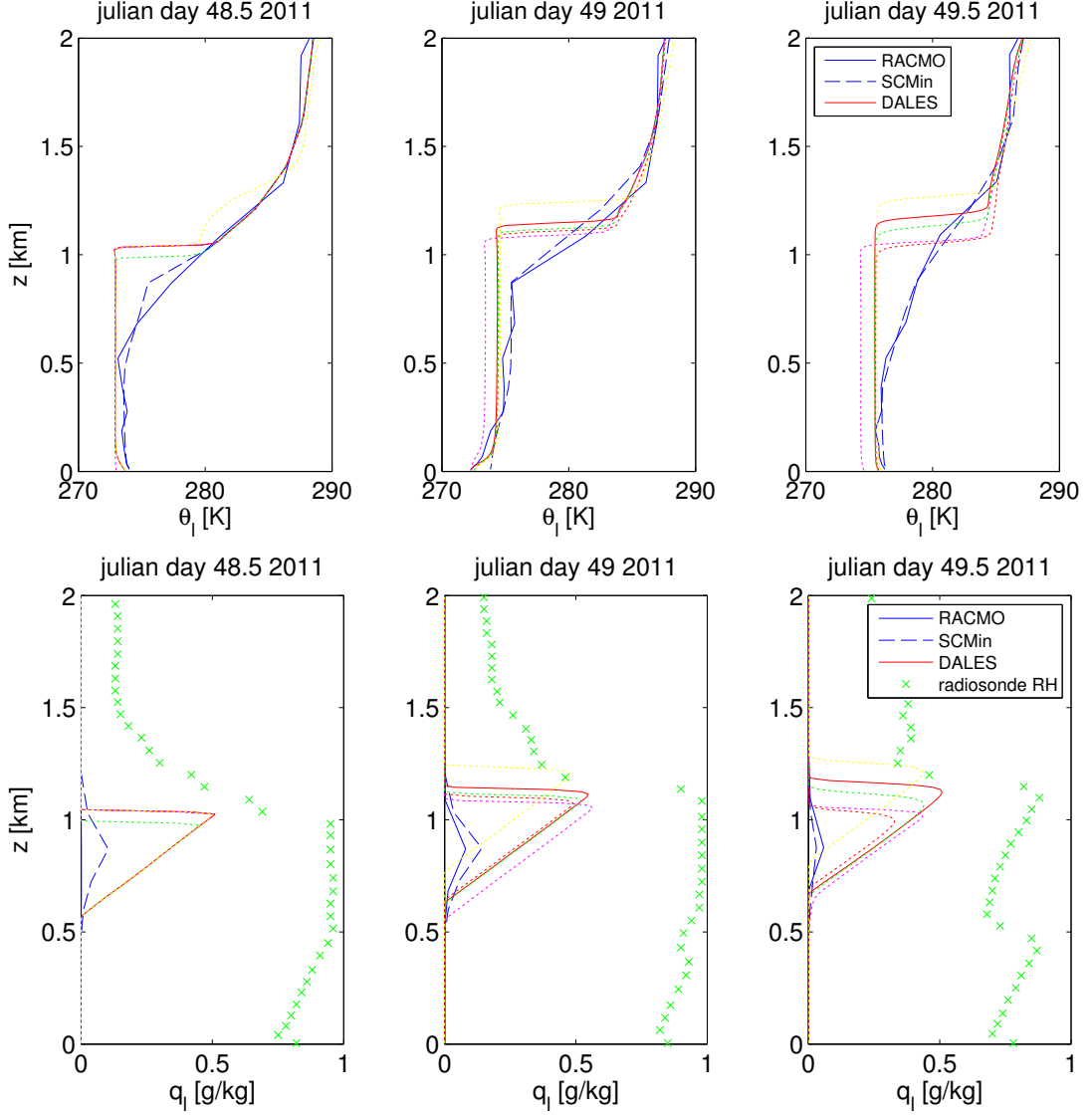
Figure 7.8: The vertical profiles of the liquid water potential temperature (top) and liquid water specific humidity (bottom) as obtained from RACMO (blue line), RACMO SCMin (blue dashed line) and from the simulations with DALES (red and dotted lines, also see caption figure 7.7) on February 18, 2011.

where the density is taken constant with height and relation 2.34 is used. The evolution of the total specific humidity beneath the inversion layer can be obtained similarly by integrating equation 2.33:

$$\int_0^{z_i^-} \frac{\partial \overline{q_t}}{\partial t}\,\mathrm{d}z = -w_e \Delta \overline{q_t} + \overline{q_t' w'}^0 - \int_0^{z_i^-} \overline{u_h} \frac{\partial \overline{q_t}}{\partial x_h}\,\mathrm{d}z - \int_0^{z_i^-} \overline{w} \frac{\partial \overline{q_t}}{\partial z}\,\mathrm{d}z \qquad (7.2)$$

The terms in the budget equations 7.1 and 7.2 from the basic DALES simulation are

shown as a function of time in figure 7.9.
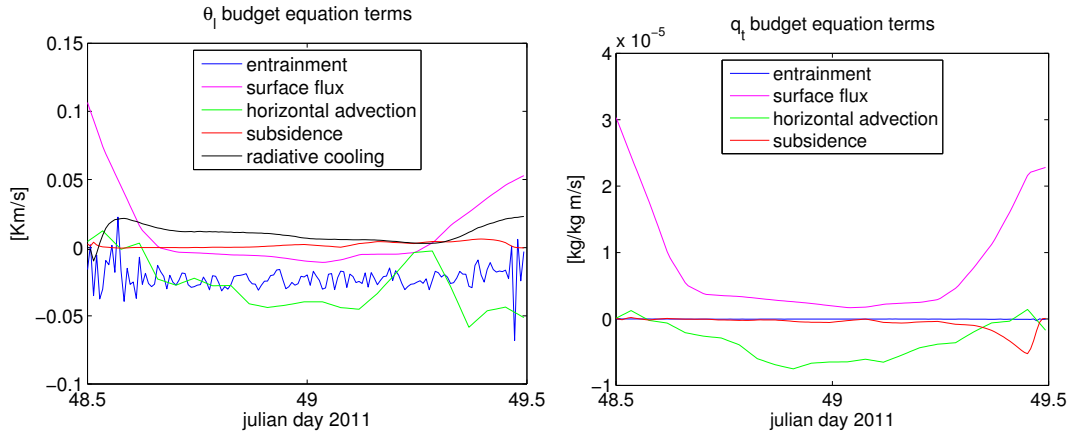
Figure 7.9: Terms from the budget equations 7.1 and 7.2 as a function of time, resulting from the basic DALES simulation.

The analysis of each term in equation 7.1 shows that at the start the most dominant term is the turbulent surface flux. This explains the lower liquid water potential temperature in the mixed layer for the run which uses the observational heat fluxes. At the start of the simulation the observational latent and sensible heat fluxes are much lower than is given by RACMO SCMin. This reduces the effect of the turbulent surface fluxes on the warming of θ_l. The left graph in figure 7.9 shows that the turbulent surface flux term is also dominating the budget of q_t at the start and end of the simulation period. The horizontal advection term is significant during the daytime hours.

Conclusions

The simulated downwelling shortwave radiation in DALES is much closer to the observations in the first half of the simulation period. Also the net longwave radiation and cloud cover is well predicted. The LWP shows little variation for the different DALES runs. The vertical profiles of the observed potential temperature and water vapour specific humidity show decoupling of the mixed layer. Unfortunately none of the simulations captured this decoupling. However the radiosonde measurement of the water vapour specific humidity at the end of the simulation period also shows a significant difference with the tower measurements, which could mean that at this moment the atmosphere is not horizontally homogeneous. The observed variations in the cloud base height also suggest this.

7.3 Simulation 6 November 2011

Another simulation is done running from 12:00 UTC on the 6th of November 2011 up until 12.00 UTC the next day. In this period two stratocumulus cases were identified in the observations. The first stratocumulus period starts at midnight and lasts 5 hours. This stratocumulus case was not found in RACMO. In figure 7.10 an infrared satellite image is shown at the beginning of the second stratocumulus period of 4 hours starting at 22.45 UTC. This stratocumulus case was also simulated in RACMO.
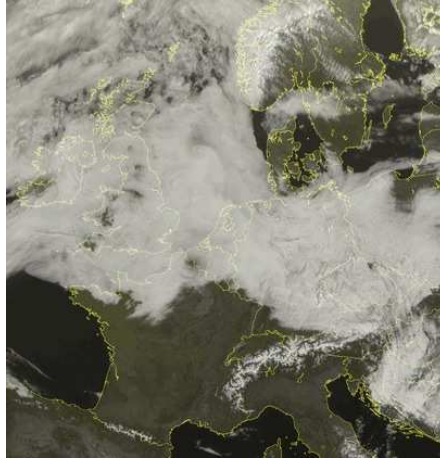
Figure 7.10: Infrared satellite image of stratocumulus cloud deck above the Netherlands on November 6, 2011 at 22:45 UTC. Image adapted from Sat24.com

The latent and sensible heat fluxes from the RACMO SCMin dataset and from CESAR are shown in figure 7.11 for the entire simulation period.
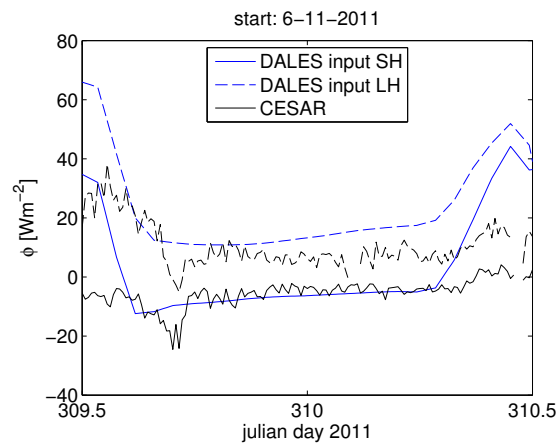
Figure 7.11: The sensible (solid line) and latent heat flux (solid line) as observed (black) and from RACMO SCMin (blue) for the entire simulation period (November 6 12.00 UTC - November 7 12.00 UTC, 2011).

The initial input profiles of the liquid water potential temperature, the total specific humidity and zonal and meridional wind speed for the DALES simulations, are shown in figure 7.12.
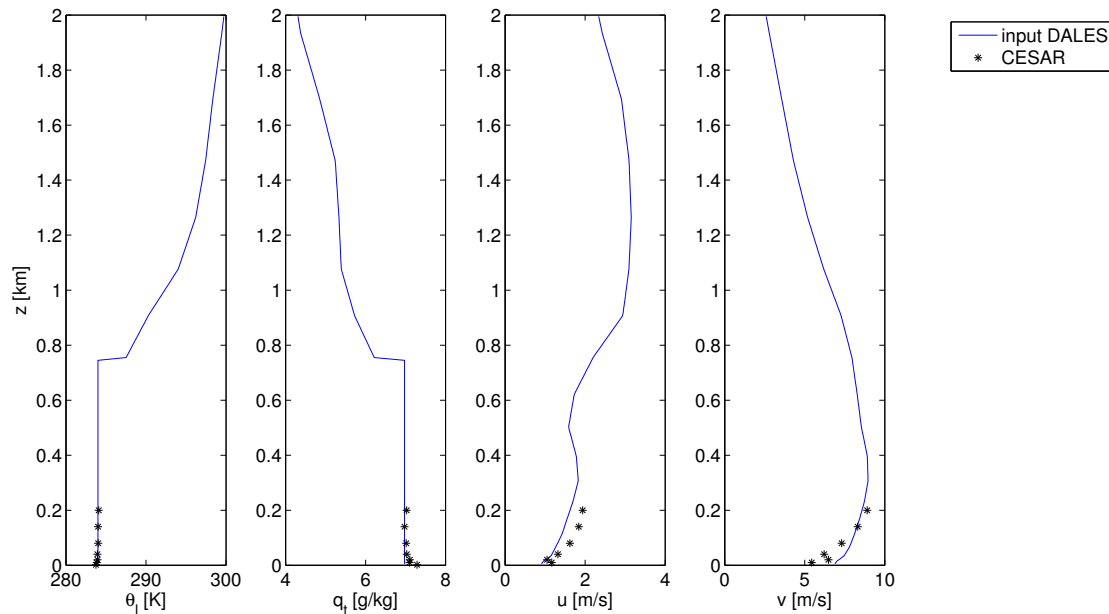
Figure 7.12: Initial DALES input profiles for Julian day 309 2011 at 12:00 UTC of the liquid water potential temperature (first graph), the total specific humidity (second graph), the zonal wind speed (third graph) and the meridional wind speed (fourth graph).

The large scale heat and humidity advection, the subsidence and the geostrophic zonal and meridional wind speed as prescribed with use of the RACMO SCMin data set are shown in figure 7.13 and 7.14
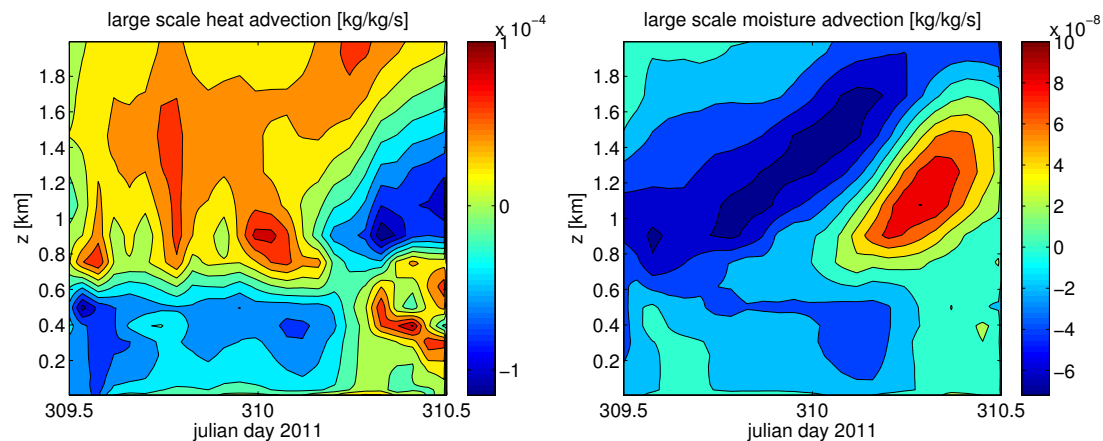
Figure 7.13: The large scale heat advection (left) and the large scale humidity advection (right) as a function of time and height.
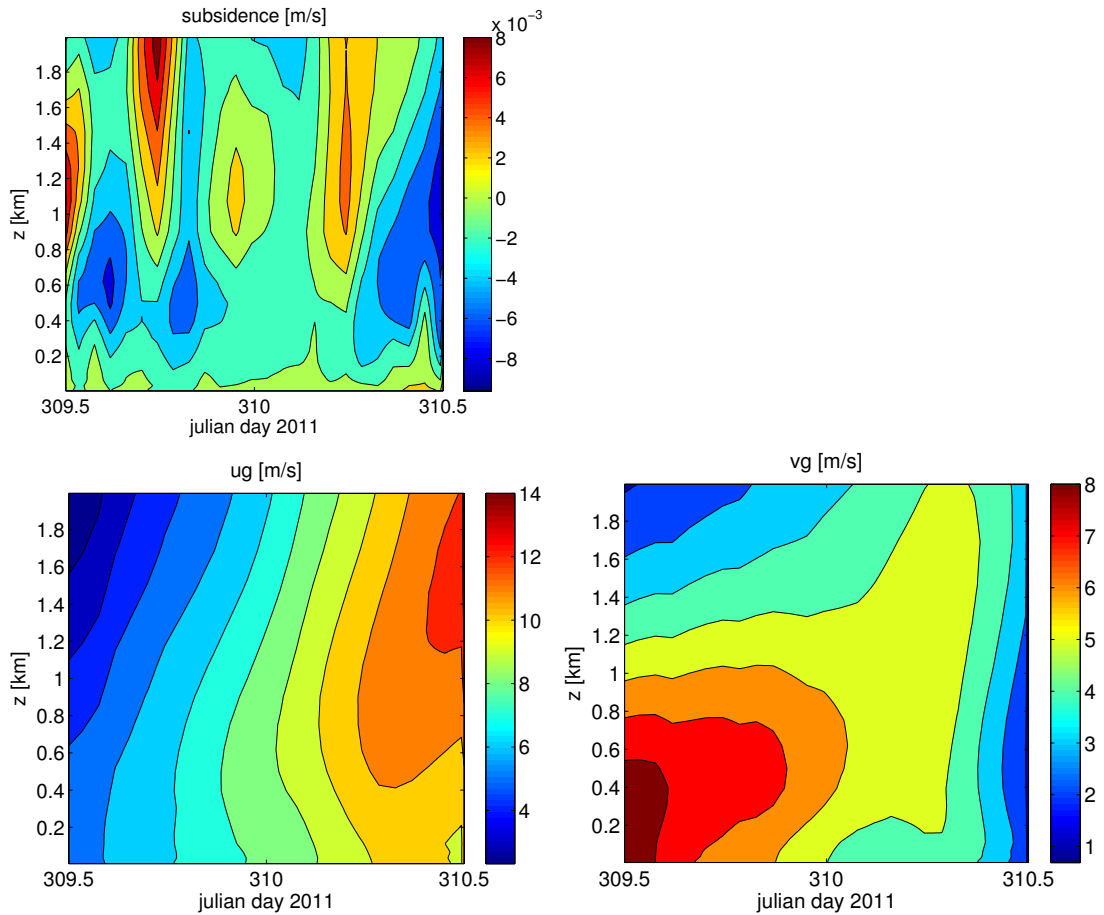
Figure 7.14: The subsidence (top), the geostrophic zonal wind speed (bottom left) and the geostrophic meridional wind speed (bottom right) as a function of time and height.

Next to the basic DALES simulation, the additional four runs with adjustments of the input parameters have been done. For this case the adjustment of the inversion height is an increase with 50 m, due to the uncertainty in the inversion height as observed by the radiosonde and the adjustment of the subsidence is a reduction of 1 mm/s over the entire simulation period and height.

Figure 7.15 shows the downwelling shortwave radiation at the surface as a function of time in the left graph. In the first half of the simulation the DALES simulations show a too high shortwave radiation, however in the first 3 hours DALES is closer to the observations than RACMO. The run with an increased initial inversion height is closest to the observed downwelling shortwave radiation.

The right graph of figure 7.15 shows the net longwave radiation as a function of time. There are very little differences in the DALES simulations. They all follow the observations very well, except the peak in the first half of the period is missing.
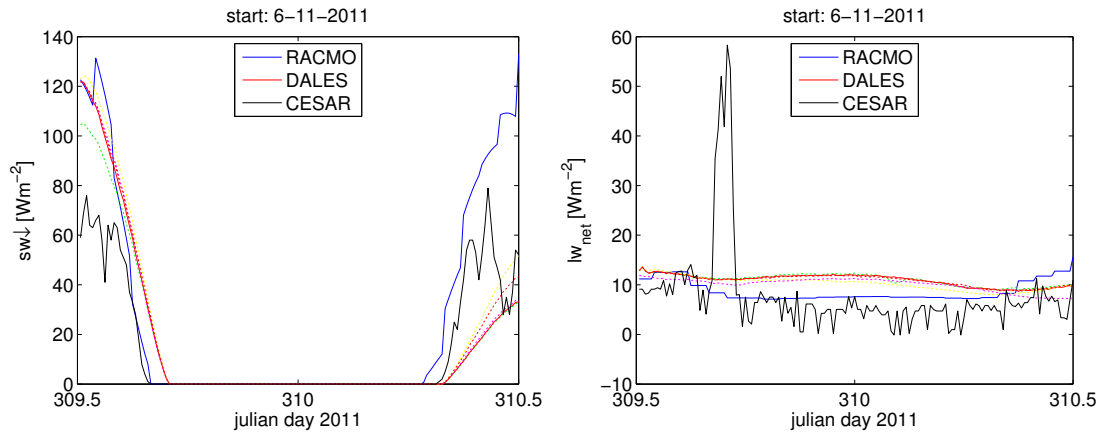
Figure 7.15: The downwelling shortwave (left) and net longwave (right) radiation as a function of time as observed (black), in RACMO (blue) and in DALES. The red solid lines indicate the basic DALES simulations, the dotted lines show the extra simulations with DALES for which (1) the observational heat fluxes are used (purple), (2) the radiosonde measurements are used as initial potential temperature and humidity profiles above the inversion (yellow), (3) the initial inversion height is adjusted (green) and (4) the subsidence is adjusted (red).

Figure 7.16 shows the cloud base height and inversion height as a function of time in the left graph. The spread in cloud base height for the DALES simulations is very small and they follow the same trends. All DALES inversion heights increase with time, as likewise is shown by the observational data, but not by RACMO.
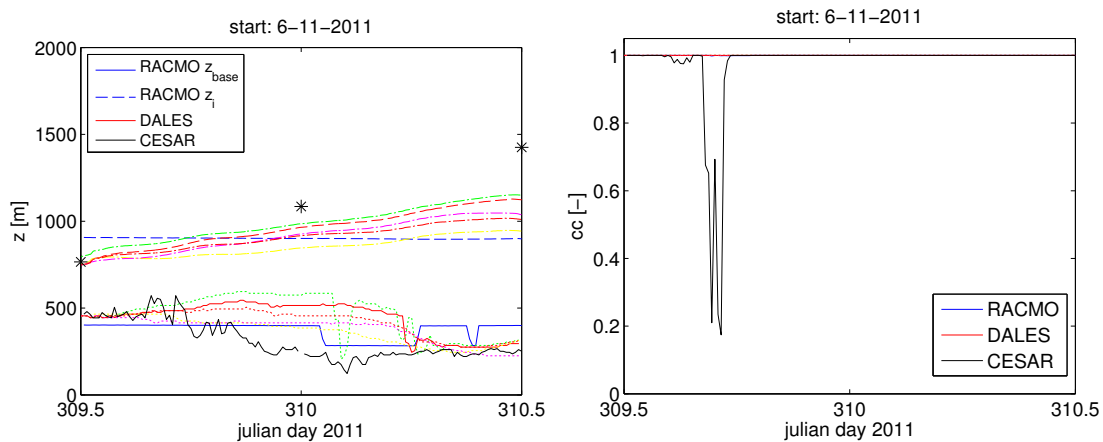
Figure 7.16: The inversion (dashed/stars) and cloud base (solid/dotted) heights (top left) and cloud cover (top right) as a function of time as observed (black), as simulated by RACMO (blue) and as simulated with DALES (see caption figure 7.15 for colour specifications).

The right graph in figure 7.16 shows the cloud cover as a function of time. All DALES simulations result in a constant cloud cover of 1. At the same moment of the peak in the observed net longwave radiation, the observed cloud cover shows a decrease. This gap in the cloud deck is not captured by the simulations.

Figure 7.17 contains the LWP as a function of time. In the first 12 hours the observed LWP is in agreement with the DALES simulations, except for the short gap in the cloud deck where the observed LWP goes to zero. After 24 hours however, the simulated LWP is up to a factor 2 too high.
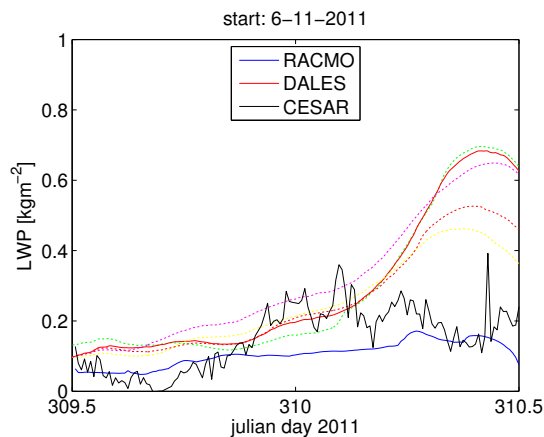
Figure 7.17: The LWP as a function of time as observed (black), as simulated by RACMO (blue) and as simulated with DALES (see caption figure 7.15 for colour specifications).

In figure 7.18 the vertical profiles of the potential temperature is shown for the 3 moments in the simulation period for which the radiosonde measurements are available. The water vapour specific humidity profiles are shown in the bottom part of figure 7.18. The radiosonde measurements of the water vapour specific humidity at Julian day 309.5 and 310 show large variations just above the inversion height. This gives rise to the notion that the free troposphere might not horizontal homogeneous and that the profile might not be representative for a large area. This complicates the method of data assimilation.

Equation 7.1 and 7.2 are used to analyse the contributions to the evolution of θ_l and q_t in the mixed layer. Each term of both equations is plotted as a function of time as shown in figure 7.19.

The budget analyses reveals that the cooling is dominated by the horizontal advection term. At the end of the simulation the turbulent surface flux is important, which explains that using the observational latent and sensible heat fluxes result in the coldest and driest profiles after 24 hours. The observational latent and sensible heat fluxes are much lower than found in SCMin at the end of the simulation.
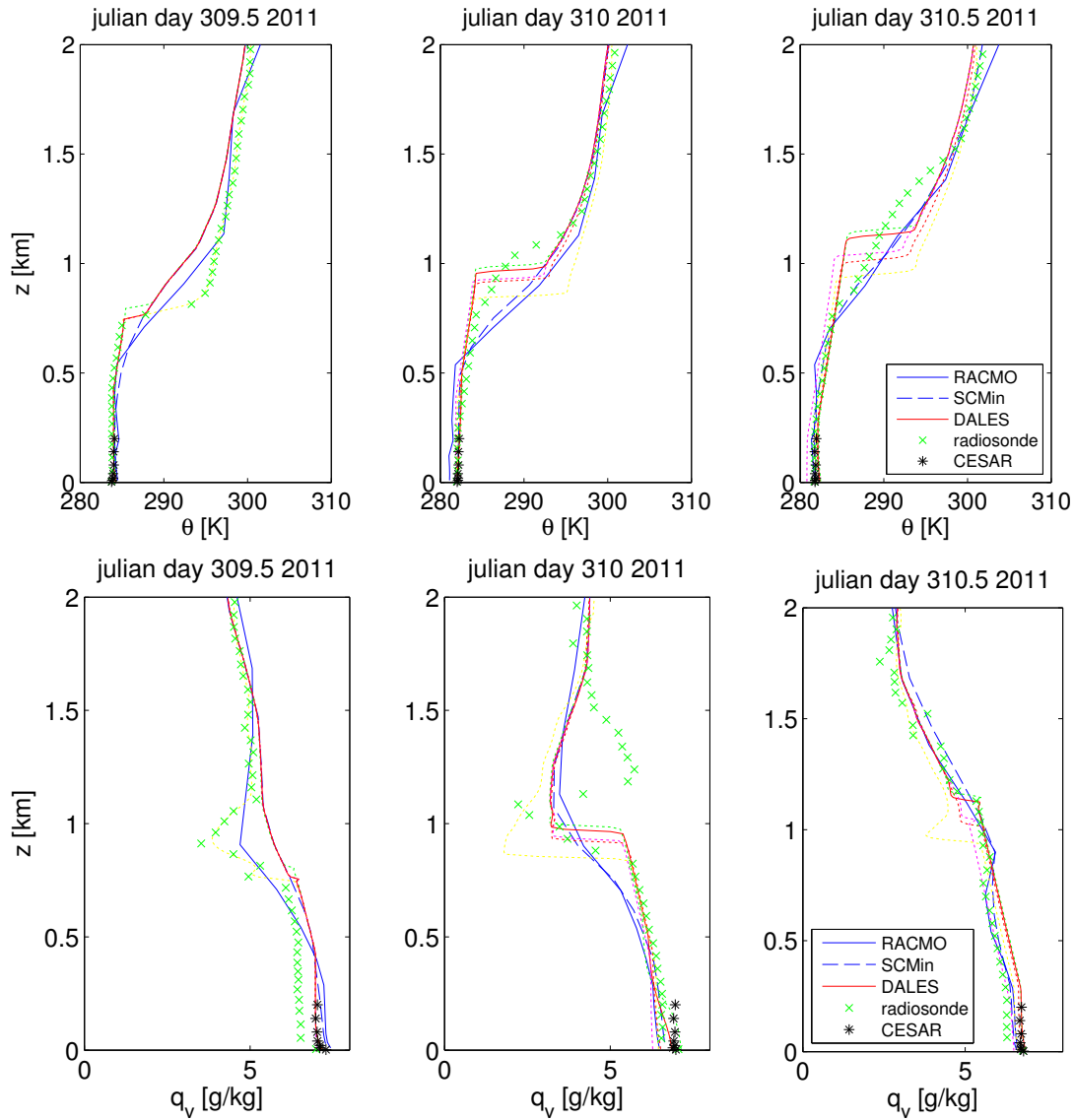
Figure 7.18: The vertical profiles of the potential temperature (top graphs) and the water vapour specific humidity (bottom graphs) as obtained from the radiosonde (green crosses), the CESAR tower (black stars), the RACMO set (blue line), the RACMO SCMin set (blue dashed line) and the DALES simulations. The red solid lines indicate the basic DALES simulations, the dotted lines show the extra simulations with DALES for which (1) the observational heat fluxes are used (purple), (2) the radiosonde measurements are used as initial potential temperature and humidity profiles above the inversion (yellow), (3) the initial inversion height is adjusted (green) and (4) the subsidence is adjusted (red).

Conclusions

In the first 3 hours the downwelling shortwave radiation of DALES is closer to the observations than RACMO. After 5 to 6 hours a gap in the cloud deck is shown in the
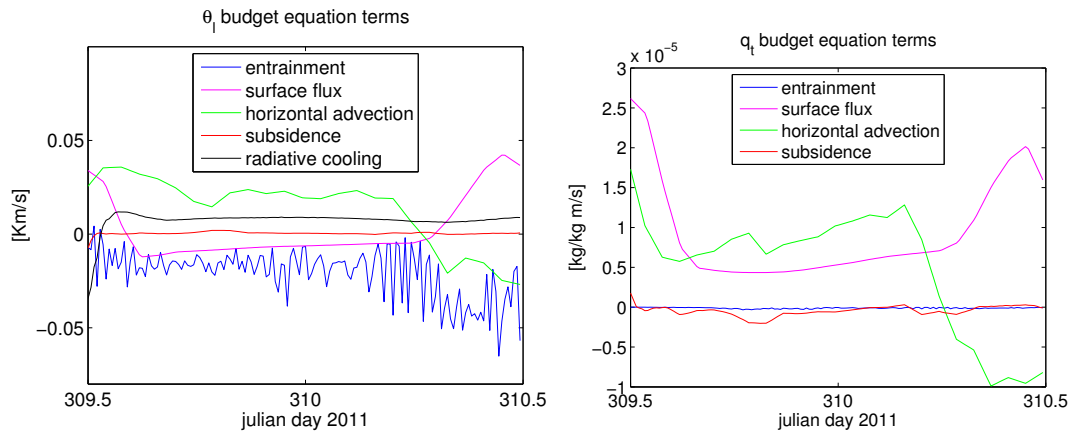
Figure 7.19: Terms from the budget equations 7.1 and 7.2 as a function of time, resulting from the basic DALES simulation.

observations, which is not captured by the simulations. At the end of the simulated period the LWP is too high. The simulated potential temperature and water vapour specific humidity profiles are in very good agreement with the radiosonde and Cabauw measurements.

7.4 Simulation 10 November 2011

The third simulation period covers a stratocumulus case that is observed on the 10th of November 2011, starting at 11:10 and lasting almost 6 hours. A satellite image of the cloud deck at 14:00 UTC is shown in 7.20. The stratocumulus case is not found in RACMO, instead RACMO simulates a clear sky.

Figure 7.20: Satellite image of stratocumulus cloud deck above the Netherlands on November 10, 2011 at 14:00 UTC. Image adapted from Sat24.com

The simulations done with DALES start at 12:00 UTC November 10th, 2011 and end at 12:00 UTC the next day. The initial input profiles of the liquid water potential temperature, the total specific humidity and zonal and meridional wind speed, are shown in figure 7.21.
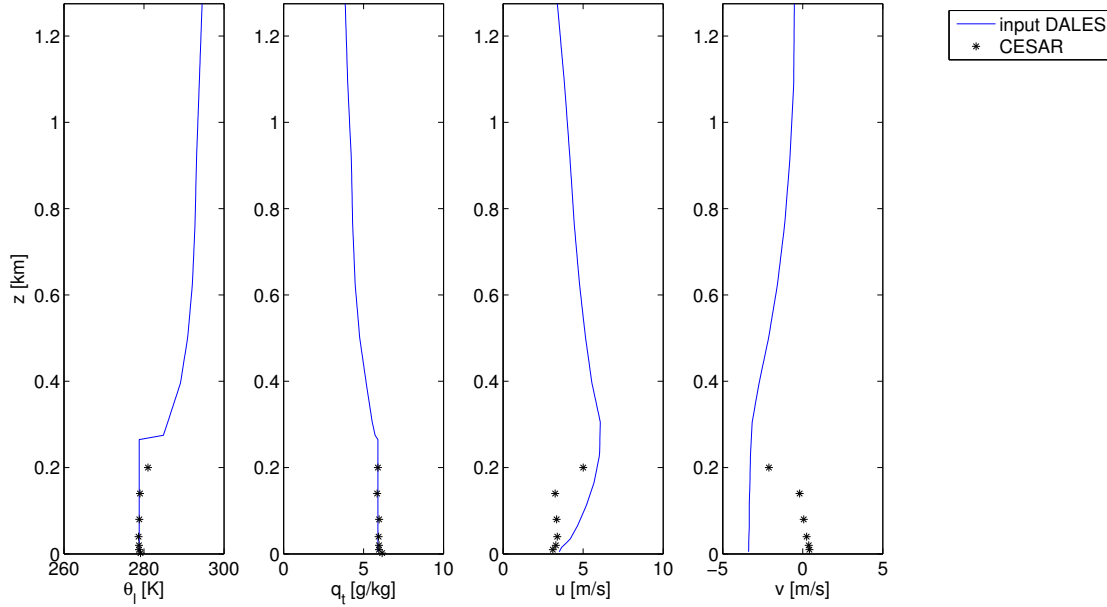
Figure 7.21: Initial DALES input profiles for Julian day 313 2011 at 12:00 UTC of the liquid water potential temperature (first graph), the total specific humidity (second graph), the zonal wind speed (third graph) and the meridional wind speed (fourth graph).

The large scale heat and humidity advection, the subsidence and the geostrophic zonal and meridional wind speed are prescribed with use of the RACMO SCMin data set. These large scale forcings are shown in figure 7.22.

The latent and sensible heat flux as prescribed to DALES from the RACMO SCMin dataset and from CESAR are shown in figure 7.23. The heat fluxes in SCMin are much higher at the start and end of the simulation period than is measured at CESAR. Likely because the lack of clouds in RACMO SCMin results in a too high solar radiative flux at the surface.

The downwelling shortwave radiation at the surface is shown in the left graph of figure 7.24. All the DALES simulations result in a downwelling shortwave radiation that is much closer to the observed radiation than RACMO.

The time series of the net longwave radiation at the surface is shown in the right of figure 7.24. The DALES runs are in good agreement with the observational data, while RACMO shows net longwave radiation that is much too high.
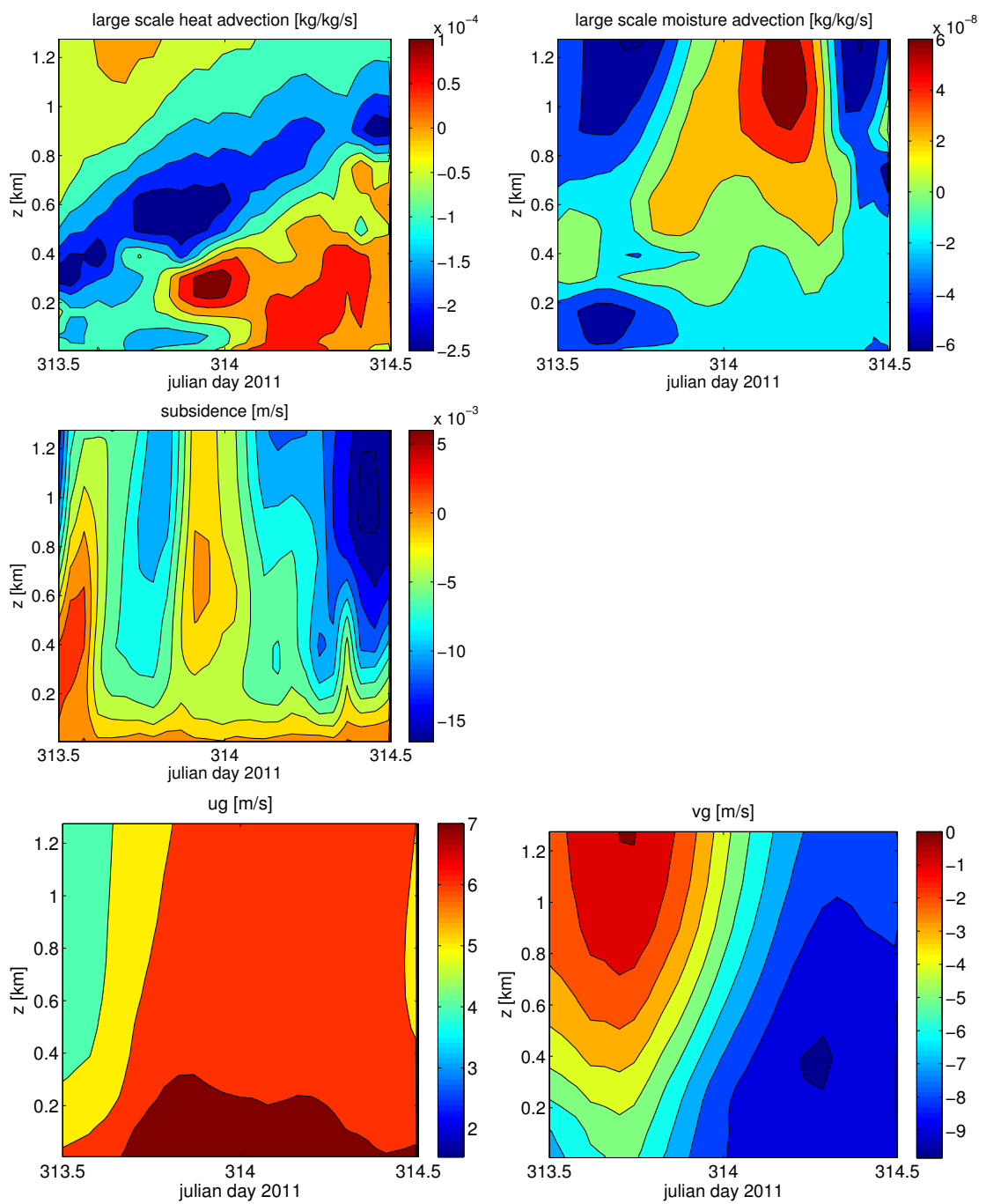
Figure 7.22: The large scale heat advection (top left), the large scale humidity advection (top right), the subsidence (middle), the geostrophic zonal wind speed (bottom left) and the geostrophic meridional wind speed (bottom right) as a function of time and height.

The cloud base height and inversion height as a function of time are shown in figure
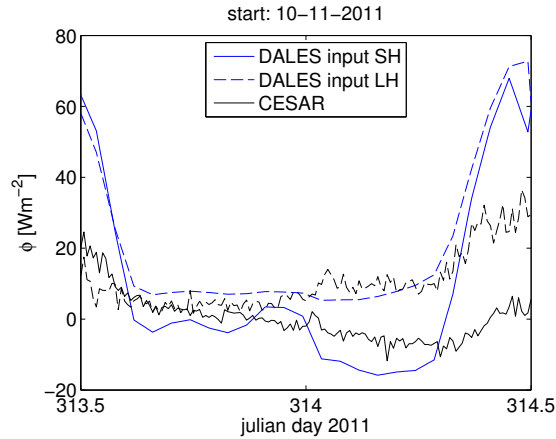
Figure 7.23: The sensible (solid line) and latent heat flux (solid line) as observed (black) and from RACMO SCMin (blue) for the entire simulation period (November 10 12.00 UTC - November 11 12.00 UTC, 2011).

??. The cloud base heights as simulated by DALES are not showing what is observed. After about 3 hours the cloud base heights have dropped to the surface, at which they stay for the rest of the period. The inversion height is also lower than is observed.

The time series of the cloud cover are shown in the right of figure **??**. The DALES simulations result in a cloud cover of 1 throughout the simulation, which is also observed. RACMO shows a cloud cover close to zero.

The times series of the LWP are shown in the bottom graph of figure **??**. During
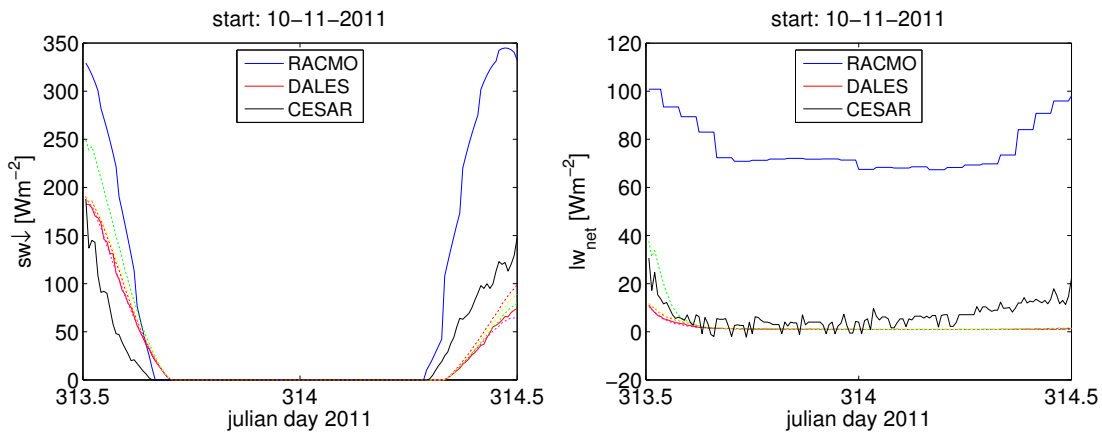
Figure 7.24: The downwelling shortwave radiation at the surface (left) and the net longwave radiation at the surface (right) as a function of time for the observations (black), RACMO (blue) and DALES. The red solid lines indicate the basic DALES simulations, the dotted lines show the extra simulations with DALES for which (1) the observational heat fluxes are used (purple), (2) the radiosonde measurements are used as initial potential temperature and humidity profiles above the inversion (yellow), (3) the initial inversion height is adjusted (green) and (4) the subsidence is adjusted (red).
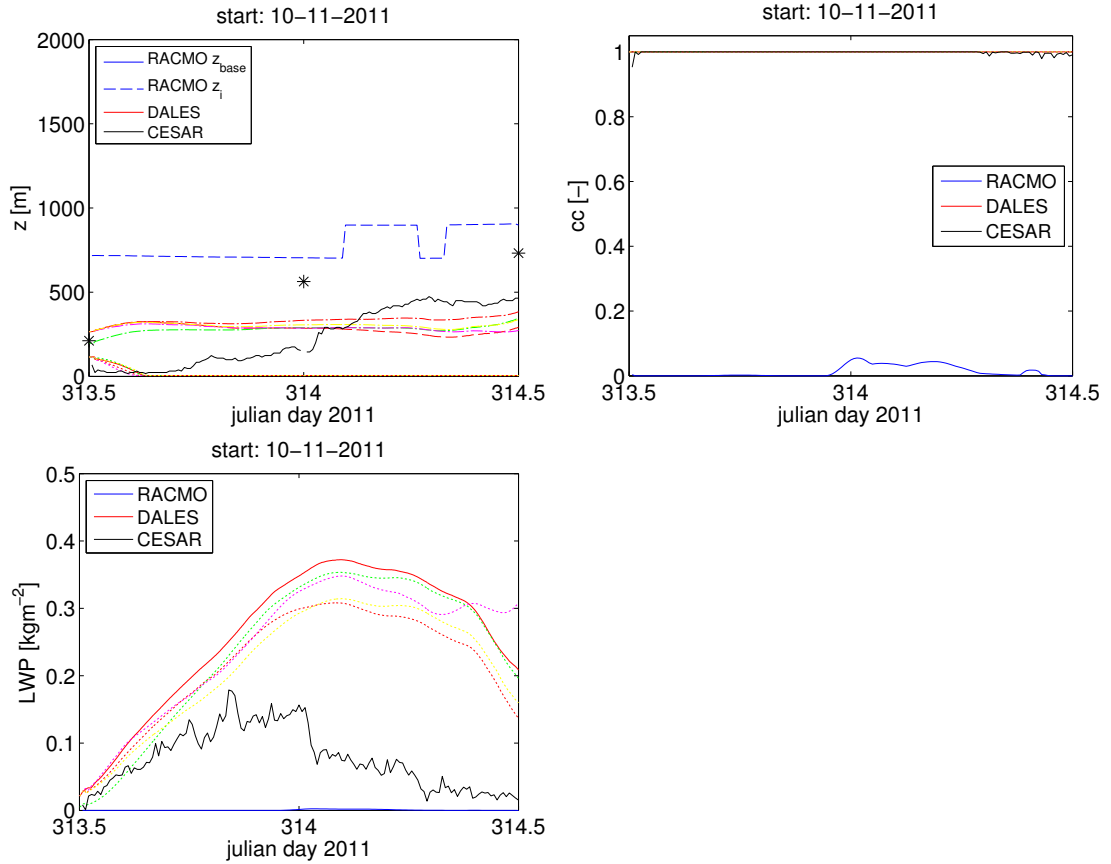
Figure 7.25: Top left: the inversion (dashed/stars) and the cloud base (solid/dotted) heights (top left) and the LWP (bottom) as a function of time for the observations (black), RACMO (blue) and DALES (see caption of figure 7.24 for the colour specifications).

the first 6 hours the with DALES simulated LWPs are in good agreement with the observations. In the second half of the simulation period the DALES LWPs are too high.

With use of equations 7.1 and 7.2 the terms contributing to the evolution of θ_l and q_t in the mixed layer are calculated. The result is shown in figure 7.26. It shows that large scale horizontal advection causes a significant heating and moistering of the profiles. The surface flux plays an important role at the start and end of the simulation period.

Conclusions

The cloud layer as simulated with DALES is situated too low. The simulated downwelling shortwave radiation and the net longwave radiation however are still quite close to the observed values. RACMO however simulated a far too high downwelling shortwave and net longwave radiation, because a clear sky is simulated in RACMO. The LWPs as simulated with DALES are close to the observed values for the first 6 hours of the
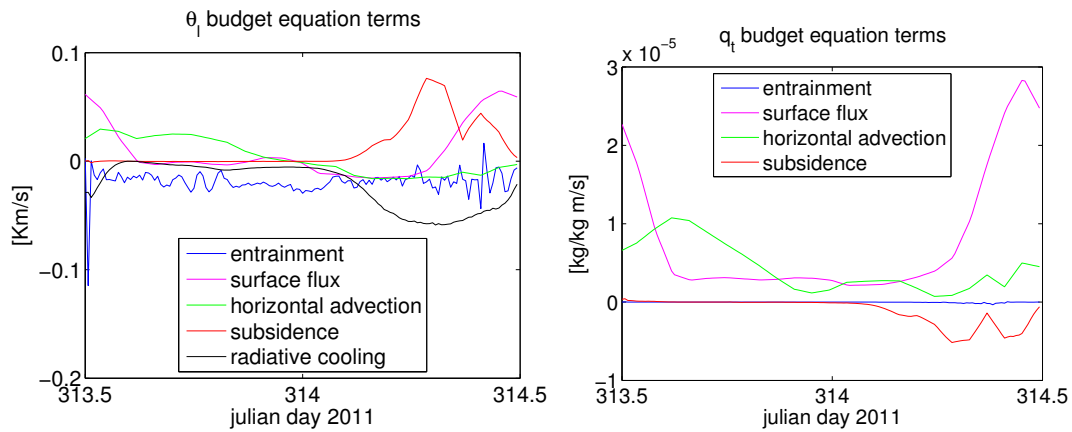
Figure 7.26: Terms from the budget equations 7.1 and 7.2 as a function of time, resulting from the basic DALES simulation.

simulation. Furthermore the tendency of the LWP in DALES is the similar for all runs.

7.5 Simulation 13 March 2012

In figure 7.27 a satellite image is shown of a stratocumulus cloud deck on March 13, 2012, at 11:00 UTC. The observed stratocumulus case starts at 9:40 UTC and lasts almost 12 hours. This stratocumulus case is also identified in both RACMO and GALES.
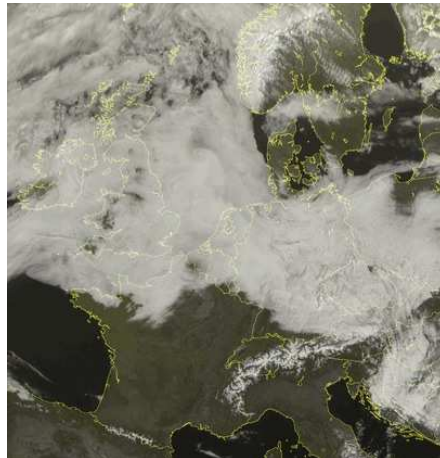
Figure 7.27: Satellite image of stratocumulus cloud deck above the Netherlands on March 13, 2012 at 11:00 UTC. Image adapted from Sat24.com

A 24 h simulation is run with DALES, starting at 12:00 UTC on March 13. The initial input profiles of the liquid water potential temperature, the total specific humidity and zonal and meridional wind speed, are shown in figure 7.28.
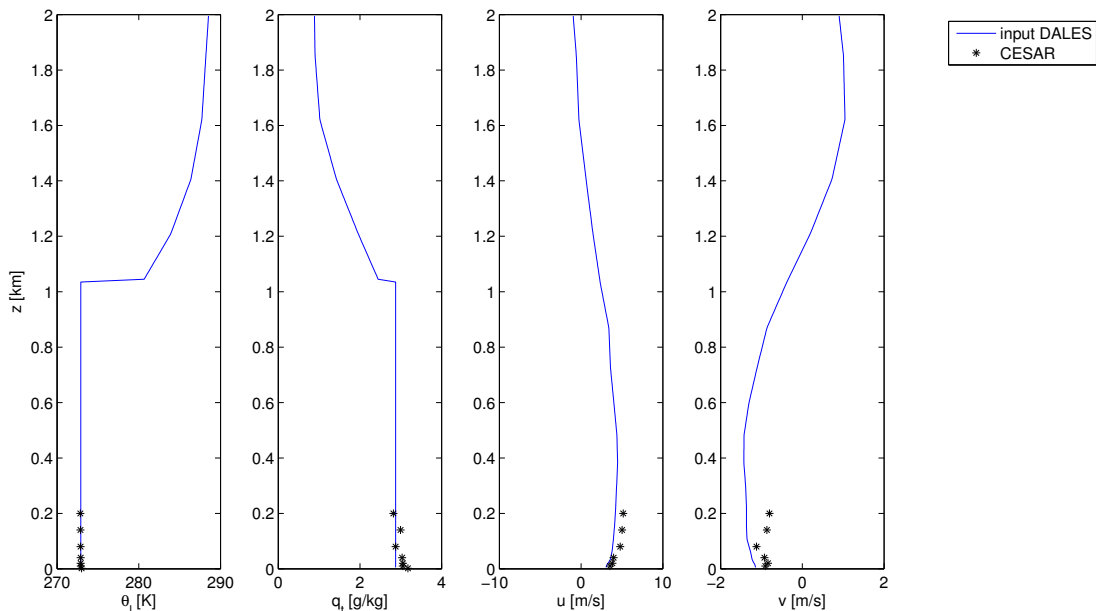
Figure 7.28: Initial DALES input profiles for Julian day 72 2012 at 12:00 UTC of the liquid water potential temperature (first graph), the total specific humidity (second graph), the zonal wind speed (third graph) and the meridional wind speed (fourth graph).

The large scale heat and humidity advection, the subsidence and the geostrophic zonal and meridional wind speed are prescribed with use of the RACMO SCMin data set. These large scale forcings are shown in figure 7.29.

The latent and sensible heat flux from CESAR and RACMO SCMin are shown in figure 7.30.

In figure 7.31 the downwelling shortwave radiation at the surface is shown in the graph on the left. It shows that the radiation is overestimated by RACMO and the DALES simulations, however DALES is closer to the observations over the entire simulation period.

In the right graph of figure 7.31 the net longwave radiation at the surface is shown. Most DALES simulations are following the observations rather well.
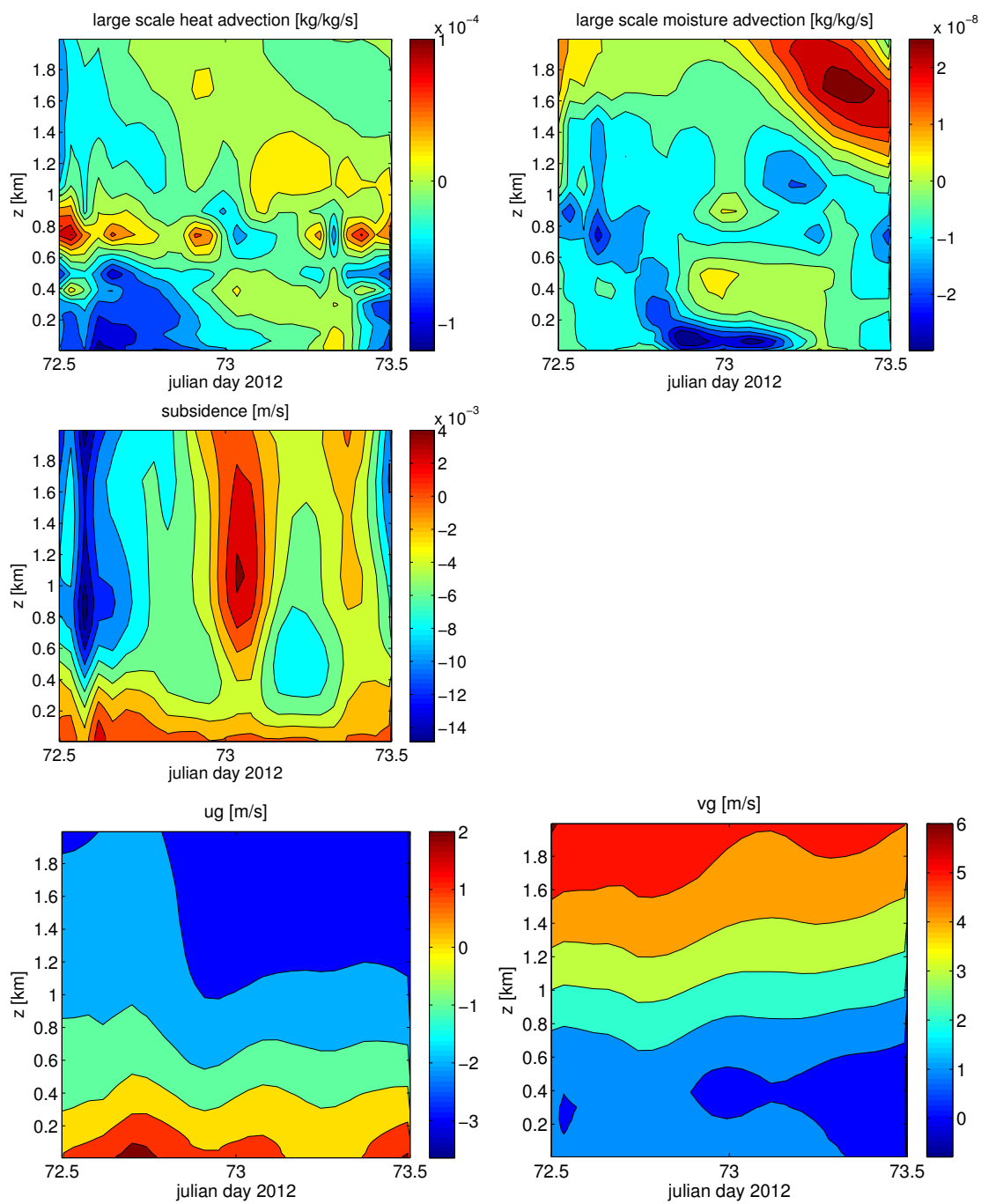
Figure 7.29: The large scale heat advection (top left), the large scale humidity advection (top right), the subsidence (middle), the geostrophic zonal wind speed (bottom left) and the geostrophic meridional wind speed (bottom right) as a function of time and height.

The evolution of the cloud base and inversion height is shown in the top left graph
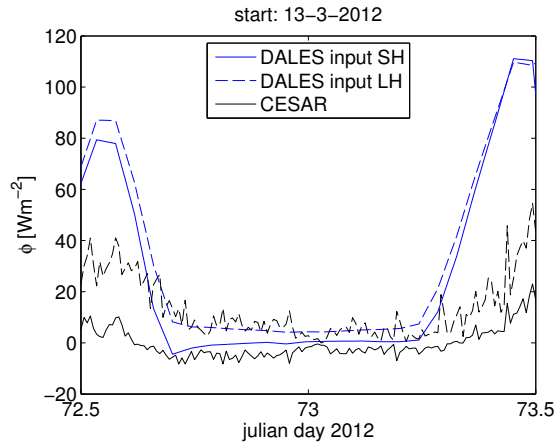
Figure 7.30: The sensible (solid line) and latent heat flux (solid line) as observed (black) and from RACMO SCMin (blue) for the entire simulation period (March 13 12.00 UTC - March 14 12.00 UTC, 2011).

of figure 7.32. It is shown that the cloud layer in GALES is a bit too low and thin. The DALES simulation with the observed heat fluxes is very close to the observations.

The cloud cover as a function of time is shown in the top right graph of figure 7.32. All runs with DALES give a cloud cover very close to 1 for the entire simulation period. The observational data show that the cloud cover reduces drastically just before the end of the simulation period.
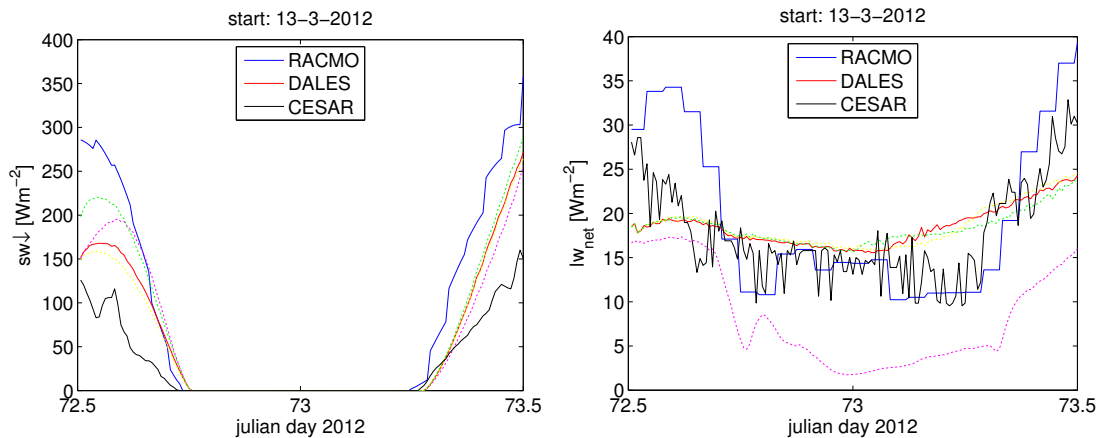
Figure 7.31: The downwelling shortwave radiation at the surface (left) and the net longwave radiation at the surface (right) as a function of time for the observations (black), RACMO (blue) and DALES. The red solid lines indicate the basic DALES simulations, the dotted lines show the extra simulations with DALES for which (1) the observational heat fluxes are used (purple), (2) the radiosonde measurements are used as initial potential temperature and humidity profiles above the inversion (yellow), (3) the initial inversion height is adjusted (green) and (4) the subsidence is adjusted (red).
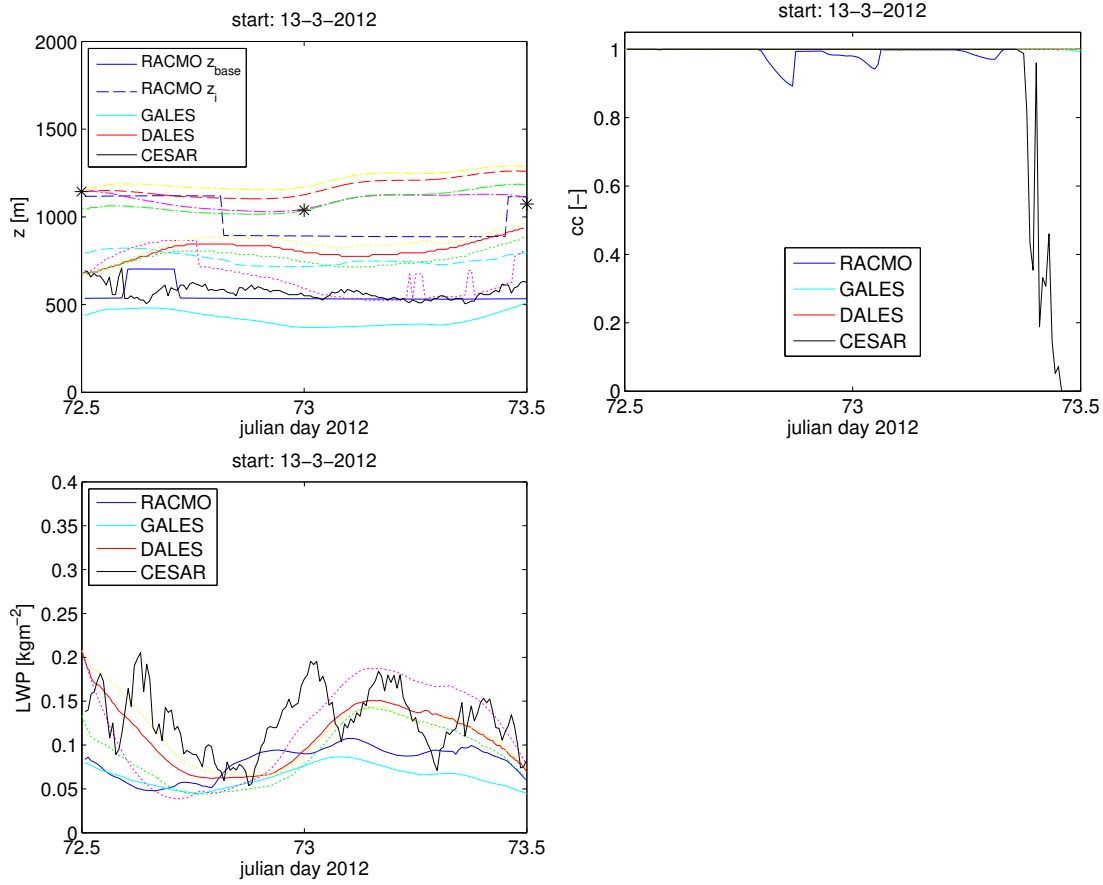
Figure 7.32: The inversion (dashed/stars) and the cloud base (solid/dotted) heights (top left), cloud cover (top right) and LWP (bottom) as a function of time for the observations (black), RACMO (blue), GALES (aqua) and DALES (see caption of figure 7.31 for colour specification).

The bottom graph of figure 7.32 shows the LWP as a function of time. The spread in the simulated LWP with DALES is quite large, but all show the same tendencies. All runs show a decrease in LWP just before Julian day 73, as confirmed in the observational data.

The terms in the budget equations 7.1 and 7.2 from the basic DALES simulation are shown as a function of time in figure 7.33.

The evolution of the liquid water potential temperature is dominated by the subsidence and the radiation in the first 12 hours. The horizontal advection is directly prescribed by RACMO and therefore could introduce a significant uncertainty in the liquid potential temperature evolution. The evolution of the total specific humidity is mainly determined by the turbulent surface flux in the first and last 3 hours of the simulation period. The subsidence plays an important role in the first half of the simulation.
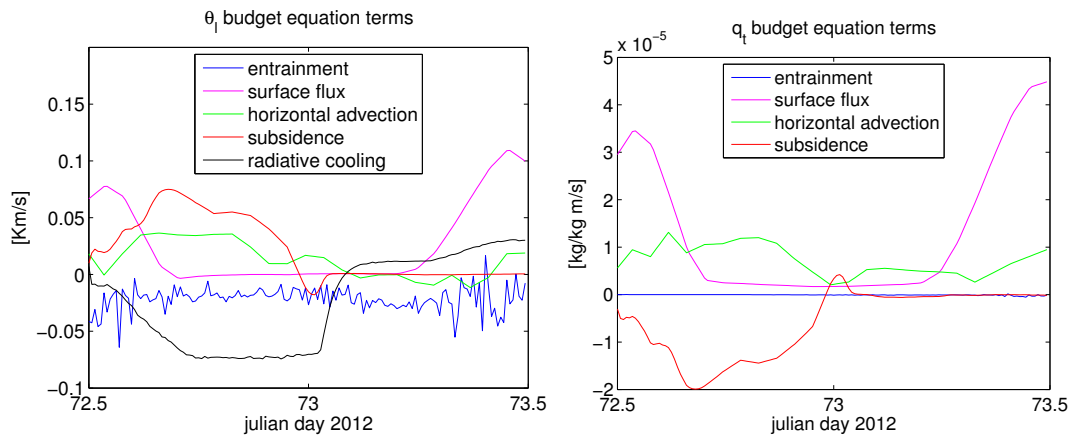
Figure 7.33: Terms from the budget equations 7.1 and 7.2 as a function of time, resulting from the basic DALES simulation.

Conclusions

Using data assimilation for the DALES simulations improves the prediction of the down-welling shortwave radiation when compared to RACMO. Using the observational heat fluxes results in a very well simulated cloud base and inversion height. The LWP shows the same tendency for all runs with DALES.

Chapter 8

Conclusions and recommendations

In this chapter the conclusions that follow from the results presented in this thesis will be discussed. Furthermore recommendations for further research will be given.

8.1 Conclusions

It was found that the occurrence of stratocumulus under a strong thermal inversion and in regions of subsidence in the period 2011 – 2012 at Cabauw is around 5 %. Stratocumulus is most likely to be found with a south-west or north-east wind direction. Furthermore stratocumulus was found to occur more at large zenith angles, thus more in winter time and in the morning and evenings. It was shown that the estimated reflected solar radiation by stratocumulus is more than 60 %, which demonstrates the large impact on the downwelling shortwave radiation at the surface.

With use of the quality matrices it was shown that RACMO and GALES have difficulties with the prediction of stratocumulus. The models predict less than 50 % of the observed stratocumulus cases correctly. Also it showed that stratocumulus is sometimes simulated while it is not observed. It must be noted however, that the subset of cases with a large LTS and in a subsidence region with which the quality matrices are calculated, is rather small for the examined period. It was found that the observed boundary layer types shallow cumulus and other low clouds in 2012 contain too little data points to obtain statistical reliable results for the performance of GALES.

Scatter plots of the simulated downwelling shortwave radiation showed that large difference between the RACMO simulated and observed solar radiation occur. When stratocumulus was identified in the observations the downwelling shortwave radiation was often modelled too high in RACMO.

Simulations with DALES have shown that LES is capable of predicting stratocumulus clouds. With use of data assimilation an improved prediction of the downwelling shortwave radiation is achieved during the first 6 hours after initialization.

69

However accurately predicting stratocumulus is sensitive to the prescribed forces and initial conditions. The uncertainties in these input parameters are quite significant since horizontal homogeneity of the atmosphere on a domain of 30 km is assumed, while it was found that this is not always the case. Furthermore the input parameters do not only depend on observations, but also on RACMO predictions of the large scale forcings. It was shown that the large scale heat and moisture advection sometimes have a large influence on the development of the potential temperature and water vapour specific humidity profiles. Furthermore it was shown that the sensible and latent heat fluxes are too high in RACMO, when the cloud layer is missing. The DALES simulations of the LWP however showed very similar tendencies by the additional runs with variations in the input parameters.

8.2 Recommendations

The quality matrices and climatology graphs in this report are obtained with data sets covering 1 to 2 years. One should consider expanding the data sets to obtain statistically more reliable results. Especially for the quality matrix of GALES this is recommended, since the subset of cases with a high LTS and in regions of subsidence is only only in 6 % in 2012.

It is recommended that the simulation period with DALES be reduced to 12 hours instead of 24 hours, since the simulation results have shown that in the first 12 hours the results are more accurate.

It was shown that the use of the latent and sensible heat fluxes from RACMO can negatively influence the DALES simulations. When the cloud deck is missing in RACMO, the RACMO heat fluxes are far too high. In this research observational heat fluxes were therefore used. In practice however these are not know when a forecast is made. Therefore it is recommended to calculate the heat fluxes with DALES instead.

It was found that the atmospheric conditions between Cabauw and de Bilt can not always assumed to be homogeneous. This complicates the use of the radiosonde measurements for initialization. It is recommended that multiple runs with changes in the jump in θ_l and q_t over the inversion layer are done for each case. This way effect of the uncertainty in the radiosonde profiles is assessed.

Furthermore one could try to simulate cases for which RACMO or GALES predict stratocumulus, while it is not observed. The question is if the data assimilation method with DALES is also capable of improving the prediction in these cases.

Acknowledgments

Bibliography

Bennetts, McCallumand, and Grant. Stratocumulus: an introductory account. *Meteorological Magazine*, 115:65–76, 1986.

H. O. G. Benschop. Validation of cloud cover in gpu-resident atmospheric large-eddy simulations. Master's thesis, TU Delft, 2013.

S. R. de Roode. Clouds, 2004.

C.J. de Rover, D. Vogelezang, H. van Bruggen, N. Maat, L. Smit, J. Heijstek, M. Keet, J. Wijngaard, and R. ten Hove. Improved low visibility and ceiling forecasts at schiphol airport. final report part 1. Technical report, KDC, 2008.

C.J. Hahn, W.B. Rossow, and S.G. Warren. ISCCP cloud properties associated with standard cloud types identified in individual surface observations. *J. Climate*, 14: 11–28, 2001.

M.J. de Haij, W.M.F. Wauben, and H. K. Baltink. Continuous mixing layer height determination using the ld-40 ceilometer: a feasibility study. *KNMI publication: WR-2007-01*, 2007.

T. Heus, C. van Heerwaarden, and J. van der Dussen. *Introduction to DALES v3.1*. TU Delft, 2009.

T. Heus, C. C. van Heerwaarden, H. J. J. Jonker, A. Pier Siebesma, S. Axelsen, K. van den Dries, O. Geoffroy, A. F. Moene, D. Pino, S. R. de Roode, and J. Vilà-Guerau de Arellano. Formulation of the dutch atmospheric large-eddy simulation (dales) and overview of its applications. *Geoscientific Model Development*, 3(2):415–444, 2010.

T. Hoff, C. Lenox, N. Miller, Y-huei Wan, R. George, J. Stein, B. Kroposki, A.D. Mills, M. Ahlstrom, M. andBrower, and A. Ellis. Understanding variability and uncertainty of photovoltaics for integration with the electric power system. Technical report, LBNL, 2009.

A. Jacobs, N. Maat, J. van der Meulen, and H. Roozekrans. Impact inventory: Een inventarisatie van kritieke weerparameters die de operatie op luchthaven schiphol benvloeden. Technical report, kennis voor klimaat, 2011.

Dr.ir. A.J.M. Jacobs, Dr. J. Barkmeijer, Prof. dr. A.P. Siebesma, Dr. ir. E.V. van der Plas, Dr.ir. B.G.J. Wichers Schreur, Ir. J.N. Roozekrans, Prof. dr. A.A.M. Holtslag, Dr.ir. G.J. Steeneveld, Dr. ir. R.J. Ronda, Dr. S.R. de Roode, Ramon Mendez Gomez, Drs. P. van den Brink, Ing. J.O. Haanstra, and Ir. L.E.M. Smit. The impact of climate change on the critical weather conditions at schiphol airport (impact). Technical report, Foundation Knowledge for Climate, 2012.

S.A. Klein and D.L. Hartmann. The seasonal cycle of low stratiform clouds. *J. Climate*, 6(8):1587–1606, 1993.

KNMI. anual report 2011. Technical report, KNMI, 2011.

D. Lew and G. Brinkman. The western wind and solar, integration study phase 2: Executive summary. Technical report, National Renewable Energy Laboratory, 2013.

D. K. Lilly. Models of cloud topped mixed layers under a strong inversion. *The Quarterly Journal of the Royal Meteorological Society*, 94:292–309, 1968.

E. van Meijgaard, L.H. van Ulft, W.J. van de Berg, F.C. Bosveld, B.J.J.M. van den Hurk, and A.P. Lenderink, G. Siebesma. The knmi regional atmospheric climate model racmo version 2.1. Technical report, KNMI, 2008.

R.A.J. Neggers and A.P. Siebesma. *The KNMI Parameterization Testbed Users Guide Version 2.0*. KNMI, 2010.

S.B. Pope. *Turbulent Flows*. Cambridge University Press, 2000.

D.W. Reynolds, D.A. Clark, F.W. Wilson, and L. Cook. Forecast-based decision support for san francisco international airport: A nextgen prototype system that improves operations during summer stratus season. *Bull. Amer. Meteor. Soc.*, 93(10):1503–1518, 2012.

S.R. de Roode, A.P. Siebesma, S. Dal Gesso, H.J.J. Jonker, J. Schalkwijk, and J. Sival. The stratocumulus response to a single perturbation in cloud controlling factors. Submitted for publication in the J. of Climate, 2012.

J. Schalkwijk, E.J. Griffith, F.H. Post, and H.J. J. Jonker. High-performance simulations of turbulent clouds on a desktop pc: Exploiting the gpu. *Bull. Amer. Meteor. Soc.*, 93:307–314, 2012.

P. M. M. Soares, A. P. Miranda, P. M. A. Siebesma, and J. Teixeira. An eddy-diffusivity/mass-flux parametrization for dry and shallow cumulus convection. *Q.J.R. Meteorol. Soc.*, 130:3365–3383, 2004.

J.J. van der Dussen. Large eddy and mixed-layer model simulations of the stratocumulus to cumulus transition as observed during astex. Master's thesis, TU Delft, 2009.

R. Wood. Stratocumulus clouds. *Mon. Wea. Rev.*, 140:2373–2423, 2012.

R. Wood and C.S. Bretherton. On the relationship between stratiform low cloud cover and lower-tropospheric stability. *J. Climate*, 19(24):6425–6432, 2006.

K. Xu, T. Wong, B.A. Wielicki, and L. Parker. Statistical analyses of satellite cloud object data from ceres. part iv: Boundary layer cloud objects during 1998 el nino. *J. Climate*, 21(7):1500–1521, 2008.

F. Yang, H. Pan, S.K. Krueger, S. Moorthi, and S.J. Lord. Evaluation of the ncep global forecast system at the arm sgp site. *Mon. Wea. Rev.*, 134(12):3668–3690, 2006.

Appendix A

Periods of stratocumulus

Periods of stratocumulus in the observations, in RACMO and in GALES are selected as described in section 4.2. In A.1 and A.2 the resulting observation cases are listed according to date. The second and third column indicate the date and time in UTC at the start of the period. The fourth column indicates the length of the period in hours. The selected cases in RACMO and GALES that overlap with the observational cases and are also shown in the table. The modelled cases of which more than 50% of the period is not identified as stratocumulus in the observations are shown separately in table A.3 for RACMO and table A.4 for GALES.

Table A.1: selection of observed stratocumulus periods longer than 3 hours in 2011, together with corresponding RACMO periods, indicated with Rcase

case	date	start UTC	hours	Rcase	start UTC	hours
1	04/01/2011	14:40	11.33	—	–:–	—
2	06/01/2011	04:30	6.00	1	04:30	3.50
3	11/01/2011	17:20	7.33	2	17:20	6.17
4	21/01/2011	01:20	3.83	3	01:00	4.17
5	27/01/2011	04:40	5.17	—	–:–	—
6	30/01/2011	06:50	29.50	6	05:40	6.33
7	31/01/2011	12:30	20.33	—	–:–	—
8	01/02/2011	20:10	11.17	—	–:–	—
9	05/02/2011	08:30	3.83	—	–:–	—
10	06/02/2011	04:20	5.33	7	04:50	3.17
11	07/02/2011	01:40	3.50	—	–:–	—
12	18/02/2011	00:10	5.17	—	–:–	—
13	18/02/2011	08:00	5.83	—	–:–	—
14	18/02/2011	17:20	11.33	8	17:20	4.67
15	24/02/2011	17:20	12.50	9	17:20	12.50
16	28/02/2011	08:50	5.83	10	08:50	5.83
17	28/02/2011	15:50	4.67	11	15:50	11.50
18	05/03/2011	06:60	5.33	12	07:30	4.50
19	05/03/2011	13:30	4.50	13	13:30	3.50
20	16/03/2011	07:00	4.83	—	–:–	—
21	16/03/2011	17:20	13.17	—	–:–	—
22	19/03/2011	05:30	3.33	—	–:–	—
23	01/04/2011	03:10	4.67	—	–:–	—
24	05/04/2011	21:30	7.33	—	–:–	—
25	07/06/2011	00:30	7.83	15	03:20	3.50
26	13/06/2011	02:20	4.33	16	02:40	4.00
27	26/06/2011	04:40	4.17	—	–:–	—
28	27/07/2011	01:50	4.50	—	–:–	—
29	29/07/2011	06:30	4.50	18	05:10	19.67
30	29/07/2011	13:30	4.00	18	05:10	19.67
31	29/07/2011	17:40	6.00	18	05:10	19.67
32	30/07/2011	20:20	3.83	—	–:–	—
33	13/08/2011	04:20	4.17	—	–:–	—
34	20/09/2011	02:40	4.00	22	03:50	6.17
35	30/10/2011	16:10	4.50	—	–:–	—
36	30/10/2011	22:50	10.33	—	–:–	—
37	02/11/2011	04:30	6.00	23	04:30	7.67
38	06/11/2011	00:40	4.67	—	–:–	—
39	06/11/2011	22:40	3.67	24	22:40	3.67
40	07/11/2011	06:50	5.50	25	06:50	5.50

case	date	start UTC	hours	Rcase	start UTC	hours
41	07/11/2011	19:40	15.33	—	–:–	—
42	10/11/2011	11:10	5.50	—	–:–	—
43	11/11/2011	01:50	11.33	—	–:–	—
44	13/11/2011	05:20	12.33	—	–:–	—
45	14/11/2011	01:60	6.50	—	–:–	—
46	28/11/2011	23:20	11.67	—	–:–	—
47	21/12/2011	15:10	7.33	26	15:10	4.33
48	24/12/2011	22:00	3.33	—	–:–	—
49	27/12/2011	05:20	7.83	—	–:–	—

Table A.2: selection of observed stratocumulus periods longer than 3 hours in 2012, together with corresponding RACMO and GALES periods, indicated with Rcase and Gcase respectively

case	date	UTC	hours	Rcase	UTC	hours	Gcase	UTC	hours
50	24/01/2012	21:30	4.00	—	–:–	—	—	–:–	—
51	25/01/2012	07:30	5.00	—	–:–	—	2	04:50	7.67
52	29/01/2012	00:00	11.67	—	–:–	—	4	00:00	12.00
53	29/01/2012	17:50	4.83	—	–:–	—	—	–:–	—
54	07/02/2012	21:00	14.00	31	01:50	8.00	—	–:–	—
55	09/02/2012	06:10	5.50	32	09:00	3.50	—	–:–	—
56	21/02/2012	22:30	5.67	—	–:–	—	—	–:–	—
57	06/03/2012	08:10	4.33	—	–:–	—	—	–:–	—
58	13/03/2012	09:40	11.50	33	09:40	11.50	6	09:40	11.50
59	14/03/2012	02:20	7.50	34	21:40	16.33	7	21:40	17.67
60	03/05/2012	08:40	3.17	35	08:40	3.17	8	08:40	3.17
61	03/06/2012	16:30	5.17	—	–:–	—	10	14:40	8.17
62	09/08/2012	03:10	3.33	—	–:–	—	—	–:–	—
63	03/09/2012	03:50	3.17	—	–:–	—	—	–:–	—
64	17/09/2012	03:40	4.00	39	04:40	4.67	13	03:20	6.00
65	21/10/2012	19:20	11.00	—	–:–	—	—	–:–	—
66	24/10/2012	14:30	6.33	—	–:–	—	—	–:–	—
67	24/10/2012	22:40	3.67	—	–:–	—	—	–:–	—
68	13/11/2012	08:30	9.83	41	08:30	12.50	—	–:–	—
69	15/11/2012	03:00	5.17	—	–:–	—	—	–:–	—
70	17/11/2012	18:10	4.50	43	18:10	4.50	19	18:10	4.50
71	19/11/2012	00:10	3.67	—	–:–	—	—	–:–	—
72	07/12/2012	20:50	3.83	—	–:–	—	—	–:–	—
73	13/12/2012	23:10	8.00	47	04:60	3.17	22	23:10	11.17

case	date	UTC	hours	Rcase	UTC	hours	Gcase	UTC	hours
61	03/03/2012	02:10	6.00	—	–:–	—	—	–:–	—
62	07/03/2012	12:20	5.33	—	–:–	—	13	12:00	5.67
63	10/03/2012	19:10	4.00	—	–:–	—	15	19:60	3.33
64	13/03/2012	09:40	24.17	55	09:40	28.50	16	09:40	29.83
65	02/05/2012	04:00	3.67	—	–:–	—	—	–:–	—
66	03/05/2012	06:20	3.67	57	06:20	3.67	18	06:20	3.67
67	11/05/2012	06:20	4.50	58	06:20	4.50	—	–:–	—
68	28/05/2012	23:20	6.17	—	–:–	—	19	22:40	6.83
69	03/06/2012	05:50	7.67	—	–:–	—	20	04:10	9.33
70	09/08/2012	03:10	3.33	—	–:–	—	—	–:–	—
71	21/08/2012	02:30	4.00	59	02:30	4.50	—	–:–	—
72	03/09/2012	03:50	3.17	—	–:–	—	—	–:–	—
73	03/09/2012	21:40	6.83	—	–:–	—	—	–:–	—
74	14/09/2012	04:10	5.67	62	04:40	7.50	21	04:60	7.00
75	17/09/2012	03:40	4.00	—	–:–	—	22	03:30	4.33
76	20/10/2012	04:10	5.17	66	03:00	6.33	—	–:–	—
77	20/10/2012	17:40	17.83	67	23:40	11.83	25	15:40	18.83
78	21/10/2012	15:30	14.83	—	–:–	—	—	–:–	—
79	24/10/2012	16:40	19.50	68	03:10	9.00	26	01:40	11.67
80	13/11/2012	05:20	13.00	70	01:10	19.83	—	–:–	—
81	15/11/2012	03:00	8.00	—	–:–	—	—	–:–	—
82	17/11/2012	08:10	8.67	72	12:20	4.50	30	11:20	5.50
83	19/11/2012	00:10	3.67	—	–:–	—	—	–:–	—
84	21/11/2012	04:50	3.67	—	–:–	—	—	–:–	—
85	03/12/2012	06:30	6.67	75	08:40	4.50	—	–:–	—
86	13/12/2012	20:10	12.50	76	21:20	11.17	—	–:–	—
87	20/12/2012	10:20	17.17	77	19:60	7.50	35	13:20	14.17

Table A.3: Selection of RACMO stratocumulus periods for which less than 50% of the period corresponds to observed stratocumulus

RACMO case	date	UTC	hours
4	26/01/2011	01:30	4.33
5	26/01/2011	16:60	3.67
14	15/03/2011	02:50	7.50
17	04/07/2011	05:30	4.83
19	30/07/2011	12:10	6.67
20	30/07/2011	21:60	14.50
21	10/09/2011	00:00	5.67
27	27/12/2011	07:60	10.83
28	11/01/2012	04:20	6.17
29	25/01/2012	18:30	4.17
30	29/01/2012	17:50	9.67
36	04/05/2012	18:50	5.17
37	01/06/2012	00:60	5.00
38	02/09/2012	22:30	9.33
40	20/10/2012	12:00	4.67
42	15/11/2012	23:30	12.83
44	19/11/2012	00:10	10.17
45	19/11/2012	12:40	8.67
46	24/11/2012	02:50	9.33
48	19/12/2012	16:10	4.67
49	28/12/2012	18:20	3.67

Table A.4: selection of GALES stratocumulus periods for which less than 50% of the period corresponds to observed stratocumulus

GALES case	date	UTC	hours
1	11/01/2012	03:40	6.83
3	25/01/2012	18:30	4.17
5	06/03/2012	04:00	4.17
9	03/06/2012	03:60	3.50
11	27/06/2012	00:50	4.17
12	28/07/2012	03:00	4.17
14	20/10/2012	12:30	6.00
15	25/10/2012	12:20	3.33
16	10/11/2012	05:40	3.83
17	13/11/2012	08:30	20.33
18	16/11/2012	04:00	3.50
20	18/11/2012	23:30	23.83
21	24/11/2012	07:20	3.50
23	19/12/2012	16:10	4.17
24	20/12/2012	07:50	3.17
25	28/12/2012	18:20	3.67

Appendix B

Sensitivity of diagnosed stratocumulus amount to the criteria

In section 4.1 and 4.3 is discussed how the LTS is used to select a data subset for identifying stratocumulus (stcu), shallow cumulus (shcu), other low broken clouds (br cl), a clear atmosphere (clear) and other boundary layer types (other) under a strong thermal inversion. The sensitivity of the selection for the used criteria is tested by making changes in the criteria.

In figure B.1 the LTS threshold for selecting the data subset with a high LTS is varied. The resulting fractions of the subset is shown for each category.
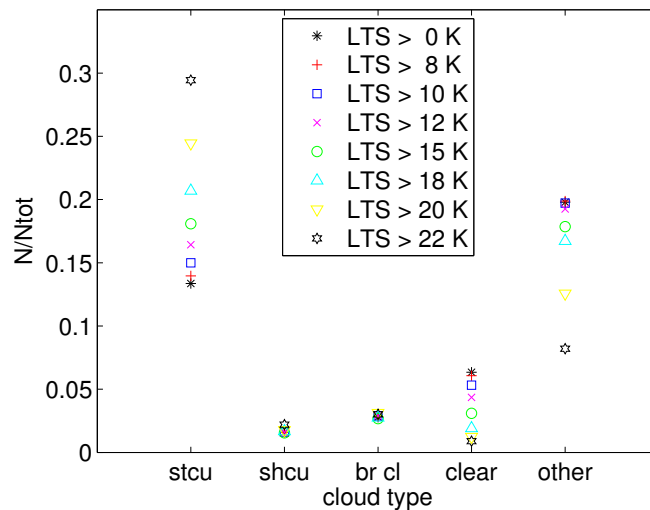
Figure B.1: The fractions of boundary layer types relative to the whole subset of cases with a LTS higher than the set criteria indicated in the legend.

It is shown that the stratocumulus fraction of LTS subset increases, when the LTS threshold for the subset is increased. Increasing the LTS threshold however also leads to a decreasing absolute number of selected stratocumulus moments. The fraction of shallow cumulus and other low broken clouds are hardly effected by changing the LTS criteria. The fraction of clear moments in the LTS subset shows a decrease with an increasing LTS threshold.

In figure B.2 the effect on the fraction per category of changes in the other criteria is shown. For this graph the data subset is constant and selected by a RACMO LTS above 15 K in a region of subsidence.
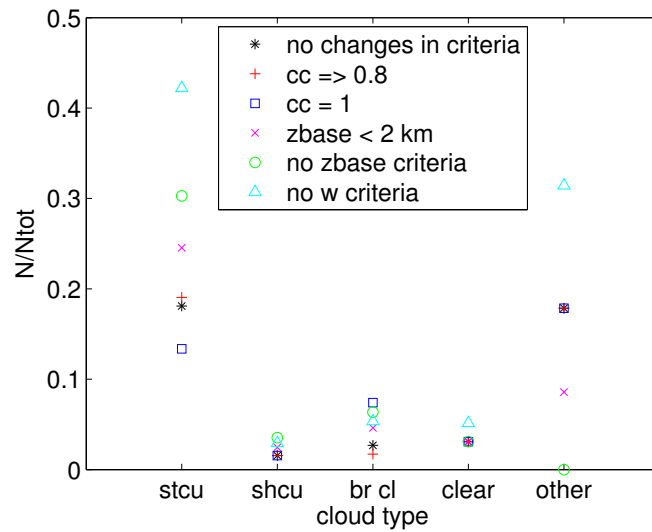
Figure B.2: The fractions of the data subset defined by a RACMO LTS larger than 15 K in a subsidence region that correspond to each of the 5 boundary layer types.

It is shown that the changes in the cloud cover criteria have little effect. The selection is more sensitive for the changes made in the cloud base height criteria. Not using the subsidence criteria is has the biggest effect on the selection of stratocumulus.

Appendix C

NCEP Global Forecast System

The Global Forecast System is generated by the National Centers for Environmental Prediction (NCEP). It is a global climate model with a grid spacing of 0.5 ° or about 55 km. With the model a 48 hour forecast is generated every 6 hours. The time steps for computing dynamics are about 5 min, except for the calculation of longwave radiation that is done once every 3 h and shortwave radiation done once every hour (Yang et al., 2006). The data from each forecast is saved in 3 hourly intervals. Energy fluxes at the Earth's surface and top of the atmosphere, are saved as averages. State variables such as the surface and atmospheric temperatures, cloud fraction and specific humidity are saved as instantaneous values at the end of each interval (Yang et al., 2006).

This research has processed the 3 hour and 6 hour predictions of each of the 6 hourly forecasts in 2012. This selection thus results in a set of 3 hourly data covering the year 2012, consisting of alternately 3 and 6 hour predictions. The averaged flux values of the 6 hour predictions are corrected to 3 hour averages. Note that the temporal resolution is much courser than that of the observations.

In figure C.1 the simulated shortwave radiation in NCEP is scattered against the observed radiation at the surface, in 3 hour averages. The NCEP forecast often gives a too high shortwave radiative flux. The annual mean of the NCEP forecast is 148 Wm^{-2}, while for the 3 hourly observation data in 2012 this mean is 117 Wm^{-2}. The overestimation of the downwelling shortwave radiation was also found by Yang et al. (2006), which states a overestimated daily maximum surface downward solar flux by 44 Wm^{-2}. The observations moments that fulfil the stratocumulus criteria are encircled with red. The RMSE of the total NCEP data is 79 Wm^{-2}, while for the observed stratocumulus points the RMSE is 68 Wm^{-2}.

In table C.1 the quality matrix of NCEP versus the observations is shown. NCEP scores are dramatically low. Only 12 % of the stratocumulus cases are modelled as such. 21 % is modelled as shallow cumulus or other low broken clouds, 39 % is modelled as clear and 27 % is classified as others. However, modelling stratocumulus while it is not observed is basically never found. A clear atmosphere is modelled when it is observed for 61 % of the identified clear cases in the observations, however a clear boundary is also often falsely modelled.
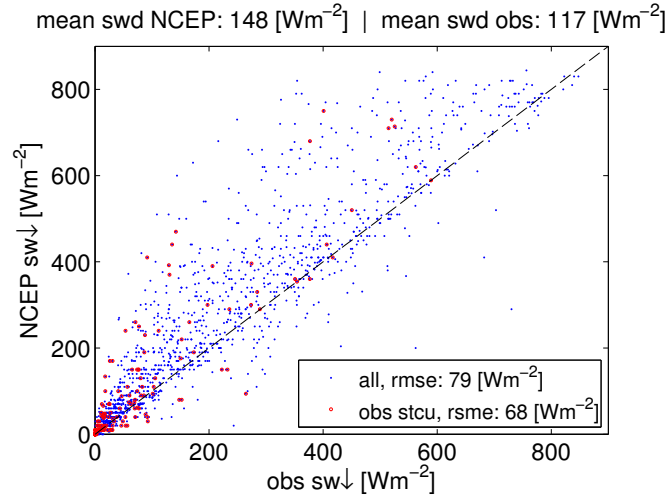
Figure C.1: Scatter plot of the downwelling shortwave radiation in NCEP as a function of the observations. The total mean of the model and of the observations is given above the figure. The identified observed stratocumulus points are indicated with red circles. The RMSE of the model with respect to the observations is given in the legend.

Table C.1: Quality matrix of NCEP for 2012, in 3 hourly intervals

	N stcu	N shcu	N low br	N clear	N other
obs stcu	**0.12**	0.09	0.12	0.39	0.27
obs shcu	0.00	**0.17**	0.33	0.33	0.17
obs low br	0.00	0.21	**0.16**	0.37	0.26
obs clear	0.04	0.04	0.04	**0.61**	0.12
obs other	0.02	0.06	0.05	0.59	**0.28**

Appendix D

Namoptions

An example of the namoptions file as used for the DALES simulations is shown in D.1.

Table D.1: example of the namoptions file

```
&RUN
iexpnr        =                 005
lwarmstart    =              .false.
startfile     =    'initd00h00m000.000'
runtime       =               86400
trestart      =                3600
dtmax         =                  10
ladaptive     =               .true.
irandom       =                  43
randthl       =                 0.1
randqt        =               2.5e-5
nsv           =                   0
/
&DOMAIN
imax          =                  72
jtot          =                  72
kmax          =                 200
xsize         =                3600.
ysize         =                3600.
xlat          =                 52.
xlon          =                 -5.
xday          =                 48.
xtime         =                 12.
/
```

```
&PHYSICS
ps               =      101640.83
thls             =         272.90
lmoist           =          .true.
lcoriol          =          .true.
iradiation       =              1
useMcICA         =          .true.
timerad          =             10
rad_longw        =          .true.
rad_shortw       =          .true.
dlwtop           =            70.
dlwbot           =            15.
sw0              =           600.
ltimedep         =          .true.
/
&NAMSURFACE
albedoav         =           0.24
wtsurf           =          0.011
wqsurf           =          8e-06
isurf            =              4
lsmoothflux      =         .false.
ustin            =            0.1
z0               =           2e-4
/
&NAMRADSTAT
dtav             =             60
timeav           =           600.
lstat            =          .true.
/
&DYNAMICS
llsadv           =         .false.
lqlnr            =         .false.
cu               =            -2.
cv               =            -4.
iadv_mom         =              5
iadv_tke         =              5
iadv_thl         =              5
iadv_qt          =              5
iadv_sv          =              5
/
```

```
&SUBGRID
ldelta              =    .false.
cm                  =     0.12
cn                  =     0.76
ch1                 =       1.
ch2                 =       2.
ce1                 =     0.19
ce2                 =     0.51
/
&NAMBUDGET
lbudget             =    .false.
dtav                =      60.
timeav              =     600.
/
&NAMCHECKSIM
tcheck              =        6
/
&NAMSAMPLING
dtav                =       60
timeav              =     600.
lsampcl             =    .false.
lsampco             =    .false.
lsampup             =    .false.
lsampbuup           =    .false.
lsampcldup          =    .false.
/
&NAMTIMESTAT
ltimestat           =    .true.
dtav                =       60
/
&NAMCROSSSECTION
lcross              =    .false.
dtav                =       60
/
&NAMGENSTAT
lstat               =    .true.
dtav                =       60
timeav              =      600
/
```

```
&NAMFIELDDUMP
lfielddump      =    .false.
dtav            =        60
ldiracc         =    .true.
/
&NAMSTATTEND
dtav            =        60
ltend           =    .true.
timeav          =      600.
/
```